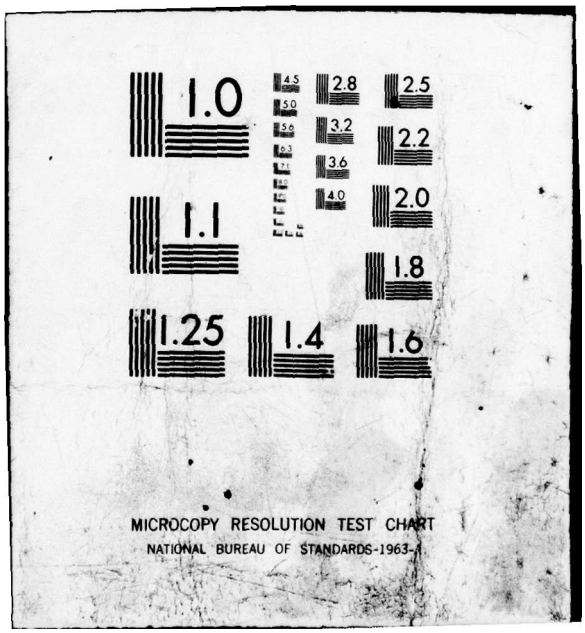
AD-A077 690 CALSPAN ADVANCED TECHNOLOGY CENTER BUFFALO NY AERODYN--ETC F/G 21/5
BASIC STUDIES OF ROTATING STALL IN AXIAL FLOW COMPRESSORS.(U)
SEP 79 G R LUDWIG , J P NENNI F33615-76-C-2092
UNCLASSIFIED CALSPAN-XE-5933-A-105 AFAPL-TR-79-2083 NL

1 OF 2
AD
A077690




1.0
1.1
1.25
1.4
1.6
1.8
2.0
2.2
2.5
2.8
3.2
3.6
4.0
4.5
5.0
5.6
6.3
7.1
MICROCOPY RESOLUTION TEST CHART
NATIONAL BUREAU OF STANDARDS-1963-A

AD A077690

AFAPL-TR-79-2083

LEVEL II

BASIC STUDIES OF ROTATING STALL IN AXIAL FLOW COMPRESSORS

DDC RECEIVED DEC 5 1979 E

Aerodynamic Research Department
Calspan Advanced Technology Center
P.O. Box 400
Buffalo, New York 14225

September 1979

DDC FILE COPY

TECHNICAL REPORT AFAPL-TR-79-2083

Final Report for Period 1 June 1976 - 31 April 1979

Approved for public release; distribution unlimited

AIR FORCE AERO-PROPULSION LABORATORY
AIR FORCE WRIGHT AERONAUTICAL LABORATORIES
AIR FORCE SYSTEMS COMMAND
WRIGHT-PATTERSON AIR FORCE BASE, OHIO 45433

79 12 3 042

NOTICE

When Government drawings, specifications, or other data are used for any purpose other than in connection with a definitely related Government procurement operation, the United States Government thereby incurs no responsibility nor any obligation whatsoever; and the fact that the government may have formulated, furnished, or in any way supplied the said drawings, specifications, or other data, is not to be regarded by implication or otherwise as in any manner licensing the holder or any other person or corporation, or conveying any rights or permission to manufacture, use, or sell any patented invention that may in any way be related thereto.

This report has been reviewed by the Information Office (ASD/OIP) and is releasable to the National Technical Information Service (NTIS). At NTIS, it will be available to the general public, including foreign nations.

This technical report has been reviewed and is approved for publication.

Marvin A. Stibich
MARVIN A. STIBICH
Project Engineer

FOR THE COMMANDER

Ernest C. Simpson
ERNEST C. SIMPSON
Director
Turbine Engine Division

"If your address has changed, if you wish to be removed from our mailing list, or if the addressee is no longer employed by your organization please notify AFAPL/TBC ,W-P AFB, OH 45433 to help us maintain a current mailing list".

Copies of this report should not be returned unless return is required by security considerations, contractual obligations, or notice on a specific document.

AIR FORCE/56780/16 November 1979 — 60

SECURITY CLASSIFICATION OF THIS PAGE (When Data Entered)

REPORT DOCUMENTATION PAGE

READ INSTRUCTIONS BEFORE COMPLETING FORM

1. REPORT NUMBER: AFAPL-TR-79-2083	2. GOVT ACCESSION NO.
3. RECIPIENT'S CATALOG NUMBER	
4. TITLE (and Subtitle): Basic Studies of Rotating Stall In Axial Flow Compressors	5. TYPE OF REPORT & PERIOD COVERED: Final Report June 76 — April 79
6. PERFORMING ORG. REPORT NUMBER: CALSPAN-XE-5933-A-10S	
7. AUTHOR(s): Gary R. Ludwig, Joseph P. Nenni	8. CONTRACT OR GRANT NUMBER(s): F33615-76-C-2092
9. PERFORMING ORGANIZATION NAME AND ADDRESS: Aerodynamic Research Department, Calspan Corporation, Advanced Technology Center, P. O. Box 400, Buffalo, New York 14225	10. PROGRAM ELEMENT, PROJECT, TASK AREA & WORK UNIT NUMBERS: 3066 04 24
11. CONTROLLING OFFICE NAME AND ADDRESS: Air Force Aero Propulsion Laboratory/TBC, Air Force Wright Aeronautical Laboratories (AFSC), Wright-Patterson Air Force Base, Ohio 45433	12. REPORT DATE: September 1979 13. NUMBER OF PAGES: 150
14. MONITORING AGENCY NAME & ADDRESS (if different from Controlling Office): U. S. Air Force Aero Propulsion Laboratory, Air Force Systems Command, Wright-Patterson Air Force Base, OHIO 45433	15. SECURITY CLASS (of this report): UNCLASSIFIED 15a. DECLASSIFICATION DOWNGRADING SCHEDULE

16. DISTRIBUTION STATEMENT (of this Report)

Approved for public release; distribution unlimited.

17. DISTRIBUTION STATEMENT (of the abstract entered in Block 20, if different from Report)

18. SUPPLEMENTARY NOTES

19. KEY WORDS (Continue on reverse side if necessary and identify by block number)

Rotating Stall
Compressor
Cascade
Fluid Mechanics
Jet Engines

20. ABSTRACT (Continue on reverse side if necessary and identify by block number)

This report presents the results of a theoretical and experimental program aimed at obtaining a sufficient understanding of the rotating stall phenomena such that its onset and properties can be predicted under a wide set of circumstances. The theoretical research covers the development of two-dimensional stability theories for compressible flows and the progress towards the development of a three-dimensional theory for incompressible flow. The experimental work, performed in an annular cascade facility, studied the effects of rotor-

DD FORM 1 JAN 73 1473 EDITION OF 1 NOV 65 IS OBSOLETE

SECURITY CLASSIFICATION OF THIS PAGE (When Data Entered)

391 214

stator interference both on the steady-state performance of the blade rows and on rotating stall. The influence of circumferential distortion on the rotating stall boundary for the stage was also determined. Comparisons are made between the experimental results and the predictions of a two-dimensional rotating stall stability theory which had been developed previously for incompressible flows.

FOREWORD

This is the final technical report prepared by Calspan Corporation on a portion of a multi-phase program sponsored by the Air Force Aero-Propulsion Laboratory, Air Force Systems Command, Wright-Patterson AFB, Ohio under Contract F33615-76-C-2092. The work reported herein was performed as part of Phases I and II of Project 3066, "Investigation of Rotating Stall and Turbine Heat Transfer in Axial Flow Turbomachinery," with Mr. Marvin A. Stibich, AFAPL/TBC, as Project Engineer. Dr. Gary R. Ludwig of the Aerodynamic Research Department of Calspan Corporation, had overall technical responsibility for the program, and carried out the experimental measurements. The theoretical studies of rotating stall were performed by Dr. Joseph P. Nenni. Mr. John Nemeth designed the experimental apparatus and assisted in the experiments.

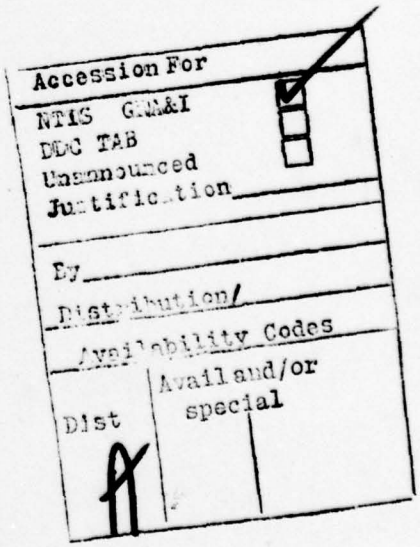


TABLE OF CONTENTS

SECTION		PAGE
I	INTRODUCTION	1
II	THEORETICAL ROTATING STALL RESEARCH	3
	A. INTRODUCTION	3
	B. TWO-DIMENSIONAL COMPRESSIBLE FLOW STABILITY THEORY	3
	C. THREE-DIMENSIONAL INCOMPRESSIBLE FLOW STABILITY THEORY	19
	1. General Analysis	20
	2. Upstream Flow Disturbances	24
	3. Downstream Flow Disturbances	28
	D. CONCLUDING REMARKS ON THEORETICAL INVESTIGATIONS	33
III	EXPERIMENTAL ROTATING STALL RESEARCH	34
	A. INTRODUCTION	34
	B. DESCRIPTION OF ANNULAR CASCADE FACILITY WITH HIGH HUB-TO-TIP RATIO	36
	1. General Description	36
	2. Rotor and Stator Blading and Distortion Screen	37
	3. Instrumentation	41
	C. EXPERIMENTS ON A CLOSELY COUPLED ROTOR-STATOR STAGE	43
	1. Relative Losses Through the Rotor	44
	2. Turning Angle of Flow Through the Rotor	56
	3. Losses Through the Stator Row	58
	4. Turning Angle of Flow Through the Stator Row	59
	5. Effect of Inlet Distortion	60
	D. LOW HUB-TO-TIP RATIO ANNULAR CASCADE	65
	E. SUMMARY	66

TABLE OF CONTENTS (Cont'd.)

SECTION		PAGE
IV	COMPARISON BETWEEN THEORY AND EXPERIMENT FOR A CLOSELY COUPLED ROTOR-STATOR STAGE	71
	A. INTRODUCTION	71
	B. COMPARISONS BETWEEN THEORY AND EXPERIMENT	71
	C. THEORETICAL EFFECTS OF BLADE ROW SPACING	77
	D. SUMMARY	81
V	SUMMARY AND CONCLUSIONS	82
	REFERENCES	85
	APPENDIX A. FUNCTIONS APPEARING IN THE THREE-DIMENSIONAL STABILITY THEORY	86

LIST OF ILLUSTRATIONS

FIGURE		PAGE
1	Actuator Model for Two-Dimensional Analysis	101
2	Overall View of Annular Cascade Facility	102
3	View of Annular Cascade Test Section	103
4	Annular Cascade Configuration Used for Rotating Stall Studies on Rotor-Stator Stage	104
5	Notation for Annular Cascade with Rotor-Stator Stage	105
6	Total Pressure Coefficient Between Rotor and Stator in Rotor-Stator Stage	
	(a) Stator Stagger Angle, δ_{SM} = 28.2 deg	106
	(b) Stator Stagger Angle, δ_{SM} = 37.2 deg	107
7	Overall Total Pressure Rise Across Isolated Rotor and Rotor in Rotor-Stator Stage	108
8	Radial Distributions of Total Pressure Coefficient Downstream of Isolated Rotor. Total Pressure Rake Located at Axial Distance 3.9 Inches from Rotor Trailing Edge	109
9	Radial Distributions of Total Pressure Coefficient Downstream of Isolated Rotor. Comparison of Measurements Close to Rotor with Measurements Farther Downstream	110
10	Radial Distributions of Total Pressure Coefficient Immediately Downstream of Isolated Rotor and the Same Rotor in Rotor-Stator Stage	
	(a) Rotor RPM = 500, 700, 900	111
	(b) Rotor RPM = 600, 800, 1000, 1100	112
11	Total Pressure Rise Across Isolated Rotor and Across Rotor in Closely Coupled Rotor-Stator Stage	113

LIST OF ILLUSTRATIONS (Cont'd.)

FIGURE		PAGE
12	Comparisons of Radial Distributions of Total Pressure Rise Across Rotor in Rotor-Stator Stage with Rotor Work	
	(a) Stator Stagger Angle, δ_{SM} = 28.2 deg	114
	(b) Stator Stagger Angle, δ_{SM} = 37.2 deg	115
13	Radial Distributions of Work Coefficient Measured On Isolated Rotor	116
14	Overall Total Pressure Loss Through Rotor in Rotor-Stator Stage, Coordinate System Relative to Rotor	117
15	Comparison of Overall Outlet Swirl From Isolated Rotor Calculated From Rotor Work With Direct Measurements	118
16	Overall Total Pressure Loss Through Stators In Rotor-Stator Stage	119
17	Flow Turning Angle Correlation Based on Extrapolation Of Limited Data, Stator Set No. 1 - Various Stator Stagger Angles, δ_{SM}	120
18	Effect of Distortion Screen on Total Pressure Rise of Isolated Rotor, Absolute Coordinate System	121
19	Effect of Distortion Screen on Average Swirl Angles Downstream of Isolated Rotor, Absolute Coordinate System.....	122
20	Annular Cascade With Low Hub-To-Tip Ratio	123
21	Theoretical Stability Characteristics of Isolated Rotor	125
22	Theoretical Stability Characteristics of Rotor-Stator Stage, Stator Stagger Angle, δ_{SM} = 28.2 deg	126
23	Theoretical Stability Characteristics of Rotor-Stator Stage, Stator Stagger Angle, δ_{SM}= 37.2 deg	127

LIST OF ILLUSTRATIONS (Cont'd.)

FIGURE		PAGE
24	Theoretical Rotating Stall Propagation Velocities	128
25	Theoretical Stability Characteristics of Rotor-Stator Stage With Circumferential Inlet Distortion, Stator Stagger Angle, δ_{SM} = 28.2 deg	129
26	Theoretical Stability Characteristics of Rotor-Stator Stage With Circumferential Inlet Distortion, Stator Stagger Angle, δ_{SM} = 37.2 deg	130
27	Effect of Blade Row Spacing On Theoretical Damping Factors For Rotor-Stator Stage, δ_{RM} = 40 deg, δ_{SM} = 37.2 deg	
	(a) Number of Cells, n = 1	131
	(b) Number of Cells, n = 3	132
	(c) Number of Cells, n = 7	133

LIST OF TABLES

TABLE	TITLE	PAGE
1	Geometric Characteristics of Rotor Set No. 1	38
2	Geometric Characteristics of Stator Set No. 1	40
3	Summary of Rotating Stall Inception Points With and Without Circumferential Inlet Distortion	62
4	Rotating Stall Inception on Low Hub-to-Tip Ratio Rotor	67
5	Theoretical Effect of Blade Row Spacing On Rotating Stall Inception and Number of Cells	80

SYMBOLS

a_i sound speed in region i or coefficient in polynomial approximation to stream function

A_{ij} matrix elements defined on Pages 14 and 15

A, B constants in solution for total pressure and swirl in three-dimensional theory

A_i, B_i, D_i constants of integration in fundamental disturbance velocity solutions for incompressible flow (additional subscript n refers to nth Fourier component)

C complex exponent of disturbance velocity solutions

C_I, C_R imaginary and real part of C respectively

C_1, C_2, C_3 constants of integration in three-dimensional theory

C_p specific heat at constant pressure

$\Delta \overline{C}_{p_{T_1}}$ time-averaged total pressure rise coefficient across rotor (See Equation 64)

$\Delta \overline{\overline{C}}_{p_{T_1}}$ area average of $\Delta \overline{C}_{p_{T_1}}$ (See Equation 65)

$\Delta \overline{C}_{p_{T_2}}$ circumferential average of total pressure rise coefficient across stage

$\Delta \overline{\overline{C}}_{p_{T_2}}$ area average of $\Delta \overline{C}_{p_{T_2}}$

$(-\Delta \overline{C}_{p_{T_R}})$ time-averaged relative loss coefficient across rotor (See Equations 68 and 70)

$(-\Delta \overline{\overline{C}}_{p_{T_R}})$ area average of $(-\Delta \overline{C}_{p_{T_R}})$ (See Equation 71)

$(-\Delta\overline{\overline{C_{p_{T_S}}}})$ area-averaged loss coefficient across stators (See Equation 74)

$\Delta\overline{\overline{C_{p_{T_{q_1}}}}}$ area-averaged total pressure rise coefficient across rotor based on relative inflow velocity to rotor (See Equation 66)

$\overline{C}_w$ time-averaged rotor work coefficient based on axial velocity far upstream of rotor

$\overline{\overline{C}}_w$ area average of $\overline{C}_w$

$\overline{\overline{C}}_{w_{q_1}}$ area-averaged rotor work coefficient based on relative inflow velocity to rotor (See Equation 67)

E_i constant in disturbance pressure solution for compressible flow theory

G function expressing flow turning relationship

G_2 constant used in three-dimensional theory

H total pressure or total pressure divided by density

H_i total pressure in flow region i

I_i function used in compressible flow theory, see Page 16

j $\sqrt{-1}$

k_i constants in three-dimensional stability theory

K_i constants of integration in compressible flow theory

$K_i, \mathcal{L}_i$
$\mathcal{M}_i, \mathcal{N}_i$ solution functions in compressible flow theory

m parameter in three-dimensional theory, see Page 22

m_i function defined on Page 7

M_i Mach number in region i

n number of stall cells

p_i disturbance pressure in region i

P_i mean static pressure in region i

$\hat{P}_i$ sum of mean and disturbance pressures

P_{T_o} total pressure far upstream of stage

P_{T_1} total pressure in survey plane between rotor and stator

P_{T_2} total pressure in survey plane downstream of stator

q_o dynamic pressure corresponding to mean axial velocity, $(\rho/2)U_o^2$

q_1 dynamic pressure corresponding to mean inflow velocity relative to rotor, $(\rho/2)(U_o^2 + \overline{\overline{W}}_b^2)$

r, θ, z cylindrical coordinate system

r_H hub radius

r_T tip radius

R hub-to-tip ratio

SYMBOLS (Cont'd.)

$\mathcal{R}$	gas constant
R_i	mean density in region i
S_i	absolute swirl in region i, $(\tan \beta_i)$
$\mathcal{S}_i$	relative swirl in region i, $(\tan \beta_{i_R})$
t	time
T_{T_o}	total temperature far upstream of rotor
T_{T_1}	total temperature in survey plane between rotor and stator
ΔT_{T_1}	total temperature rise across rotor, $(T_{T_1} - T_{T_o})$
u_i	axial disturbance velocity in region i
U, V, W	velocities in cylindrical coordinate system
U_i	mean axial velocity in region i
U_o	mean axial velocity far ahead of blade row
U_1	axial velocity between rotor and stator
$\hat{U}_i$	sum of mean and disturbance axial velocities
V_p	absolute propagation velocity for rotating stall cell
V_{p_r}	relative propagation velocity for rotating stall cell

SYMBOLS (Cont'd.)

ω_i disturbance velocity along cascade axis

W_b blade velocity (W_b is constant in time so $W_b = \bar{W}_b$)

x, y Cartesian coordinates

β_i swirl angle in flow region i

$\bar{\beta}_i$ circumferential average flow angle in region i

$\bar{\beta}_{i_R}$ circumferential average flow angle in region i relative to blade row

$\bar{\bar{\beta}}_{i_R}$ radially averaged value of $\bar{\beta}_{i_R}$

δ_{RM} rotor stagger angle at mid annulus

δ_{SM} stator stagger angle at mid annulus

$\Delta\theta$ change in azimuthal angle

λ parameter defined on Page 16

ξ_i functions defined on Page 16

ρ density

ϕ flow coefficient ($U_o / \bar{\bar{W}}_b$)

Φ disturbance stream function

χ total pressure loss parameter (See Page 10)

χ' derivative of χ with respect to β_1

ψ stream function

Ω vorticity

Ω_θ θ component of vorticity

$\bar{\Omega}$ normalized blade velocity

$\bar{\Omega}_i$ normalized blade velocity in region i

Subscripts and Superscripts

In the theoretical presentations:

$( )_1$ denotes conditions upstream of blade row

$( )_2$ denotes conditions downstream of blade row

$\bar{( )}$ denotes averaged quantities

In the experimental presentations:

$( )_o$ denotes conditions far upstream of rotor

$( )_1$ denotes conditions downstream of rotor, but upstream of stator

$( )_2$ denotes conditions downstream of stator

$\bar{( )}$ indicates a time average downstream of rotating blades or a circumferential average downstream of stationary blades

$\bar{\bar{( )}}$ indicates that $\bar{( )}$ data have been integrated radially to obtain an area-average (for example see Equation 65).

SECTION I
INTRODUCTION

The optimum performance of a turbo-propulsion system is usually achieved when the compressor is operating near its maximum pressure ratio. However, this optimum is generally not attainable because it occurs close to compressor stall and unstable flow conditions. In actual operation a stall margin must be provided to prevent the compressor from penetrating the stall boundary and developing destructive unsteady flow phenomena such as rotating stall and surge. This is usually done by prescheduling the engine controls. When an aircraft has a varied flight envelope, the prescheduling approach can lead to the requirement for a large stall margin to keep the engine out of stall under all possible transient and steady flight conditions. This stall margin represents a significant performance penalty. Also, in many instances of engine failure, rotating stall has been identified as a precursor to destructive unsteady flows in an engine. Furthermore, blade fatigue considerations will not allow a compressor to operate for prolonged periods in a large amplitude rotating stall mode. Clearly then, it is desirable to develop methods of estimating the stall boundaries of a compressor and if possible to develop an engine control system that can sense incipient destructive unsteady flows in a compressor and take corrective action to prevent compressor stall. Recognition of these goals has been the motivation for a continuing program of research that the AFAPL has sponsored at Calspan since 1962. This report covers a portion of the work completed under the latest three year research program at Calspan.

The work accomplished under this portion of the program was both theoretical and experimental in nature and has been aimed at obtaining a sufficient understanding of the rotating stall phenomena such that its onset and properties can be predicted under a wide set of circumstances. The theoretical research is reported in Section II of this report and covers the development of two-dimensional stability theories for compressible flows and the progress towards the development of a three-dimensional theory for incompressible flow. The experimental research is covered in Section III of this report and describes a series of three tests that were performed in Calspan/Air Force Annular

Cascade Facility. The first series of tests was concerned with the effects of rotor-stator interference on closely coupled high hub-to-tip ratio stages. The effects of rotor-stator interference on both the steady-state performance of the blade rows and the rotating stall boundary for the stage were determined. The second series of tests was concerned with the influence of a stationary distortion pattern on the stall boundary for these stages. The third series of tests was concerned with obtaining the stall boundary on a low hub-to-tip ratio rotor. Section IV presents comparisons between the experimental results and the predictions of a two-dimensional rotating stall stability theory which was developed previously. The comparisons include an isolated rotor, a rotor-stator stage, and the stage with distortion. The theoretical effect of changing the axial separation between the blade rows in a stage is also discussed. A summary of the program is presented in Section V.

SECTION II

THEORETICAL ROTATING STALL RESEARCH

A. INTRODUCTION

The primary effects that have been studied theoretically are the stability of two-dimensional compressible flow through a blade row and the stability of three-dimensional incompressible flow through a blade row. The formulation of a stability theory for wholly subsonic two-dimensional compressible flows given in Reference 1 has been modified through a revision of the energy matching condition. Also some analysis of the theory has been made with respect to the mechanisms of rotating stall in supersonic flows. This work is described in Part B of this section. Progress towards developing three-dimensional stability theory for incompressible flow is given in Part C.

B. TWO-DIMENSIONAL COMPRESSIBLE FLOW STABILITY THEORY

A two-dimensional stability theory for the incompressible flow through a blade row (and stage) was given in Ref. 2. The theory employed a finite-thickness actuator model of the blade row and required the steady state loss and turning performance of the blade row as inputs. Correlations of the theory with low speed data on rotating stall boundaries taken in the CALSPAN/USAF Annular Cascade Facility have been good. The theory has been correlated with data on isolated blade rows for sixteen cases involving both rotors and stators, and for two different rotor-stator stages. The theory generally predicted the relative swirl to the blade row at which rotating stall occurred to within two percent. The basic theory was extended to wholly subsonic compressible flow in Ref. 1. The compressible flow stability theory was shown to reduce to the incompressible limit as $M \rightarrow 0$, but was not correlated with data because of the lack of suitably detailed measurements to use as input to the theory. In the present work the formulation of the compressible flow theory given in Ref. 1 has been modified in that a revised energy matching condition was developed. In addition some analysis of the theory has been made with respect to the mechanisms of rotating stall in supersonic flows.

A portion of the analysis given in Ref. 1 will be recounted briefly for the sake of completeness and the ensuing analysis. The blade row is modeled by a finite thickness actuator shown in Figure 1. The mean flows upstream and downstream of the actuator have uniform swirl. The upstream flow region is denoted by 1 and the downstream region by 2. Briefly the assumptions inherent in this type of modeling are:

1. The blade row has high hub-to-tip ratio
2. The annular area is constant
3. The flow disturbances have wave lengths in the circumferential direction (y-direction) which are large compared to either the blade spacing or chord.
4. The local performance of the blade row is only a function of the local inlet swirl and dynamic pressure and may be obtained in a quasi-steady fashion from the steady state performance data.

Quantities in a blade fixed coordinate system are denoted with a subscript o. The transformation between blade fixed and duct fixed coordinates is given by

$$x_o = x$$
$$y_o = y - W_b t$$
$$t_o = t$$

where W_b is the blade velocity in the duct fixed system. This velocity is given in non-dimensional form by $\bar{\Omega}_i = \frac{W_b}{U_i}$ where i denotes the flow region and U_i is the mean axial flow in region i. The mean absolute swirl angle in each region is denoted as $\bar{\beta}_i$ and the tangent of $\bar{\beta}_i$ is defined as S_i the absolute swirl. The relative swirl with respect to the blade row is given by $\mathcal{S}_i = S_i - \Omega_i$.

Following Refs. 1 and 2, all of the total flow quantities, which are denoted by a hat, are decomposed into steady and unsteady parts as

$$\hat{U}_i = U_i + u_i(t)$$
$$\hat{W}_i = W_i + w_i(t)$$
$$\hat{P}_i = P_i + p_i(t)$$
$$\hat{\rho}_i = R_i + \rho_i(t)$$

where $\hat{P}$ and $\hat{\rho}$ are the pressure and density, respectively, and the i denotes the flow region. The steady parts of each quantity are constants. The assumptions on the unsteady flow are basically the same as in the incompressible case, i.e., the flow outside blade rows is considered inviscid, so that frictional and heat conduction effects are neglected. Generally, however, the flow will be rotational to reflect the losses incurred in the blade row. The unsteady disturbance quantities are assumed to be much smaller than the steady quantities so that the equations of motion can be linearized about the steady flow.

The resulting linearized equations of motion are those of continuity, x- and y- momentum and energy; namely,

$$\frac{\partial \rho_i}{\partial t} + U_i \frac{\partial \rho_i}{\partial x} + W_i \frac{\partial \rho_i}{\partial y} + R_L \left[\frac{\partial u_i}{\partial x} + \frac{\partial w_i}{\partial y} \right] = 0 \tag{1}$$

$$\frac{\partial u_i}{\partial t} + U_i \frac{\partial u_i}{\partial x} + W_i \frac{\partial u_i}{\partial y} + \frac{1}{R_i} \frac{\partial p_i}{\partial x} = 0 \tag{2}$$

$$\frac{\partial w_i}{\partial t} + U_i \frac{\partial w_i}{\partial x} + W_i \frac{\partial w_i}{\partial y} + \frac{1}{R_i} \frac{\partial p_i}{\partial y} = 0 \tag{3}$$

$$\frac{\partial (p_i - a_i^2 \rho_i)}{\partial t} + U_i \frac{\partial (p_i - a_i^2 \rho_i)}{\partial x} + W_i \frac{\partial (p_i - a_i^2 \rho_i)}{\partial y} = 0 \tag{4}$$

where the speed of sound a_i is given by $a_i^2 = \gamma P_i / R_i$ and is constant in each flow region; γ is the ratio of specific heats. The major difference between this problem and the corresponding one for incompressible flow is the appearance of one more unknown, namely the density, and one more governing equation, the energy equation. Eqs. (1) to (4) can be solved by assuming solutions of the form

$$u_i(x,y,t) = \mathcal{U}_i(x)\, e^{j(\sigma t + \frac{ny}{r})} \tag{5}$$

$$\omega_i(x,y,t) = \mathcal{L}_i(x)\, e^{j(\sigma t + \frac{ny}{r})} \tag{6}$$

$$p_i(x,y,t) = \mathcal{M}_i(x)\, e^{j(\sigma t + \frac{ny}{r})} \tag{7}$$

$$\rho_i(x,y,t) = \mathcal{N}_i(x)\, e^{j(\sigma t + \frac{ny}{r})} \tag{8}$$

Here $\sigma = \sigma_R + j\sigma_i$ and n is the number of stall cells and r is the mean radius of the blade row. The resulting disturbance is spatially periodic in the y direction with period $2\pi r/n$. The flow is neutrally stable if $\sigma_i = 0$, unstable if $\sigma_i < 0$ and stable if $\sigma_i > 0$.

Since the system of differential equations has constant coefficients the solutions for $\mathcal{U}_i$, $\mathcal{L}_i$, $\mathcal{M}_i$ and $\mathcal{N}_i$ are expected to be of the form $e^{\alpha x}$. Using this form in Eqns. (5) through (8) and substituting into Eqs. (1) through (4) results in

$$\mathcal{U}_i = D_i e^{\alpha_{3i} x} - A_i \frac{\alpha_{1i}}{R_i U_i (\alpha_{1i} - \alpha_{3i})} e^{\alpha_{1i} x} - B_i \frac{\alpha_{2i}}{R_i U_i (\alpha_{2i} - \alpha_{3i})} e^{\alpha_{2i} x} \tag{9}$$

$$\mathcal{L}_i = D_i \frac{jr}{n} \alpha_3 e^{\alpha_{3i} x} - A_i \frac{jn}{r R_i U_i} \frac{1}{(\alpha_{1i} - \alpha_{3i})} e^{\alpha_{1i} x} - B_i \frac{jn}{r R_i U_i} \frac{1}{(\alpha_{2i} - \alpha_{3i})} e^{\alpha_{2i} x} \tag{10}$$

$$m_i = A_i e^{\alpha_{1i} x} + B_i e^{\alpha_{2i} x} \tag{11}$$

$$n_i = \frac{1}{a_i^2} m_i + E_i e^{\alpha_{3i} x} \tag{12}$$

where

$$\alpha_{1i} = \frac{j m_i m_i + \frac{n}{r}\left\{1 - M_i^2\left(1 + \frac{r^2}{n^2} m_i^2\right)\right\}^{1/2}}{1 - M_i^2} \tag{13}$$

$$\alpha_{2i} = \frac{j m_i m_i + \frac{n}{r}\left\{1 - M_i^2\left(1 + \frac{r^2}{n^2} m_i^2\right)\right\}^{1/2}}{1 - M_i^2} \tag{14}$$

$$\alpha_{3i} = \frac{-j}{U_i}\left(C + W_i \frac{n}{r}\right) \tag{15}$$

and

$$m_i = \frac{1}{U_i}\left(C + \frac{n}{r} W_i\right) = j\alpha_{3i}$$

$$M_i = \frac{U_i}{a_i} \text{ (axial Mach number)}$$

The A_i, B_i, D_i and E_i are constants to be determined by the matching conditions. Normally, since there are four simultaneous differential equations that we are solving there would be four values of the α_{ki} obtained. However for this particular system α_{3i} is a double root. Nevertheless four linearly independent solutions can be obtained for this case using the three α_{ki}.

The terms of the disturbance quantities with exponential factors α_{1i} and α_{2i} correspond to irrotational disturbances. Those terms of U_i and w_i with exponential factors α_{3i} correspond to vorticity waves convected with the mean flow speed. The E_i term of the density disturbance corresponds to a convected entropy wave as will be seen by the following. For a perfect gas the entropy, s_i, in flow region i is given by the following expression

$$s_i = \frac{R}{\gamma-1} \ln \frac{\hat{P}_i}{(\hat{\rho}_i)^\gamma} + s_0 \tag{16}$$

where s_0 is a reference value and R is the gas constant for the particular gas under consideration. Using the linearizing assumptions this becomes

$$s_i \approx s_0 + \frac{R}{\gamma-1}\left\{\ln \frac{P_i}{(R_i)^\gamma} + \frac{1}{P_i}\left(p_i - a_i^2 \rho_i\right)\right\} \tag{17}$$

The only non-constant terms in this expression are the p_i and ρ_i terms and

$$p_i - a_i \rho_i = -E_i\, e^{\alpha_{3i} x + j(\omega t + n y/r)} \tag{18}$$

At this point it should be noted that disturbance solutions corresponding to Eqs. (9) through (12) have been given by Smith.[3] The solutions presented in Ref. 3 are, however, in error by the omission of the E_i term in the density perturbation (the entropy wave term). However the entropy and the vorticity are related by Crocco's theorem which is given in Ref. 4 as.

$$T \operatorname{grad} s + \vec{V} \times \vec{\xi} = \operatorname{grad} h_0 + \frac{\partial \vec{V}}{\partial t} \tag{19}$$

where T is the temperature, $\vec{V}$ is the velocity vector, $\vec{\xi}$ is the vorticity vector and h_0 is the total enthalpy. Hence, it is not consistent to retain the vorticity disturbance terms without the entropy disturbance terms in the disturbance solutions.

Thus far the solution for the disturbance velocities contain eight undetermined constants namely the A_i, B_i, D_i and E_i. For wholly subsonic

flow these constants are determined by requiring bounded flow far upstream and downstream, requiring irrotational flow upstream of the blade row, and by applying matching conditions across the blade row. The requirement for bounded flow far upstream and downstream results in $A_1 = B_2 = 0$. The requirement for irrotational flow upstream of the blade row results in $D_1 = E_1 = 0$. The remaining four constants are determined by applying matching conditions across the actuator which are derived from the continuity equation, the axial momentum equation (with losses), the energy equation and the blade row steady-state turning performance.

The matching conditions are derived using the notation and symbols shown in Figure 1 and are generally written in the blade fixed coordinate system. The conservation of mass flow across the actuator gives the mean flow quantities $U_1 R_1 = U_2 R_2$ and for the unsteady quantities

$$U_1 \rho_1 + u_1 R_1 - U_2 \rho_2 - u_2 R_2 + \cos\delta \frac{\partial}{\partial t} \int_0^{\ell} \rho \, dS = 0 \tag{20}$$

The quantities with a subscript 1 are evaluated at $x_{o1} = 0$ and y_{o1} ; the quantities with a subscript 2 are evaluated at $x_{o2} = \ell \cos\delta$ and $y_{o2} = y_{o1} + \ell \sin\delta$ The integral term in Eq. (20) is evaluated by assuming a linear variation in the integrand between 0 and ℓ.

It is assumed that the turning performance of the blade row may be expressed as

$$\hat{s}_2 = G(\hat{s}_1) \tag{21}$$

where G represents the steady state turning of the blade row functionally. Linearizing this relation about its steady-state value gives

$$\omega_2 - s_2 U_2 = G'(s_1) \frac{U_2}{U_1} (\omega_1 - s_1 U_1) \tag{22}$$

where

$$G'(s_1) \equiv \left. \frac{\partial G}{\partial s_1} \right|_{s_1}$$

The vector form of the momentum equation may be put in the following form

$$\frac{\partial}{\partial t}\oint \vec{V}\cdot d\vec{r} - \oint (\vec{V}\times\vec{\xi})\cdot d\vec{r} = -\oint \left(\frac{\hat{f}_e}{\hat{\rho}_2}\nabla\hat{\rho}\right)\cdot d\vec{r} + \oint \vec{F}\cdot d\vec{r} \qquad (23)$$

where $d\vec{r}$ is the differential of the position vector to points on the contour C in Figure 1. The line integrals are taken around this contour. The friction force vector, $\vec{F}$, is most easily defined in Cortesian Tensor notation. Let $x_1 = x$ and $x_2 = y$ then the ith component of $\vec{F}$ is $\frac{1}{\rho}\frac{\partial \tau_{ij}}{\partial x_j}$ where the summation convention should be used and τ_{ij} is the viscous stress acting in x_j direction on planes perpendicular to x_i. For laminar flows the τ_{ij} may be computed using the Newtonian assumption and Stokes hypothesis. For turbulent flows the viscous stress are usually given empirically. Eq. (23) may be evaluated as in Ref. 2 to give

$$\frac{\partial}{\partial t_0}(W_{o_1} - W_{o_2}) - \sec\delta\,\frac{\partial}{\partial t_0}\int_0^{\ell}\frac{\partial U}{\partial y}\,ds - U_2\,\eta_{o_2}$$
$$-U_1\left\{\left[\chi + \frac{\delta_1}{2}(1+\delta_1^2)\chi'\right]\frac{\partial U_{o_1}}{\partial y_0} + \left[\chi\delta_1 - \frac{1}{2}(1+\delta_1^2)\chi'\right]\frac{\partial W_{o_1}}{\partial y_0}\right\} = 0 \qquad (24)$$

where χ is a loss coefficient for steady flow defined by.

$$\chi = \frac{1}{R_1}\,\frac{(P_{T_{o_1}} - P_{T_{o_2}})}{\frac{1}{2}(U_{o_1}^2 + W_{o_1}^2)}$$

where $P_{T_{o_i}}$ is the steady-state total pressure relative to the blade row in flow region i. Functionally, it is assumed that

$$\chi = \chi(\delta_1) \qquad (25)$$

so that

$$\chi' = \frac{\partial \chi}{\partial \delta_1}$$

The remaining matching condition comes from the energy equation. An energy matching condition was derived in Ref. 1, however, this matching condition required the evaluation of the integral of a dissipation function through the blade row. This was accomplished by assuming linear variations of the quantities to be integrated based upon their values immediately upstream and

downstream of the actuator. This assumption has also been used to evaluate integrals appearing in the continuity and momentum matching conditions, but is not appropriate for evaluating the integral of the dissipation function. The dissipation function involves the product of the viscosity and squares of derivatives of the velocity components. In the actual flow through the blade row these derivatives may be large thus estimating these derivatives from the model of the upstream and downstream flows which are composed of constant values for the mean flow velocities plus small unsteady components is inaccurate. Also the form of the dissipation function used is only strictly valid for laminar flows. A form of the energy equation has been found which avoids evaluation of the dissipation function and will now be derived.

The starting point is the basic energy conservation equation given in Ref. 5. Neglecting heat transfer by conduction this equation is

$$\int_{\Sigma} V_i (\bar{\pi}_{ij} n_j)\, d\Sigma - \int_{\Sigma} E_t (\rho V_j n_j)\, d\Sigma = \frac{\partial}{\partial t} \int_{V_0} \rho E_t \, dV_0 - \int_{V_0} \frac{\partial Q}{\partial t} dV_0 \qquad (26)$$

and is applied to an arbitrary control volume, V_0 , bound by the surface Σ. The Cartesian tensor notation and summation convention are used here again. The integrals appearing on the left hand side of the equations are surface integrals where V_i is the ith component of the velocity vector $\vec{V}$, n_i is the ith component of the outward normal $\vec{n}$ at the bounding surface. The stresses at the control volume surface are $\bar{\pi}_{ij}$ and are composed of the pressure forces and viscous stresses such that

$$\bar{\pi}_{ij} = \tau_{ij} - p\,\delta_{ij}$$

when p is the static pressure; τ_{ij} , are the viscous stresses previously defined and δ_{ij} is the Kronecker delta function having the property

$$\delta_{ij} = 1 \qquad i = j$$
$$= 0 \qquad i \neq j$$

E_t is the sum of the internal energy, e , and kinetic energy per unit mass of fluid so that

$$E_t = e + \frac{1}{2} U_i U_i$$

and $e = c_v T$ for a thermally perfect gas where T is the temperature and c_v is the specific heat at constant volume. $\frac{\partial Q}{\partial t}$ is the rate of heat produced per unit volume in V_o and is due to friction in this case.

Basically Eq. (26) states that the rate of work performed on the control volume by the surface stresses minus the rate at which energy is transported out of the volume is equal to the time rate of change of energy inside the volume minus the heat produced in the volume. To apply Eq. (26) to the present problem, choose a control volume (area for the two-dimensional case) bounded by the curve Ⓒ in Figure 1. In the figure, Ⓒ is drawn so that B-C and A-D correspond to blade surfaces. This is not necessary but these two sides of the control volume should be chosen such that they are parallel to the blade chord lines. The assumption will be made that flow in the passage is parallel to the blade chords so that convection of energy out these sides of the control volume can be neglected.

We now use an argument given by Vavra[6] that the frictional heat is immediately and equally transmitted to all points in a fluid particle as it moves along its path. Further it is assumed that the frictional heating is equivalent to the work of the frictional forces acting on the surface of the particle. Under these assumptions for the control volume chosen the viscous portion of the surface stress work integral (first integral on left hand side of Eq. 26) is cancelled by the heat production integral (last integral on right hand side of Eq. 26). Then Eq. (26) may be simplified to

$$\int_0^\epsilon \hat{U}_1 \hat{p}_1 d\tilde{y} - \int_0^\epsilon \hat{U}_2 \hat{p}_2 d\tilde{y} + \int_0^\epsilon \hat{\rho}_1 \hat{U}_1 \hat{E}_{t_1} d\tilde{y} - \int_0^\epsilon \hat{\rho}_2 \hat{U}_2 \hat{E}_{t_2} d\tilde{y} = \cos\delta \int_0^\epsilon \int_0^\ell \frac{\partial}{\partial t}\left(\hat{\rho}\hat{E}_t\right) ds\, d\tilde{y} \tag{27}$$

where $s, \tilde{y}$ are a sheared coordinate system parallel to the blade chord and cascade axis respectively. Since ϵ is arbitrary

$$\hat{p}_1 \hat{U}_1 - \hat{p}_2 \hat{U}_2 + \hat{\rho}_1 \hat{U}_1 \hat{E}_{t_1} - \hat{\rho}_2 \hat{U}_2 \hat{E}_{t_2} = \cos\delta \int_0^\ell \frac{\partial}{\partial t}\left(\hat{\rho}\hat{E}_t\right) ds \tag{28}$$

After applying the linearizing assumptions and use of the mean flow continuity equation this equation can be split into a steady part

$$\frac{1}{\gamma-1}\frac{P_2}{R_2}+\frac{1}{2}\left[U_2^2+(W_2-W_b)^2\right]=\frac{1}{\gamma-1}\frac{P_1}{R_1}+\frac{1}{2}\left[U_1^2+(W_1-W_b)^2\right] \tag{29}$$

which essentially states that the mean total enthalpy is conserved and an unsteady part

$$\begin{aligned}
&\frac{\gamma}{\gamma-1}U_1 p_1+\rho_1\left\{E_0U_1-\frac{\gamma}{\gamma-1}\frac{P_1U_1}{R_1}\right\}+u_1\left\{R_1U_1^2+E_0R_1\right\}+w_1R_1U_1(w_1-w_b)\\
&-\frac{\gamma}{\gamma-1}U_2p_2-\rho_2\left\{E_0U_2-\frac{\gamma}{\gamma-1}\frac{P_2U_2}{R_2}\right\}-u_2\left\{R_2U_2^2+E_0R_2\right\}-w_2R_2U_2(w_2-w_b)\\
&=\ell/2\cos\delta\left\{\frac{\dot{p}_1}{\gamma-1}+\dot{\rho}_1\left(E_0-\frac{\gamma P_1}{(\gamma-1)R_1}\right)+\dot{u}_1R_1U_1+\dot{w}_1R_1(w_1-w_b)\right.\\
&\left.+\frac{\dot{p}_2}{\gamma-1}+\dot{\rho}_2\left(E_0-\frac{\gamma P_2}{(\gamma-1)R_2}\right)+\dot{u}_2R_2U_2+\dot{w}_2R_2(w_2-w_b)\right\}
\end{aligned} \tag{30}$$

Here a dot over a quantity signifies its time derivative and the integral appearing on the right hand side of Eq. (28) has been evaluated by assuming a linear variation of the integrand. Also we have let

$$E_0=\frac{1}{\gamma-1}\frac{P_i}{R_i}+\frac{1}{2}\left[U_i^2+(w_i-w_b)^2\right]$$

having the same value for both i = 1 and 2 because of Eq. (29). (This is the mean total enthalpy of the flow.)

It will be noted, by inspection of Eq. (29) and (30), that the viscosity does not explicitly appear in the energy matching conditions. This appears to be consistent with the energy equation used for one-dimensional flow in pipes with friction. (see Ref. 7).

Eqs. (20), (22), (24) and (30) supply the required relation to determine the unknown constants. Substituting Eqs. (9) through (12) in these equations results in a system of homogeneous equations of the form

$$[A] \begin{bmatrix} B_1 \\ D_2 \\ A_2 \\ E_2 \end{bmatrix} = 0 \tag{31}$$

where the A matrix has elements A_{ij}. The characteristic equation of the system which gives the allowable values of C is then

$$\det [A] = 0 \tag{32}$$

The elements of the A matrix are:

$$A_{11} = \lambda \frac{j}{2} \frac{n}{r} \ell M_1^2 \cos\delta - M_1^2 + \frac{I_1}{I_2}$$

$$A_{12} = \frac{R_1 U_1^2}{U_2}$$

$$A_{13} = M_2^2 \frac{U_1}{U_2} - j \lambda M_2^2 \left(\frac{a_1}{a_2}\right)^2 \frac{n}{r} \ell \cos\delta - \frac{U_1 I_1}{U_2 I_2}$$

$$A_{14} = U_1 U_2 \left(1 + j \frac{\lambda}{2} \frac{U_1}{U_2} \frac{n}{r} \ell \cos\delta\right)$$

$$A_{21} = \frac{G' U_2}{U_1 I_2} \left\{ j (1 - M_1^2) - \mathcal{I}_1 I_2 \right\}$$

$$A_{22} = R_1 U_1 (\xi_2 - \mathcal{I}_2)$$

$$A_{23} = \frac{1}{I_4} \left\{ \mathcal{I}_2 I_3 - j (1 - M_2^2) \right\}$$

$$A_{24} = 0$$

$$A_{31} = \frac{1}{I_4} \left\{ \left(j \left[\chi - \frac{\mathcal{I}_1}{2} (1 + \mathcal{I}_1^2) \chi' \right] - \frac{\lambda}{2} \frac{n}{r} \ell \sec\delta \right) I_1 \right.$$

$$\left. - (1 - M_2^2) \left[\lambda + \chi \mathcal{I}_1 + \frac{1}{2} (1 + \mathcal{I}_1^2) \chi' \right] \right\}$$

$$A_{32} = R_1 U_1 \lambda \left(i \xi_2 + \frac{1}{2} \frac{n}{r} \ell \sec \delta \right) - j \frac{U_2}{U_1} \left(1 + \xi_2^2 \right) R_1 U_1$$

$$A_{33} = \frac{\lambda}{I_4} \left\{ (1 - M_2^2) - \frac{1}{2} \frac{n}{r} \ell \sec \delta I_3 \right\}$$

$$A_{34} = 0$$

$$A_{41} = U_1 + \frac{E_0 U_1}{a_1^2} - \frac{I_1 \left(U_1 + \frac{E_0}{U_1} \right) + j \mathcal{S}_1 (1 - M_1^2) U_1}{I_1 + j \xi_1 \frac{r^2}{n^2} (1 - M_1^2)}$$

$$- j \frac{c}{2} \ell \cos \delta \left\{ \frac{E_0}{a_1^2} + \frac{\mathcal{S}_1 (1 - M_1^2) - I_1}{I_1 - j \xi_1 \frac{r^2}{n^2} (1 - M_1^2)} \right\}$$

$$A_{42} = - R_2 U_2^2 - E_0 R_2 - \frac{r^2}{n^2} \xi_2 \mathcal{S}_2 R_2 U_2^2$$

$$- j \frac{c}{2} \ell R_2 U_2 \cos \delta \left(1 + \frac{r^2}{n^2} \mathcal{S}_2 \xi_2 \right)$$

$$A_{43} = - U_2 - \frac{E_0 U_2}{a_2^2} + \frac{I_3 \left(U_2 + \frac{E_0}{U_2} \right) + j \mathcal{S}_2 (1 - M_2^2) U_2}{I_3 + j \xi_2 \frac{r^2}{n^2} (1 - M_2^2)}$$

$$- j \ell \frac{c}{2} \cos \delta \left\{ \frac{E_0}{a_2^2} - \frac{I_3 + j \mathcal{S}_2 (1 - M_2^2)}{I_3 + j \frac{r^2}{n^2} \xi_2 (1 - M_2^2)} \right\}$$

$$A_{44} = - E_0 U_2 - \frac{\gamma}{\gamma - 1} \frac{P_2 U_2}{R_2} - j c \frac{\ell}{2} \cos \delta \left\{ E_0 - \frac{\gamma}{\gamma - 1} \frac{P_2}{R_2} \right\}$$

where

$$I_1 = j M_1^2 \xi_1 + \left[1 - M_1^2 (1 + \xi_1^2)\right]^{1/2}$$

$$I_2 = j \xi_1 + \left[1 - M_1^2 (1 + \xi_1^2)\right]^{1/2}$$

$$I_3 = j M_2^2 \xi_2 - \left[1 - M_2^2 (1 + \xi_2^2)\right]^{1/2}$$

$$I_4 = j \xi_2 - \left[1 - M_2^2 (1 + \xi_2^2)\right]^{1/2}$$

$$\xi_1 = \lambda + \delta_1$$

$$\xi_2 = \frac{U_1}{U_2} \lambda + \delta_2$$

$$\lambda = \frac{cr}{nU_o} + \bar{\Omega}_1$$

$$M_1 = U_1/a_1$$

$$M_2 = U_2/a_2$$

As may be seen from inspecting the A_{ij} elements of the A matrix Eq. (32) is not a simple polynomial, as in the incompressible flow case, and must be solved numerically. This has not been done yet. However, Eq. (32) reduces to the incompressible limit of Ref. 1 when $\rho_i \to 0$, $a_i \to \infty$ and the numerical results should be the same as those presented in Ref. 1 for incompressible flow.

As mentioned previously the foregoing analysis is limited to wholly subsonic flows. This limitation results because of the steady-state blade row performance assumed. The basic solutions, Eqs. (9) through (12) for the disturbance quantities are valid for supersonic flows. Examining the exponential factors α_{1i} and α_{2i} (Eqs. 13 and 14) appearing in the expressions for the velocity disturbances for the case of neutrally stable flows $(C_I = 0)$

it can be seen that the variation with χ changes character when

$$U_1^2 + (W_1 - V_p)^2 > a_1^2 \tag{33}$$

Here $V_p = \frac{-C_R r}{n}$ is the propagation velocity of the wave in the azimuthal direction.

When this inequality occurs the radical terms of Eqs. 13 and 14 change from real to imaginary and the variation with χ changes from damped oscillatory (complex valued α_{ij}) to undamped oscillatory (purely imaginary valued α_{ij}). At this point the disturbances quantities correspond to sound waves that are propagated to upstream infinity. The selection of which values of the α_{ij} apply in each flow region is then determined by the requirement that the waves emanate at the blade row and travel away from it in both the upstream and downstream direction. Put another way, no waves should emanate from either upstream or downstream infinity. Assuming that $W_1 - V_p > 0$, the α_{21} root is used in the upstream flow and the α_{12} root is used in the downstream flow as before.

The condition expressed by relation (33) occurs when the inlet flow becomes supersonic relative to the disturbance wave. Since W_b is negative for a compressor, in the sign convention being used, and since V_p is usually about one half W_b, relation (33) will generally occur at some point after the inlet flow has become supersonic relative to the blades.

There are several flow regimes to consider for nominally supersonic flows dependent upon whether the axial flow is supersonic or not. Further the cases with subsonic axial flows have different characteristics dependent upon whether both the inlet and outlet flows are supersonic relative to the rotor. The steady-state characteristics of cascades operating in these different flow regimes is discussed in Ref. 8. In the present discussion only the case with supersonic axial flow and the case with subsonic axial flow where both the inlet and outlet conditions are supersonic relative to the rotor will be considered.

First the case with subsonic axial flow will be discussed. The steady operational characteristics of the cascade have two properties which are very important to this case. First of all, a supersonic cascade with subsonic

axial flow can only operate in the steady state at a single inlet angle. This condition is often referred to as "unique incidence". Secondly the back pressure (flow angle) far downstream of the cascade is not a unique function of mass flow and inlet conditions to the cascade. A range of back pressures is possible without unstarting the cascade; therefore, the back pressure must be prescribed as part of the boundary conditions for the problem. In addition there is only one-way communications for the unsteady disturbances between upstream and downstream flow fields (assuming that the disturbances are small enough not to unstart a blade passage). Nothing that happens in the downstream flow can influence the upstream flow. Propagation of a disturbance which starts at the trailing edge, upstream through the blade passage, is blocked by the blade surfaces and reflected back into the downstream flow. Therefore the upstream disturbance field may be neglected as far as stability considerations are concerned and there are only three constants (A_2, D_2 and E_2) to be determined. This requires the following revisions to the required matching conditions. First the turning relation, Eq. (22), is dropped. Secondly the loss relation, Eq. (25), should be revised to indicate that now the losses are a function of the downstream flow angle (or static pressure) and this revision incorporated in the vorticity compatability matching condition, Eq. (24). Thirdly the three matching conditions used should be revised to reflect the fact that all the upstream disturbances are now zero. The characteristic equation for this case can be obtained quite simply from Eq. 31 by deleting the first column and second row of the A matrix. In addition the third row must be revised because of the new loss relationship. The resulting equation is however, again, not a simple polynomial and must be solved numerically. This has not been done yet.

For the case of supersonic axial flow the unique incidence does not apply and the outlet conditions are uniquely determined by the inlet conditions. However, there can be no disturbances ahead of the cascade so that, again, there are only three undetermined constants to be determined in the disturbance solutions; namely A_2, D_2 and E_2. At this stage is not clear which matching condition should be dropped. It appears that this question will have to be settled by correlation with experimental data.

These considerations of the different types of compressible flows show that the two-dimensional analysis should be limited to cases where the same type of flow prevails along the entire span of the blade. Moreover it appears that the most significant blade row performance parameters that influences the inception of rotating stall must be substantially different in the supersonic cases. It was concluded in Ref. 2 that the slope of blade row losses with inlet flow angle was the most important performance parameter with respect to the stall boundaries for incompressible flows (this also appears true for wholly subsonic compressible flows). For the case of supersonic flow with subsonic axial flow the blade row losses will be dependent upon the back pressure rather than the inlet flow angle which suggests that the slope of the blade row losses with back pressure may be the controlling factor for this case. The case with supersonic axial flow remains a subject for further analysis.

C. THREE-DIMENSIONAL INCOMPRESSIBLE FLOW STABILITY THEORY

There are basically two ways to study the stability of a system. The first way is to determine under what conditions small disturbances with an oscillatory time behavior are either damped or amplified with time. This is referred to as a stability theory approach and was used in the two-dimensional case. The second method is to disturb the system and examine the time history of the response of the system to determine if the response becomes unbounded with time. The second method is somewhat more general in that it is not necessarily limited to linear systems. However, it involves actually calculating the response of the system for a variety of input disturbances. If this is done numerically, care must be taken to ensure that divergence of the response is actually due to the physics of the problem and not due to instabilities of the numerical algorithm used. It is therefore, usually, better to use a stability analysis if it is tractable.

In the two-dimensional case a stability theory has proved quite useful in understanding the mechanisms of rotating stall and predicting inception conditions for blade rows with high hub-to-tip ratios. However,

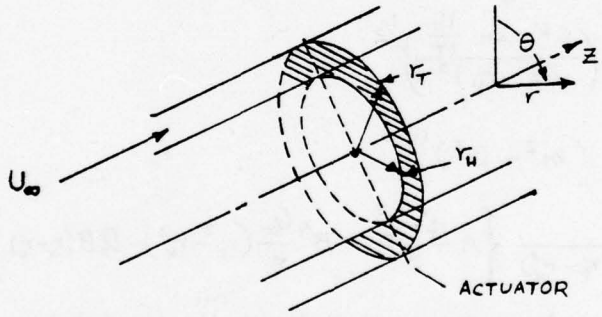
most modern compressors have initial stages with relatively low hub-to-tip ratios and it is thought that three-dimensional effects may be important for these cases. The two-dimensional theory for an isolated blade row provided concise results in that for the incompressible case a closed form expression was obtained for the damping factor and propagation velocity of admissible disturbance solutions (Eqs. 30 Ref. 2). In addition the conditions that apply at the neutral stability boundary could be concisely stated (Eq. 32 Ref. 2). Therefore the stability boundary for a given blade row could be calculated with relatively little numerical effort. The case for two blade rows was only slightly more complicated so that it would be practical to apply this theory to several stages if the appropriate blade row loss and turning performance were available. The conciseness of the results for the two-dimensional case also promoted a physical interpretation and understanding of the results. This situation prompted the formulation of a three-dimensional stability analysis using the same overall approach as in the two-dimensional case. The simplified model for the mean flow developed in Ref. 1 was used. However applying the overall methodology of the two-dimensional problem to the three-dimensional case resulted in a much more complicated problem that did not allow a concise statement of results. Further, sufficient numerical effort would have been required such that physical insight to the problem would be lost. Therefore the implementation of the three dimensional theory was not completed. However the theory has been developed to the point where it could be implemented and this development is presented in the following paragraphs.

General Analysis

As in the two-dimensional case the basic plan of attack was to determine basic solutions for the perturbation velocities and pressures both upstream and downstream of the blade row. It was expected that these disturbance solutions would contain unknown constants that would be determined by the matching conditions across the blade row. These matching conditions would result in a characteristic equation for the damping factors and propagation velocities for admissible solutions. The major difficulty arose when the downstream disturbance velocities could not be determined in analytical form.

Coupling a numerical solution for the downstream disturbance velocities with the characteristic equation obtained from the matching conditions leads to the requirement for substantial numerical effort to implement the analysis. The implementation was not completed but was carried far enough that the detailed mechanics of obtaining a solution are relatively clear. The completed portion of the analysis will be given along with the intended method of solution.

The simplified actuator sheet model developed in Ref. 1 was used as the model for the basic steady flow. Basically the flow considered is that in a constant area annulus. The blade row is modeled by an actuator sheet. The inner radius of the annulus is denoted by r_H and the outer radius by r_T. The following sketch shows the coordinate system and geometry.



The mean flow is axially symmetric. The axial, radial and azimuthal velocity components are designated by U, V and W respectively. From Ref. 1 we have that a stream function Ψ exists such that

$$V = -\frac{1}{r}\Psi_z \quad ; \quad U = \frac{1}{r}\Psi_r$$

and the approximate solutions for Ψ and the other flow quantities are given by

$$\Psi = U_\infty \frac{r^2}{2} + a_2(z)(K_0 + K_1 r + r^2) \tag{34}$$

$$W = \frac{B}{r}\Psi + \frac{D_2}{r} \tag{35}$$

$$H = A\Psi + D_1 \tag{36}$$

where H is the total pressure divided by the density, U_∞ is the undisturbed axial velocity far upstream of the blade row, and

$$K_0 = r_T r_H$$

$$K_1 = -(r_T + r_H)$$

The function $a_2(z)$ has two forms dependent upon $z \gtrless 0$. Upstream when

$$z < 0$$

$$a_2 = G_2 e^{mz} \tag{37}$$

and for $z > 0$

$$a_2 = \frac{G_2}{M}\left(M + m - m e^{-Mz}\right) \tag{38}$$

where

$$m = \left(\frac{6K_1 \ln \frac{r_H}{r_T}}{(r_T - r_H)^3}\right)^{1/2}$$

$$M = (m^2 - B^2)^{1/2}$$

$$G_2 = \frac{6}{M(M+m)(r_T - r_H^3)}\left\{A\frac{r_T^3 - r_H^3}{3} - B^2\frac{U_\infty}{6}(r_T^3 - r_H^3) - D_2 B(r_T - r_H)\right\}$$

However, in the ensuing development we will not distinguish between the two forms of a_2 until necessary. Also A, B, D_1 and D_2 are constants. Upstream of the blade row A, B and D_2 are zero. Downstream of the blade row they may be determined by using two-dimensional cascade data in a strip theory fashion, as in Ref. 1, or they may be determined to give a best fit to experimental velocity distributions if they are known. In any event, they are considered as known quantities for the present analysis.

The total velocity components and pressure, which are denoted by a hat are decomposed into steady and unsteady parts as follows

$$\hat{U} = U(z,r) + \tilde{u}(z,r)\, e^{j(\sigma t + n\theta)} \tag{39a}$$

$$\hat{V} = V(z,r) + \tilde{V}(z,r)\, e^{j(ct+n\theta)} \tag{39b}$$

$$\hat{w} = W(z,r) + \tilde{w}(z,r)\, e^{j(ct+n\theta)} \tag{39c}$$

$$\hat{p} = p(z,r) + \tilde{p}(z,r)\, e^{j(ct+n\theta)} \tag{39d}$$

The major difference between these forms and those used in the two-dimensional case is that the steady parts are no longer constants but are determined from Eqs. (34) through (36). Assuming that the steady part of each quantity is much larger than the unsteady part, the momentum and continuity equations may be linearized into the following:

$$jc\tilde{v} + V\frac{\partial \tilde{v}}{\partial r} + \tilde{v}\frac{\partial V}{\partial r} + jn\frac{W}{r}\tilde{w} + U\frac{\partial \tilde{v}}{\partial z} + \tilde{u}\frac{\partial V}{\partial z} - 2W\frac{\tilde{w}}{r} = -\frac{1}{\rho}\frac{\partial \tilde{p}}{\partial r} \tag{40}$$

$$jc\tilde{w} + V\frac{\partial \tilde{w}}{\partial r} + \tilde{v}\frac{\partial W}{\partial r} + jn\frac{W}{r}\tilde{w} + U\frac{\partial \tilde{w}}{\partial z} + \tilde{u}\frac{\partial W}{\partial z} + \tilde{v}\frac{W}{r} + V\frac{\tilde{w}}{r} = -\frac{1}{\rho r}jn\tilde{p} \tag{41}$$

$$jc\tilde{u} + V\frac{\partial \tilde{u}}{\partial r} + \tilde{v}\frac{\partial U}{\partial r} + jn\frac{W}{r}\tilde{u} + U\frac{\partial \tilde{u}}{\partial z} + \tilde{u}\frac{\partial U}{\partial z} = -\frac{1}{\rho}\frac{\partial \tilde{p}}{\partial z} \tag{42}$$

$$\frac{1}{r}\frac{\partial}{\partial r}(r\tilde{v}) + j\frac{n}{r}\tilde{w} + \frac{\partial \tilde{u}}{\partial z} = 0 \tag{43}$$

Eqs. (40), (41) and (42) are the r, θ and z momentum equations respectively and Eq. (43) is the continuity equation.

Based upon the approximate techniques used in Ref. 1 solutions for the disturbance quantities are sought in the form

$$\tilde{u} = \frac{u_0(z)}{r} + u_1(z) \tag{44a}$$

$$\tilde{v} = \frac{V_0(z)}{r} + V_1(z) + V_2(z)r \tag{44b}$$

$$\tilde{w} = \frac{W_0(z)}{r} + W_1(z) + W_2(z)r \tag{44c}$$

$$\tilde{p} = p_0(z) + p_1(z)r + p_2(z)r^2 \tag{44d}$$

Requiring no flow through the annulus walls and the continuity equation, Eq. (43) to be satisfied for all r results in.

$$\tilde{v} = V_2(z)\left(\frac{K_0}{r} + K_1 + r\right) \tag{45}$$

$$\tilde{w} = \frac{j}{n}\left\{K_1 V_2 + u_0' + r\left[2V_2 + u_1'\right]\right\} \tag{46}$$

where primes denote differentiation with respect to z. Thus there are six remaining functions of z to be determined; namely u_0, u_1, V_2, p_0, p_1 and p_2. The six required equations to determine these functions will be determined in different fashions for the upstream and downstream flows.

Upstream Flow Disturbances

The upstream flow is much easier to analyze since it is irrotational and the velocity components may be solved for independently of the pressure. Let the ith component of vorticity be denoted by Ω_i and let

$$\Omega_i = \tilde{\Omega}_i e^{j(ct+n\theta)}$$

then

$$\tilde{\Omega}_z = \frac{1}{r}\left(\frac{\partial}{\partial r}(r\tilde{w}) - jn\tilde{v}\right) \tag{47a}$$

$$\tilde{\Omega}_r = j\frac{n\tilde{u}}{r} - \frac{\partial \tilde{w}}{\partial z} \tag{47b}$$

$$\tilde{\Omega}_\theta = \frac{\partial \tilde{v}}{\partial z} - \frac{\partial \tilde{u}}{\partial r} \tag{47c}$$

Now the equations required to solve for u_o, u_1 and V_2 are obtained by substituting Eqs. (44a), (45) and (46) into Eqs. (47) and requiring

$$\int_{r_T}^{r_H} \tilde{\Omega}_r \cdot dr = 0$$

This leads to the following system of ordinary differential equations for the unknown function

$$k_1 V_2' + \frac{k_9}{K_o} u_o = 0 \tag{48a}$$

$$V_2 (2k_{10} - k_1 n^2) + k_9 u_o' + 2k_{10} u_1' = 0 \tag{48b}$$

$$k_9 u_o'' + k_{10} u_1'' - n^2 \frac{k_9}{K_o} u_o - n^2 k_8 u_1 = 0 \tag{48c}$$

where

$$k_1 = K_o \ln\left(\frac{r_T}{r_H}\right) - \frac{1}{2}(r_T^2 - r_H^2)$$

$$k_8 = \ln\left(\frac{r_T}{r_H}\right)$$

$$k_9 = (r_T - r_H)$$

$$k_{10} = \frac{1}{2}(r_T^2 - r_H^2)$$

Since this system has constant coefficients the solution will be of the form

$$u_o = c_o e^{\lambda z}$$

$$u_1 = c_1 e^{\lambda z}$$

$$V_2 = c_2 e^{\lambda z}$$

Substitution of these forms in Eqs. (48) gives the following equation for λ

$$\lambda^4 - \lambda^2 (\alpha_{21} + \alpha_{10}) + (\alpha_{10}\alpha_{21} - \alpha_{20}\alpha_{11}) = 0 \qquad (49)$$

where

$$\alpha_{10} = \frac{1}{K_0}\left(3n^2 - \frac{2k_{10}}{k_1}\right)$$

$$\alpha_{11} = 2n^2 \frac{k_8}{k_9}$$

$$\alpha_{20} = \frac{2k_9}{K_0}\left(\frac{1}{k_1} - \frac{n^2}{k_{10}}\right)$$

$$\alpha_{21} = -n^2 \frac{k_8}{k_{10}}$$

The real positive roots of Eq. (49) provide the values of λ of interest. Once these have been determined Eqs. (48) provide two relations involving c_0, c_1 and c_2, namely

$$c_3 = \frac{k_9}{K_0 k_1 \lambda}$$

and

$$-\frac{c_1}{c_0} = \frac{\lambda^2 k_9 - n^2 \frac{k_9}{k_{10}}}{k_{10}\lambda^2 - n^2 k_8}$$

Thus for each value of λ there is one undetermined constant associated with the upstream disturbance velocities that remains to be determined by the matching conditions. The p_i may be determined by substituting the above solutions for u_0, u_1 and V_2 into Eqs. (40), (41) and (42). At this point we note that the upstream disturbance velocities are independent of the mean flow. This is a consequence of the irrotationality of the upstream flow. This fact also allows us to construct an exact solution for the upstream-flow disturbances that may be compared to the approximate solutions just found. Since the upstream flow is irrotational, a velocity potential Φ exists such that

$$\bar{\Phi} = \phi(z,r)e^{j(\sigma t + n\theta)}$$

where $\tilde{u} = \phi_z$, $\tilde{v} = \phi_r$, $\tilde{w} = j n \phi$

and the continuity equation (Eq. (43)) becomes

$$\phi_{zz} + \phi_{rr} + \frac{1}{r}\phi_r - \frac{n^2}{r}\phi = 0$$

Then ϕ has a Fourier Bessel expansion given by

$$\phi(z,r) = \sum_{i=0}^{\infty} \left[S_{1i} \cdot J_n\left(\alpha_i \frac{r}{r_T}\right) + S_{2i} \cdot Y_n\left(\alpha_i \frac{r}{r_T}\right) \right] e^{\alpha_i \frac{z}{r_T}} \qquad (50)$$

Here, J_n and Y_n are the n^{th} order Bessel function of the first and second kind, respectively, The α_i are the roots of

$$Y_n'(\alpha_i) J_n'(\alpha_i R) - J_n'(\alpha_i) Y_n'(\alpha_i R) = 0 \qquad (51)$$

The primes denote differentiation with respect to r , and R is the hub-to-tip ratio, r_H/r_T. The constants S_{1i} and S_{2i} satisfy the following relation

$$-\frac{S_{1i}}{S_{2i}} = \frac{Y_n'(\alpha_i)}{J_n'(\alpha_i)} = \frac{Y_n'(\alpha_i R)}{J_n'(\alpha_i R)} \qquad (52)$$

These constants are determined for each α_i by prescribing appropriate boundary conditions at the blade row ($z = 0$) which result from matching $\tilde{u}$ and $\tilde{v}$ with the downstream solution and by prescribing a turning relation through the blade row.

Eq. 51 results from the condition of no flow through the duct walls and the α_i which satisfy this equation must be determined numerically. Tables of these roots are given by Bauer[9] for $0 \le n \le 11$ and $0 \le i \le 9$.

A comparison of the exponential decay factors for $R = .8$ (corresponding to the Calspan/AF annular cascade tests) will now be made. Eq. 49 yields two solutions for the decay factor of the approximate solution which corresponds to the first two terms in the Fourier-Bessel expansion of the exact solution. For $n = 1$ the value of α_0 given in Ref. 8 is 1.11337 and that for

α_1 is 15.77771 indicating that the subsequent terms in the exact solution decay very rapidly as distance from the blade row is increased. The agreement between the decay factors of the exact and approximate solutions for the first term is excellent as shown in the following table.

COMPARISON OF EXPONENTIAL DECAY FACTOR IN UPSTREAM DISTURBANCE SOLUTIONS

	1st Term in Exact Bessel Function Expansion α_0	Approximate Velocity Components λr_T
n = 1	1.11337	1.11337
n = 2	2.22646	2.22652
n = 5	5.56194	5.56233
n = 10	11.07246	11.09664

The axial decay factors for the second term in the approximate solution are about ten percent high. However, overall, this type of agreement between the approximate and exact solution indicate that the approximate method should be sufficiently accurate.

Downstream Flow Disturbances

For the downstream flow the six unknown functions u_0, u_1, v_2, p_0, p_1 and p_2 are determined by substituting Eqs. (44a), (45) and (46) into Eqs. (40) through (49), integrating between r_H and r_T, and taking the first integral moment of these equations between r_H and r_T. This leads to a system of ordinary differential equations of the form

$$\Gamma_{i1} v_2 + \Gamma_{i2} v_2' + \Gamma_{i3} u_0 + \Gamma_{i4} u_0' + \Gamma_{i5} u_0''$$

$$+ \Gamma_{i6} u_1 + \Gamma_{i7} u_1' + \Gamma_{i8} u_1'' + \Lambda_{i1} p_0 + \Lambda_{i2} p_0'$$

$$+\Lambda_{i3}p_1+\Lambda_{i4}p_1'+\Lambda_{i5}p_2+\Lambda_{i6}p_2' = 0 \qquad (53)$$

for $i = 1, 2, \ldots, 6$

The detailed expressions for the Γ_{ij} and Λ_{ij} are given in Appendix A. The Γ_{ij} are functions of z because a_2 is a function of z. The Λ_{ij} are constant terms. This allows the p_i to be eliminated from the system of equations arriving at the somewhat simplified form

$$F_{i1}V_2 + H_{i1}V_2' + P_{i1}V_2'' + F_{i2}u_0 + H_{i2}u_0' + P_{i2}u_0''$$
$$+ Q_{i2}u_0''' + F_{i3}u_1 + H_{i3}u_1' + P_{i3}u_1'' + Q_{i3}u_1''' = 0 \qquad (54)$$

for $i = 1, 2, 3$

The F_{ij}, H_{ij}, P_{ij} and Q_{ij} are functions of z given in the Appendix A. It will be noted here that the functional dependence upon z is of a special form displayed as follows:

$$F_{ij} = \mathcal{F}_{ij} + f_{ij}e^{-Mz} \qquad (55a)$$

$$H_{ij} = \mathcal{H}_{ij} + h_{ij}e^{-Mz} \qquad (55b)$$

$$P_{ij} = \mathcal{P}_{ij} + p_{ij}e^{-Mz} \qquad (55c)$$

$$Q_{ij} = \mathcal{Q}_{ij} + q_{ij}e^{-Mz} \qquad (55d)$$

The only z dependence is in the exponential factor so that far downstream all the functions approach a constant value. In general closed form solutions to the system of equations (Eqs. (54)) cannot be obtained. There are several approximate methods for solving systems of linear ordinary differential equations with variable coefficients given in Chapter 7 of Ref. 10. These

methods generally result in series expansions in powers of $\bar{z}$. The perturbation quantities will have boundary conditions applied at the actuator ($\bar{z} = 0$) and at downstream infinity ($\bar{z} \to \infty$). A series expansion in terms of powers of $\bar{z}$ is not particularly useful for applying the downstream infinity boundary conditions. However, because of the special form of the coefficients in Eqs. (54) we may use Theorem 8.1 of Reference 11 to construct asymptotic solutions for large $\bar{z}$. Essentially the referenced theorem states that the solution for a system of equations whose coefficients are asymptotically equal to a constant (as noted from Eqs. (55)) is asymptotically equal to the solution of the system with constant coefficients. These asymptotic solutions are most easily found directly from Eqs. (55). Let the asymptotic solution for large $\bar{z}$ for the perturbation amplitude functions be denoted with a superscript star. Then these solutions will be of the form

$$V_2^* = C_1 e^{\lambda \bar{z}} \tag{56a}$$

$$u_0^* = C_2 e^{\lambda \bar{z}} \tag{56b}$$

$$u_1^* = C_3 e^{\lambda \bar{z}} \tag{56c}$$

where λ satisfies

$$\begin{vmatrix} (\mathcal{T}_{11} + \mathcal{H}_{11}\lambda) & (\mathcal{H}_{12}\lambda + \mathcal{P}_{12}\lambda^2) & (\mathcal{H}_{13}\lambda + \mathcal{P}_{13}\lambda^2) \\ (\mathcal{T}_{21} + \mathcal{H}_{21}\lambda + \mathcal{P}_{21}\lambda^2) & (\mathcal{T}_{22} + \mathcal{H}_{22}\lambda + \mathcal{P}_{22}\lambda^2 + \theta_{22}\lambda^3) & (\mathcal{T}_{23} + \mathcal{H}_{23}\lambda + \mathcal{P}_{23}\lambda^2 + \theta_{23}\lambda^3) \\ (\mathcal{T}_{31} + \mathcal{H}_{31}\lambda + \mathcal{P}_{31}\lambda^2) & (\mathcal{T}_{32} + \mathcal{H}_{32}\lambda + \mathcal{P}_{32}\lambda^2 + \theta_{32}\lambda^3) & (\mathcal{T}_{33} + \mathcal{H}_{33}\lambda + \mathcal{P}_{33}\lambda^2 + \theta_{33}\lambda^3) \end{vmatrix} = 0 \tag{57}$$

Eq. (57) is obtained by direct substitution of Eqs. (56) into Eqs. (54). Eq. 57 is an seventh order polynomial in λ with complex valued coefficients. After considerable effort no analytic solutions to this equation were found and it was concluded that the equation would have to be solved numerically. Assuming these roots are known the analysis proceeds as follows.

The first step in completing the solution is to put Eqs. (54) into standard first order form. This is accomplished by differentiating Eq. (54a)

and obtaining simultaneous solutions for V_2'', u_0'' and u_1''' from the resulting three equations. This results in the following system of equations.

$$V_2'' = l_{11} V_2 + l_{12} V_2' + l_{13} u_0 + l_{14} u_0' + l_{15} u_0'' + l_{16} u_1 + l_{17} u_1' + l_{18} u_1'' \tag{58a}$$

$$u_0''' = l_{21} V_2 + l_{22} V_2' + l_{23} u_0 + l_{24} u_0' + l_{25} u_0'' + l_{26} u_1 + l_{27} u_1' + l_{28} u_1'' \tag{58b}$$

$$u_1''' = l_{31} V_2 + l_{32} V_2' + l_{33} u_0 + l_{34} u_0' + l_{35} u_0'' + l_{36} u_1 + l_{37} u_1' + l_{38} u_1'' \tag{58c}$$

The l_{ij}'s have been determined but they will not be given at the present time because they would overly complicate this presentation. The conversion of Eqs. (54) to standard form is completed by renaming the dependent variables as follows

$$\begin{aligned} V_2 &= y_1 \\ V_2' &= y_2 \\ u_0 &= y_3 \\ u_0' &= y_4 \\ u_0'' &= y_5 \\ u_1 &= y_6 \\ u_1' &= y_7 \\ u_1'' &= y_8 \end{aligned}$$

At this time we introduce matrix notation. Let y denote the column matrix $[\, y_i \,]$. Then Eqs. (58) plus the definition of the y_i lead to the following system of equations

$$y' = A y \tag{59}$$

where $y' \equiv [\, y_i' \,]$ and A is an eight by eight square matrix given by

$$A = \begin{bmatrix} 0 & 1 & 0 & 0 & 0 & 0 & 0 & 0 \\ \ell_{11} & \ell_{12} & \ell_{13} & \ell_{14} & \ell_{15} & \ell_{16} & \ell_{17} & \ell_{18} \\ 0 & 0 & 0 & 1 & 0 & 0 & 0 & 0 \\ 0 & 0 & 0 & 0 & 1 & 0 & 0 & 0 \\ \ell_{21} & \ell_{22} & \ell_{23} & \ell_{24} & \ell_{25} & \ell_{26} & \ell_{27} & \ell_{28} \\ 0 & 0 & 0 & 0 & 0 & 0 & 1 & 0 \\ 0 & 0 & 0 & 0 & 0 & 0 & 0 & 1 \\ \ell_{31} & \ell_{32} & \ell_{33} & \ell_{34} & \ell_{35} & \ell_{36} & \ell_{37} & \ell_{38} \end{bmatrix} \tag{60}$$

The planned method for determination of y is to assume that y is of the form

$$y = [y^*_D]\, q \tag{61}$$

where $[\, y^*_D \,]$ is a diagonal matrix with the asymptotic solutions for the y_i along the diagonal and q is a column matrix. Under these assumptions, Eq. (59) becomes

$$q' = [B]\, q \tag{62}$$

where

$$[B] = [y^*_D]^{-1} \left\{ [A]\,[y^*_D] - [y^{*\prime}_D] \right\} \tag{63}$$

Now the power series approximation methods given in Ref. 10 may be applied to Eq. (62) to solve for q. The assumed form of the solution for y is essentially the asymptotic solution for large z times a series expansion in powers of z. The rationale for choosing this representation was that the asymptotic solution should dominate the behavior for large z and the series solution should give accurate results for small z such that the composite solution should give reasonably accurate results near the points $z = 0$ and $z \to \infty$ where the boundary conditions are to be imposed.

The planned method of solution became unduly complicated when we were unable to analytically determine the values of λ that satisfied Eq. (57). Numerical solution of this equation was judged not to be a promising approach

for the following reasons. The coefficients of the powers of λ appearing in Eq. (57) are functions of $C = C_R + jC_I$, the complex damping factor of the assumed disturbance form, which is unknown at this stage of the analysis. Therefore Eq. (57) would have to be solved in conjunction with the matching conditions between upstream and downstream perturbation quantities. These matching conditions would be of the same nature as those used in the two-dimensional problem. They would be applied on a radially integrated basis across the annulus as was done for the steady-flow problem in Ref. 1 and integral moments of the three fundamental matching conditions would be used to generate a sufficient number of equations to make the problem determinate. However, since we don't know, apriori, how many of the $\lambda's$ which satisfy Eq. (57) have negative or zero values for their real parts it is not certain how many matching conditions are required. This type of uncertainty in the formulation can be handled but would require an extensive effort to computerize the method of solution. At this point it was decided that the amount of required numerical effort would subvert any physical interpretation of the results and the stability analysis was discontinued. It appears that the stability of the three-dimensional problem would be best studied from the response viewpoint.

D. CONCLUDING REMARKS ON THEORETICAL INVESTIGATIONS

During this program, the two-dimensional stability theory for wholly subsonic compressible flows was modified through the revision of the energy matching conditions. Also the formulation of the theory to supersonic flow has been initiated. A stability theory for three dimensional flow was developed but not implemented because of extensive computational requirements. It appears that the stability of three-dimensional flows would be best studied through analysis of the response of the blade row rather than a stability theory approach.

SECTION III

EXPERIMENTAL ROTATING STALL RESEARCH

A. INTRODUCTION

As a part of the work under a previous program Contract AF 33(615)-3357, an annular cascade facility was designed and fabricated. Its principal purpose is to provide detailed fundamental experimental data during and prior to the occurrence of rotating stall in order to improve our understanding of the phenomena and for use as a guide in improving the theoretical analysis. The facility has also been used to evaluate the operation of a prototype rotating stall control system (Reference 12) and to provide acoustic data for comparison with theory (References 13 and 14). This section presents the results of fundamental experiments on rotating stall.

In previous programs using the annular cascade facility (References 1 and 2), rotating stall has been induced on a variety of stator rows with differing geometries, and on a rotor row with and without circumferential inlet distortion. In addition, a limited examination of the effects of rotor-stator interference on the inception of rotating stall was included in Reference 1. The latter study showed that the effect of close coupling between the rotor and stator in a stage can lead to significant delay in rotating stall inception over that which occurs on an isolated rotor. Moreover, the delay in rotating stall inception increased as the stator stagger angle was increased, that is as the stator row was unloaded. A preliminary correlation was made between these experimental results and the predictions from a two-dimensional rotating stall stability theory for a stage. The theoretical results also showed a delay in inception, but the numerical predictions of the theory were generally inaccurate due to a lack of steady-state performance data for the rotor and stator rows in the stage. The theory requires these steady-state data as inputs.

The major portion of the current experimental study was designed to provide basic information on rotor-stator interference and to provide the steady-state performance data required by the rotating stall stability theory. In addition, a limited study was performed to determine the effect of circumferential inlet distortion on rotating stall inception in the closely coupled stage. The results of these studies have been used for comparison with the predictions of the rotating stall stability theory for multiple blade rows. Moreover, the experiments have provided some unexpected results which are important in their own right.

All of the above rotating stall investigations were performed in a configuration of the annular cascade with high hub-to-tip ratio (0.80). This hub-to-tip ratio was chosen originally because the data would be used to guide and verify the development of a rotating stall theory that was basically two-dimensional. However, rotating stall frequently originates on the front stages of axial flow compressors where the hub-to-tip ratio is usually quite low and three-dimensional effects may be important. Thus, during the latter portion of the current program, a major modification was made to the annular cascade facility to provide it with a low hub-to-tip ratio (0.44) configuration. The final tests in the current program consisted of checkout of the new configuration and determination of the rotating stall inception boundary on a low hub-to-tip ratio rotor.

The order of presentation of the experimental program in the remainder of this section is as follows. A description of the high hub-to-tip ratio configuration of the annular cascade facility is presented in Section III-B. Section III-C presents the results of the study of rotor-stator interference effects with and without circumferential inlet distortion. Section III-D presents a description of the low hub-to-tip ratio configuration of the annular cascade and the preliminary rotating stall inception tests on an isolated rotor. Finally, in Section III-E, a summary of the experimental program is presented.

B. DESCRIPTION OF ANNULAR CASCADE FACILITY WITH HIGH HUB-TO-TIP RATIO

1. General Description

The annular cascade facility consists of a test section built around the outer front casing of a J-79 jet-engine compressor with a Calspan fabricated hub. The facility includes a bell-mouth inlet on the outer casing and a bullet nose on the hub to provide a smooth flow of air to the test section. Outlet ducting is connected to an independently variable source of suction to provide the required flow through the annulus. An electrically powered two-speed axial flow fan is used as the source of suction. Continuous control of the mass flow is achieved through the use of variable inlet guide vanes to the fan and a variable damper in the fan exit flow. Photographs of the complete annular cascade facility and of the test-section portion of the facility are shown in Figures 2 and 3, respectively.

The test section of the annular cascade forms a circular annulus with an outer diameter of 29.35 inches and an inner diameter of 23.35 inches which provides a hub-to-tip ratio of 0.80. The outer casing will accept up to six variable stagger angle stator rows. The hub has provision for two rotor rows at the third- and fifth-stage rotor locations of the J-79 compressor. Speed control on each rotor hub is independently variable in either direction of rotation. The overall combination of variable stagger angle stators, independently powered rotors, and independent mass flow control provides exceptional versatility to the complete test rig.

The configuration of the annular cascade used for rotor-stator interference studies is sketched in Figure 4. The sketch shows both the third and the fifth stage rotors. However, only the fifth stage rotor was rotated during the test program. The third stage rotor and the outer skins on the hub upstream and downstream of the rotors, and between the rotors were held stationary. The fifth stage rotor is driven by a hydraulic motor mounted inside the hub. An external hydraulic pump system, powered by a

50-horsepower electric motor, is used to provide power to the hydraulic motor. With this system, the fifth stage rotor speed is continiously variable between zero and approximately 1760 rpm. This rotor hub is designed to accept 46 blades. The method of fastening the blades to the hub allows individual adjustment of the stagger angle. In addition to the rotor blades on the fifth stage hub, a symmetric two-lobe distortion screen was mounted on the stationary third stage rotor hub for some of the tests. The location of the distortion screen is indicated in Figure 4.

2. Rotor and Stator Blading and Distortion Screen

The tests performed during this program involved either an isolated rotor or a closely coupled rotor-stator stage. The fifth stage rotor and stator blades from a J-79 compressor were used in these tests, unmodified except for blade length, which was shortened in order to fit into the three-inch annulus of the test rig. In each case, the spanwise portion of the blades closest to the outer compressor casing was used. The set of rotor blades has been designated as Rotor Set No. 1 and the set of stator blades as Stator Set No. 1, in keeping with the nomenclature used in References 1 and 2. The geometric characteristics of these blades have been presented in References 1 and 2, along with detailed measurements of turning and loss performance when used as single blade rows in isolation. The extensive performance data are not repeated here, except where they are used for purposes of comparison with the current test results. The blade geometric characteristics are repeated below.

Rotor Set No. 1 has the same number of blades and is at the same axial location as the fifth stage rotor in the original J-79 compressor. These blades have a NACA 65-Series thickness distribution on a circular arc mean line.

The geometric characteristics are listed in TABLE 1.

TABLE 1

Geometric Characteristics of Rotor Set No. 1

Blade Length		2.98 inches
Blade Chord		1.448 inches (constant)
Blade Thickness;	Outer Diameter	0.072 inch
	Mid-Annulus	0.086 inch
	Inner Diameter	0.113 inch
Blade Camber Angle (angle between tangents to mean camber line of leading and trailing edges);	Outer Diameter	23.5 degrees
	Mid-Annulus	28.0 degrees
	Inner Diameter	32.7 degrees
Blade Twist		See Text
Number of Blades		46
Solidity at Mid-Annulus		0.805

The blades in Rotor Set No. 1, have a nominal twist of 14.5 degrees over the three inch span. However, measurements showed that in practice, the twist over the center 2-1/2 inches in these production J-79 blades varied between 10.8 and 14.4 degrees, with an average value of 12.9 degrees. The blades were installed in a sequence which distributed the nonuniformities in twist over the complete circumference.

A blade-tip clearance problem was encountered on installation of the rotor assembly in the annular cascade. The J-79 compressor outer casing used in the annular cascade is about one-tenth inch out of round with the split line diameter being the largest. In the final assembly, the rotor was mounted in the casing with shims along the split line which provided the following tip clearances: 0.030 inch on the top and bottom, and 0.046 to 0.048 inch on the sides. Since the stagger angles of the rotor blades are adjustable, the quoted tip clearances apply only to the mid-chord pivot points. Clearance at the blade leading and trailing edges vary slightly with changes in stagger angle from the angle for which the tip contour was determined. The stagger angle used to determine the tip contour was the maximum which was expected to be used. The choice of lower reference stagger angles would have resulted in interference between the blades and outer casing at stagger angles much larger than the reference.

Stator Set No. 1, has the same number of blades and is located at the same axial location as the fifth stage stator row in the original J-79 compressor. Its geometric characteristics are listed in Table 2, and the axial location is shown in Figure 4.

For some of the tests, a circumferential distortion screen was mounted on the third stage rotor hub, upstream of the rotor-stator stage. The screen has a symmetric two-lobed pattern with each lobe encompassing a circumferential extent of 60 degrees. The lobes of the screen are perforated steel plates. Detailed calibration of the distortion generated by the screen has been presented in Reference 1. Briefly, the total pressure deficit in

TABLE 2

Geometric Characteristics of Stator Set No. 1

Blade Length		2.98 inches
Blade Chord;	Outer Diameter	1.316 inches
	Inner Diameter	1.290 inches
Blade Thickness;	Outer Diameter	0.1524 inch
	Inner Diameter	0.1132 inch
Blade Camber Angle (angle between tangents to mean camber line of leading and trailing edges)		35.6 degrees
	Outer Diameter	0 degree
Blade Twist;	Mid-Annulus	0.28 degree
positive twist reduces stagger	Inner Diameter	1.42 degree
Number of Blades		54
Solidity at Mid-Annulus		0.85

the wake of each lobe was approximately constant over a 60 degree circumferential extent. The magnitude of the total pressure drop in the screen wake was approximately 1.1 times the dynamic pressure measured far upstream of the screen.

3. Instrumentation

The outer casing of the annular cascade test section has been modified to allow circumferential and radial traverses with hot-wire and total pressure probes upstream and downstream of the fifth stage location. These traverse locations are shown in Figure 3. Two probes can be accommodated simultaneously in either of these traverse mounts with adjustable circumferential spacing between the two probes. In addition, simple radial traverses can be made at various other locations in the test section. The measuring locations used in this program are indicated in Figure 4, as Stations 0, 1, and 2.

In all of the experiments, mass flow through the test section was determined by measuring the dynamic pressure in the constant-area annulus upstream of the test section (Station 0 in Figure 4).

Total pressure surveys were made through traverses with a seven-tube total pressure rake which spanned one-half of the three-inch annulus. A complete radial survey was obtained by positioning the rake at two radial locations, one adjacent to the hub and one adjacent to the outer casing. At each radial location, the total pressure rake was aligned with the flow by using a Conrad arrowhead style yawmeter incorporated at the mid-span location of the rake. At axial Station 1 in Figure 4, a single radial survey was made midway between adjacent stator blades to determine the time averaged total pressure rise across the rotor. At Station 2, downstream of the stators, circumferential as well as radial surveys were performed to insure that the stationary stator blade wakes were properly taken into account. In all tests, the pressures detected by the rake were photograph-

ically recorded from a multitube inclined monometer.

Radial surveys of the temperature rise across the rotor in the rotor-stator stage were made with a matched set of two thermister probes calibrated to measure total temperature differences as small as 0.01 degrees Fahrenheit, in an environment with constant upstream reference temperature. For these tests, one thermister probe was located at mid-annulus upstream of the rotor to provide an upstream reference total temperature. The second probe was used to perform radial surveys at Station 1, between the rotor and stator, to determine the radial distribution of total temperature rise across the rotor. Output from the matched thermister probes was integrated for 50 seconds on an integrating voltmeter and the average of seven such integrated readings were used to determine a single data point. Thus, each data point represented a time average for 350 seconds. The very long averaging times were used in an attempt to compensate for random fluctuations in upstream reference temperature in the annular cascade. The annular cascade uses room air as its source and the inlet temperature is not constant in time.

In addition to the total pressure and total temperature data measured during the current program, velocity and swirl angle measurements presented in References 1 and 2, will be used to complement the data analysis in the presentation of the results. These data were taken at Station 2 (Figure 4) with a linearized, two-channel, constant-temperature, hot-wire anemometer system in conjunction with a crossed-wire probe. Readout for the hot-wire system was made by means of a two-channel integrator-digital voltmeter system. Each linearized hot-wire signal was integrated for 60 seconds and the time average was calculated from the readings on the digital voltmeters.

Rotating stall was detected and the number of cells and propagation velocity were measured by using outer-wall static pressure taps connected to pressure transducers. Two pressure taps at different circumferential

locations and at an axial location corresponding to the quarter-chord on the rotor blades were used.

C. EXPERIMENTS ON A CLOSELY COUPLED ROTOR-STATOR STAGE

In Reference 1, a limited study was performed to study the effect of rotor-stator interference on the inception of rotating stall. These experiments were conducted in the configuration of the annular cascade shown in Figure 4. The experiments were designed to investigate whether interference between a rotor and a stator has an effect on the conditions for inception of rotating stall. The rotor row and the stator row used in these experiments had previously been tested in isolation so that the conditions under which the individual blade rows undergo inception were known. The inlet flow conditions relative to each blade row were such that, in the absence of interference, rotating stall would occur first on the rotor. These studies were performed at a fixed setting of the rotor blade stagger angle, but with four different settings of the stator blade stagger angle. The combined results showed an increasingly larger delay in rotating stall inception in comparison to the isolated rotor as the stator stagger angle was increased, that is as the stator row was unloaded. Thus, it was concluded that rotor-stator interference does have an effect on rotating stall inception and that the magnitude of the effect depends on the loading of the blade row which would be unstalled in the absence of interference.

An attempt was made to correlate the experimental inception points on the stage with the predictions of the two-blade row rotating stall stability theory. The results of the correlations were encouraging in that the theory predicted that blade row coupling does stabilize the stage. However, the numerical predictions were inaccurate, due to a lack of steady state performance data for the blade rows. The theory requires these steady state performance data as inputs. The major portion of the current experimental program was designed to extend the experimental data so that valid comparisons could be made between theory and experiment.

The steady-state blade row performance data required as inputs to the rotating stall stability theory are as follows: The relative losses through the rotor row, the turning angle of the flow through the rotor, the losses through the stator row, and the turning angle of the flow through the stator row. Each of these quantities will be addressed in turn in the following discussion. A sketch showing the velocity notation is presented in Figure 5.

1. Relative Losses Through the Rotor

The basic experimental data required as an input to the rotating stall theory are the steady-state losses across the compressor blade rows. These are required in a coordinate system fixed to the blade row (relative losses). The determination of the relative losses through a rotor row requires the measurement of total pressure rise in a duct-fixed coordinate system and a measurement of the work done by the rotor. In previous tests on an isolated rotor, the work done by the rotor was determined from the velocity components measured downstream of the rotor with a crossed hot-wire anemometer system. However, in the current program, the tests were performed on a closely coupled rotor-stator stage and the measurement of the components of velocity between the rotor and stator was not possible. Thus, an attempt was made to determine the rotor work by measuring the total temperature rise across the rotor instead of the velocity components. It will be demonstrated that the rotor work coefficients calculated from the total temperature measurements between the rotor and stator are reasonably consistent in the mid-annulus region with the work coefficients calculated from velocity measurements downstream of the isolated rotor. However, the total temperature results are not accurate enough to provide an estimate of the work done by the rotor for use in calculating the relative losses across the rotor in a rotor-stator stage. On the other hand, application of the rotating stall stability theory still requires the relative losses as an input. In view of the disappointing temperature results, the rotor work determined from the isolated rotor tests will be used in combination with the total pressure rise

across the rotor in the rotor-stator stage to estimate the relative rotor loss coefficient. The experimental results and the method of data analysis are described below. The total pressure measurements are presented first.

Total pressure surveys between the rotor and stator (Station 1 in Figure 4) were performed for a rotor stagger angle, δ_{RM}, of 40 degrees measured at mid-annulus and for three different stator stagger angles, δ_{SM} = 28.2, 37.2 and 47.2 degrees, again measured at mid-annulus. The mean axial velocity, U_o , measured far upstream of the stage was held constant at 60 ft/sec in these tests and measurements were made for a wide range of rotor speeds. With the two smaller stator stagger angles, rotating stall inception was sudden and of large amplitude. In these cases, rotating stall displayed hysteretic behavior at inception. That is, as rotor rpm was increased rotating stall occurred at a higher value of rpm than the value at which it disappeared on decreasing the rotor rpm. The stage with δ_{SM} = 47.2 degrees did not display hysteresis in rotating stall inception. In this case, as rotor speed was increased, the outer casing pressure transducers used to detect rotating stall indicated increasing turbulence which became quite large just before inception. The rotating stall which occurred was intermittent in time and not much larger in amplitude than the turbulent pressure fluctuations. Repeated surveys of total pressure for this stagger angle showed that the data were not repeatable near inception. Moreover, the total pressure rise across the rotor began to decrease with increasing rotor speed well before inception occurred. These results suggest that steady stall was occurring on the rotor well before rotating stall inception for a stator stagger angle of 47.2 degrees. The presence of steady stall and non-repeatable total pressures made it impractical to continue tests with this atypically large stator stagger angle. Thus, the remainder of the tests were completed only for stator stagger angles of 28.2 and 37.2 degrees.

Radial distributions of total pressure coefficient between the rotor and stator are shown in Figures 6(a) and 6(b), for stator stagger angles of 28.2 and 37.2 degrees, respectively. The data obtained in the absence of rotating stall are shown as open symbols connected by solid lines. Data measured while rotating stall was occurring are shown as variously dashed lines without symbols. The total pressure coefficient $\Delta\bar{C}_{P_{T_1}}$, shown in Figure 6, is defined as

$$\Delta\bar{C}_{P_{T_1}}(r) = \frac{\bar{P}_{T_1} - \bar{P}_{T_0}}{\frac{\rho}{2} U_0^2} \tag{64}$$

where P_{T_0} = Total pressure far upstream of the stage (Station 0 in Figure 4).

P_{T_1} = Total pressure in the survey plane between the rotor and stator (Station 1 in Figure 4).

r = Radius

U_0 = Mean axial velocity far upstream (Station 0).

ρ = Air density

and $\bar{(\ )}$ indicates a time average in a fixed frame of reference downstream of the rotating blades (this is assumed to be equivalent to a circumferential average in a frame of reference which rotates with the blades).

Some of the radial surveys were repeated twice for δ_{SM} = 28.2 degrees (Figure 6(a)). In these cases, both sets of data are plotted. There is relatively good agreement between these repeated data, in contrast to the poor repeatability mentioned previously for δ_{SM} = 47.2 degrees. Note that when rotating stall begins, there is a drop in pressure coefficient across the complete annulus and that the stalled pressure coefficients are nearly independent of rotor rpm over the range tested.

The radial pressure distributions shown in Figure 6 were integrated

radially (area-averaged) to provide an overall total pressure rise coefficient, $\Delta \bar{\bar{C}}_{p_{T_1}}$, across the rotor. The results are shown in Figure 7, along with additional data measured on the same rotor in isolation, that is with the stator row removed. The overall total pressure rise coefficient is defined as follows:

$$\Delta \bar{\bar{C}}_{p_{T_1}} = \frac{2}{(r_t^2 - r_h^2)} \int_{r_h}^{r_t} r \, \Delta \bar{C}_{p_{T_1}}(r) \, dr \tag{65}$$

where r_h = inner wall (hub) radius of annular cascade

r_t = outer wall (tip) radius of annular cascade

and $\Delta \bar{C}_{p_{T_1}}(r)$ is defined in Equation (64).

Inception of rotating stall with increasing rotor speed is indicated in Figure 7 by a vertical arrow. Note that the stage stalls at increasingly higher values of rotor speed as the stator stagger angle is increased. Also, the behavior of the total pressure rise after stall is somewhat different on the isolated rotor than on the stage. On the isolated rotor the total pressure rise after stall increases fairly rapidly with increasing rotor rpm, while on the stage the total pressure increases only slightly with increasing rotor rpm.

The pre-stall total pressure rise across the isolated rotor is significantly lower than the total pressure rise across the rotor in the stage. At the time these data were first analyzed, it was speculated that some of the difference may be due to differences in axial location of the total pressure surveys downstream of the rotor. The isolated rotor data shown in Figure 7, were measured prior to the current program (Reference 2). In that study, the total pressure surveys were made approximately 3.9 inches (2.73 rotor chords) downstream of the rotor-blade trailing edges. In the current study on the rotor-stator stage, the corresponding measurements were

made near the stator-vane leading edges, at an axial distance of 0.70 inches (0.48 rotor chords) from the rotor-blade trailing edges. The larger rotor-to-probe distance on the isolated rotor may have contributed additional losses in total pressure from mixing and from friction on the annulus walls. However, the differences between the isolated rotor and the rotor-stator stage appeared to be too large to be accounted for solely by mixing and additional wall friction. Thus, the total pressure surveys on the isolated rotor were repeated with the total pressure rake situated in its original downstream location (3.9 inches from the rotor trailing edge) and also with the rake situated at the same location as used on the stage (0.7 inches from the rotor trailing edge). The downstream rake location served as a check of the original isolated rotor data presented in Figure 7.

The results from the new total pressure surveys with the downstream rake location are compared to the original (Reference 2) surveys in Figure 8. At rotor speeds up to 850 rpm, the data agree quite well. At speeds between 900 and 1000 rpm, the current data show a small increase near the hub and very small decreases in the outer half of the annulus. Area-weighted averages of the new profiles provide almost identical values of $\Delta \overline{\overline{C}}_{P_T}$, as those found from the Reference 2 data, even for the 900, 950 and 1000 rpm cases. Thus, except for a slight radial redistribution of the profiles, the current data agrees quite well with the original data. The radial redistribution may have been caused by small geometric differences in the hub of the annular cascade, which was rebuilt between the two sets of surveys.

Radial distributions of total pressure coefficient measured during the current program with the rake close to, and far from, the isolated rotor are compared in Figure 9. Here, the data measured close to the rotor are consistently a small amount larger than the data measured far from the rotor. This trend extends over most of the annulus and occurs at low, as well as high rotor rpms. However, the apparent increase in total pressure close to the isolated rotor is only a fraction of the increase in total pressure across

the same rotor in a rotor-stator stage. This is illustrated in Figure 10, where the radial distributions of total pressure coefficients for the rotor in the stage prior to rotating stall inception are compared to similar data for the isolated rotor. In this figure, all of the data were measured at the same axial location 0.7 inches from the rotor trailing edge. The total pressure coefficients for the rotor in the stage are larger than those for the isolated rotor and the differences increase with rotor speed up to 1000 rpm. At 1100 rpm, only the stage with δ_{SM} = 37.2 degrees remained unstalled, so a comparison is not possible for this speed.

All of the total pressure data presented thus far are summarized in Figure 11, where area-averaged total pressure rise coefficients based on relative inflow velocity to the rotor are shown as a function of flow coefficient. The notation in this figure is as follows:

Pressure Coefficient, $$\Delta\bar{\bar{C}}_{P_{T_{q_1}}} = \frac{\overline{(\bar{P}_{T_1} - \bar{P}_{T_0})}}{q_1} = \frac{\overline{(\bar{P}_{T_1} - \bar{P}_{T_0})}}{q_0\left[1 + \left(\frac{\bar{\bar{W}}_b}{U_0}\right)^2\right]} \qquad (66)$$

Work Coefficient, $$\bar{\bar{C}}_{W_{q_1}} = \frac{2\,\overline{W_b W_1}}{U_0^2\left[1 + \left(\frac{\bar{\bar{W}}_b}{U_0}\right)^2\right]} \qquad (67)$$

Flow Coefficient, $$\varphi = \frac{U_0}{\bar{\bar{W}}_b}$$

where:

q_0 = Dynamic pressure corresponding to a mean axial velocity, $\left(\frac{\rho}{2} U_0^2\right)$

q_1 = Dynamic pressure corresponding to mean velocity relative to the rotor, $\frac{\rho}{2}\left(U_0^2 + \bar{\bar{W}}_b^2\right)$

$\bar{P}_{T_0}$ = Time-averaged total pressure at mid-annulus upstream of rotor (Measured in absolute coordinate system)

$\bar{P}_{T_1}$ = Time-averaged total pressure at given radius downstream of rotor (Measured in absolute coordinate system)

$\overline{(\bar{P}_{T_1} - \bar{P}_{T_0})}$ = Area weighted average of total pressure rise across rotor

U_0 = Mean axial velocity at mid-annulus far upstream of rotor

W_1 = Circumferential flow velocity (Measured in absolute coordinate system downstream of isolated rotor)

$\bar{W}_1$ = Time average of W_1

$\bar{W}_b$ = Rotor Velocity (Constant in time)

$\overline{\bar{W}_b}$ = Area weighted average of rotor velocity

$\overline{\bar{W}_b \bar{W}_1}$ = Area weighted average of $\bar{W}_b \bar{W}_1$

The area weighted averages were computed by numerically integrating the various quantities over the span of the annular cascade in the same fashion as indicated by Equation 65.

As can be seen in Figure 11, the current and original (Reference 2) data measured with the total pressure rake 3.9 inches downstream of the isolated rotor agree very well. The current data measured with the rake 0.7 inches from the isolated rotor fall a small, almost constant, amount above the downstream measurements. The difference in this case may well be due to increased friction and mixing losses. However, there is a significant increase in total pressure rise across the rotor when the stator row is added immediately downstream of the rotor. This is true, even when the total pressure rake is situated in the same location for measurements on the isolated rotor as it is for measurements on the stage. Thus, the presence of the stator row appears to have a beneficial upstream influence on the

performance of the rotor. It is not known whether the presence of the stators increases the work done by the rotor or decreases the losses through the rotor. A work coefficient calculated from hot-wire measurements downstream of the isolated rotor is shown in Figure 11, for comparison. If this work coefficient applies to the staged rotor as well as the isolated rotor, then the differences between this curve and the total pressure rise data give the relative loss coefficient across the rotor. As noted at the beginning of this section, one of the inputs required by the rotating stall stability theory is the relative loss coefficient across the rotor. Thus, an attempt was made to determine the actual work coefficient of the rotor in the stage by measuring the total temperature rise across the rotor. The results are described below.

The relative loss coefficient, $(-\Delta \bar{C}_{p_{T_R}})$, across the rotor is given by the difference between the work done by the rotor and the total pressure rise generated by the rotor. For incompressible flow, this is

$$(-\Delta \bar{C}_{p_{T_R}}) = \frac{2 C_p \Delta \bar{T}_{T_1}}{U_o^2} - \Delta \bar{C}_{p_{T_1}} \tag{68}$$

where C_p = specific heat at constant pressure ($C_p = 6006\ ft^2/sec^2 {}^\circ R$ for air)

$\Delta \bar{C}_{p_{T_1}}$ = time averaged total pressure rise coefficient across rotor

$(\bar{P}_{T_1} - \bar{P}_{T_o}) / \frac{\rho}{2} U_o^2$ in absolute coordinate system

$\bar{P}_T$ = time averaged total pressure (pounds/ft^2) in absolute coordinate system

$\Delta \bar{T}_{T_1}$ = time averaged total temperature rise ($\bar{T}_{T_1} - \bar{T}_{T_o}$) across rotor in absolute coordinate system

$\bar{T}_T$ = time averaged total temperature (deg. Rankine) in absolute coordinate system.

U_o = mean axial velocity (ft/sec) far ahead of rotor

ρ = density of air (slugs/ft^3).

and subscripts

0 - denotes conditions far upstream of rotor

1 - denotes conditions downstream of rotor, but ahead of stator vanes

R - denotes conditions in coordinate system fixed to rotor, (relative coordinate system).

The relative loss coefficient can also be expressed in terms of the swirl velocity downstream of a rotor. In this case

$$(-\Delta\bar{C}_{P_{T_R}}) = \frac{2\bar{W}_b(\bar{W}_1 - \bar{W}_o)}{U_o^2} - \Delta\bar{C}_{P_{T_1}} \qquad (69)$$

In these tests, $\bar{W}_o = 0$ so that

$$(-\Delta\bar{C}_{P_{T_R}}) = \frac{2\bar{W}_b\bar{W}_1}{U_o^2} - \Delta\bar{C}_{P_{T_1}} \qquad (70)$$

The total temperature rise, $\Delta\bar{T}_{T_1}$, measurements were made with a matched set of two thermister probes as described in Part A. 3 of this section. Radial distributions of the rotor work coefficient $\frac{2C_p\Delta\bar{T}_{T_1}}{U_o^2}$ calculated from some of the total temperature rise surveys are compared in Figure 12, to the total pressure rise coefficient, $\Delta\bar{C}_{P_{T_1}}$, and to the rotor work coefficient, $\frac{2\bar{W}_b\bar{W}_1}{U_o^2}$, measured with the stator row removed. The data in Figure 12(a) are for a stator stagger angle of 28.2 degrees. Results from temperature surveys performed on two different dates are shown for two rotor speeds. As can be seen, there is considerable scatter in the temperature survey results repeated on different dates. Moreover, at the lower rotor speed, (700 RPM) the rotor work coefficient is smaller than the total pressure rise coefficient over most of the annulus. This would indicate a negative relative loss coefficient, which is not possible. Results are shown for a stator stagger angle of 37.2 degrees in Figure 12 (b). In this case, the temperature measurements were not repeated on different dates. However, the trends in the data are similar.

The very large rise in the apparent work coefficient near the hub, $\Delta r = 0$, is believed to be a result of heat added to the flow by the hydraulic motor used to drive the rotor. The latter is situated inside the hub and becomes hotter as the test progresses. The addition of external heat from the motor would explain a peculiarity of the temperature surveys noted during the tests. It was noted that measurements near the hub showed a substantially smaller temperature rise at the beginning of a test than a similar measurement made near the end of the test. On the other hand, repeated temperature tests at mid-annulus did not exhibit this consistent behavior. Moreover, temperature surveys at very low rotor and flow speeds also showed a temperature rise near the hub when it should not have been possible to detect such a rise. Thus, it was concluded that the temperature rise data measured near the hub were contaminated by the addition of external heat.

In summary, the above comments indicate that the total temperature results are not accurate enough to provide an estimate of the relative losses across the rotor in a rotor-stator stage. On the other hand, application of the rotating stall stability theory still requires the relative losses as an input. In view of the disappointing temperature results, the rotor work coefficient, $\frac{2\bar{W}_b\bar{W}_1}{U_o^2}$, determined from the isolated rotor tests was used in combination with the total pressure rise across the rotor in the rotor-stator stage to estimate the relative rotor loss coefficient, (see Equation 70). The radial distributions of this work coefficient are shown in Figures 12(a) and 12(b), along with the measured total pressure rise across the staged rotor, and the work coefficient calculated from the temperature measurements. It is worth noting that even though the temperature-derived work coefficients are not very accurate, they do appear to be reasonably consistent in the mid-annulus region with the velocity-derived isolated rotor work coefficients.

The data in Figure 12 show that at low rotor speeds, the isolated rotor work coefficient is nearly identical to the total pressure coefficient

in the middle portion of the annulus. The fact that the isolated rotor work coefficient is very slightly smaller than the total pressure rise in the mid-annulus region should not be taken as an indication of negative relative losses. There are two reasons for this statement. First, the hot-wire velocity measurements are accurate to within approximately 3 percent of the true value and some of the apparent (small) negative relative losses could be due to the accuracy of the hot-wire measurements. Second, the hot-wire velocity measurements on the isolated rotor were made farther downstream than the total pressure measurements on the staged rotor. Thus, radial re-distribution of the flow could account for the apparent negative local relative loss coefficients. In general, comparisons of the complete set of measurements for all rotor speeds on the isolated and staged rotor are encouraging in that the trends shown are what one would expect. Even the isolated rotor work coefficient after rotating stall inception appears to be consistent with the data obtained prior to stall inception. This is illustrated in Figure 13, where radial distributions of work coefficient are shown for the isolated rotor at various rotor speeds, both unstalled and stalled.

As can be seen, the isolated rotor work coefficients with and without rotating stall appear to be consistent with each other, except for two unstalled data points at 1000 rpm on the rotor. For this rotor speed, radial distributions of the isolated rotor work coefficient are nearly identical over the annulus in the range $0 \leq \Delta r \leq 2.2$ inches. The difference in work coefficients for the stalled and unstalled rotor at 1000 rpm occurs near the tip where the unstalled rotor work coefficient decreased significantly; a result which appears inconsistent with the remainder of the unstalled data. At the same time, the stalled rotor work coefcients at 1000 rpm appear consistent with the unstalled data at lower rotor speeds and, also consistent with the stalled data at higher rotor speeds. The reason for the inconsistent behavior of the unstalled isolated rotor at 1000 rpm is not known. However, the main point to be made here is that the isolated rotor

work coefficients, with the exception of the unstalled data near the tip at 1000 rpm, are well-behaved through and beyond the stall boundary. Moreover, since they agree reasonably well with the work obtained from the total temperature measurements taken on the rotor-stator stage in the mid-annulus region, the isolated rotor work coefficients were assumed to hold for the rotor-stator stage. Thus, the solid line in Figure 11 was used as an estimate of the area-weighted average of the rotor work coefficient for the rotor-stator stage. The work coefficient in this figure was derived from the unstalled measurements in Figure 13 for rotor rpm's $\leq 950 (\phi \geq 0.517)$ and from stalled measurements for rotor rpm's $> 950 (\phi < 0.517)$.

The area-weighted average of the rotor loss coefficient was calculated from the data shown in Figure 11 as follows.

$$(-\Delta \overline{\overline{C_{P_{T_R}}}}) = \left(\frac{2 \overline{\overline{W_b W_1}}}{U_o^2} \right)_{\substack{\text{ISOLATED} \\ \text{ROTOR}}} - \Delta \overline{\overline{C_{P_{T_1}}}}_{\substack{\text{STAGED} \\ \text{ROTOR}}} \tag{71}$$

The results are shown in Figure 14 for the isolated rotor and for the rotor in the rotor-stator stage with two different stator stagger angles. The data for the rotor-stator stage at 1000 rpm and above, are based on the isolated rotor work coefficients measured in the presence of rotating stall. In all cases, the rotor pressure rise coefficients, $\Delta \overline{\overline{C_{P_{T_1}}}}$, used in the calculations were measured with rotating stall absent. Experimental inception of rotating stall is indicated in Figure 14 by a vertical arrow. The solid lines drawn through the loss data are spline-fitted to the experimental points. These spline-fitted curves were used as inputs to the two-blade-row stability theory for calculating rotating stall inception. Application of the theory to the rotor-stator stage required a small extrapolation of the loss data. The extrapolations are shown as dashed extensions to the solid lines.

The rotating stall stability theory requires several other inputs, as well as the relative losses through the rotor in the rotor-stator stage. These inputs are: the turning angle of the flow through the rotor, the losses through the stator row, and the turning angle of the flow through the stator row. The methods used to estimate these parameters from the experimental data are discussed below.

2. Turning Angle of Flow Through the Rotor

In previous tests on an isolated rotor, the turning of the flow through the rotor was obtained by measuring the velocity components downstream of the rotor with a crossed hot-wire anemometer system. As noted at the beginning of this section, it was not possible to obtain similar velocity data between the rotor and stator in the closely-coupled rotor-stator stage. Moreover, the isolated rotor turning data cannot be used directly, because the isolated rotor stalled at a lower rotor speed than the rotor in the rotor-stator stage. This leaves one with the requirement to estimate the turning through the unstalled rotor, under conditions for which the isolated rotor was in rotating stall. In the previous paragraphs, the work coefficient measured on the isolated rotor was shown to be insensitive to the presence of rotating stall, and to provide what appears to be a reasonable basis for calculating the relative losses through the rotor in a rotor-stator stage. Thus, the isolated rotor work coefficient was also used to estimate the effective turning of the flow through the rotor.

For incompressible flow, the time-averaged absolute outlet swirl, $\overline{\tan \beta_1}$, from the rotor is given by (see Figure 5),

$$\overline{\tan \beta_1} = \frac{\bar{W}_1}{\bar{U}_1}$$

and the time-averaged relative outlet swirl, $\overline{\tan \beta_{1_R}}$, is given by

$$\overline{\tan \beta_{1_R}} = \frac{\bar{W}_1 - \bar{W}_b}{\bar{U}_1}$$

Note that in the experiments, W_b was held constant in time, so $\bar{W}_b = W_b$.

Area-weighted averages of the absolute and relative swirls are given by

$$\overline{\tan\beta_1} = \left(\frac{\overline{\bar{W}_1}}{\bar{U}_1}\right)$$

and

$$\overline{\tan\beta_{1_R}} = \left(\frac{\overline{\bar{W}_1}}{\bar{U}_1}\right) - \left(\frac{\overline{\bar{W}_b}}{\bar{U}_1}\right)$$

From continuity, the area-weighted axial flow velocity, $\bar{U}_1$, is equal to the mean axial flow velocity, U_o, far upstream of the rotor. It was assumed that

$$\left(\frac{\overline{\bar{W}_b}}{\bar{U}_1}\right) = \frac{\bar{\bar{W}}_b}{U_o}$$

and

$$\left(\frac{\overline{\bar{W}_1}}{\bar{U}_1}\right) = \frac{(2\,\overline{\overline{W_b W_1}} / U_o^2)}{(2\,\bar{\bar{W}}_b / U_o)}$$

With these assumptions, one has

$$\overline{\tan\beta_1} = \frac{(2\,\overline{\overline{W_b W_1}} / U_o^2)}{(2\,\bar{\bar{W}}_b / U_o)} \qquad (72)$$

and

$$\overline{\tan\beta_{1_R}} = \frac{(2\,\overline{\overline{W_b W_1}} / U_o^2)}{(2\,\bar{\bar{W}}_b / U_o)} - \frac{\bar{\bar{W}}_b}{U_o} \qquad (73)$$

The isolated rotor work coefficient, $(2\,\overline{\overline{W_b W_1}} / U_o^2)$, has already been calculated as a function of rotor rpm. (Figure 11 presents a slightly different form of this coefficient as a function of flow coefficient.) The area average $\overline{W}_b / U_o$ is easily calculated from the annulus geometry and rotor rpm.

The results from Equations 72 and 73 are plotted in Figure 15, as a function of rotor rpm. Note that the negative of the relative swirl $(-\overline{\overline{\tan \beta_{1_R}}})$ is plotted to present both curves on the same graph. Also shown in Figure 15, are the results from direct measurements of $\overline{\overline{\tan \beta_1}}$ and $-\overline{\overline{\tan \beta_{1_R}}}$ which were reported in Reference 2. In the absence of rotating stall (rpm < 1000), the swirl calculated from the rotor work agrees very well with the direct measurements. In the stalled region (rpm > 1000), the direct measurements of swirl are less than the values calculated from the rotor work. The direct measurements display a discontinuity at stall inception, whereas the calculated values progress smoothly through stall inception. Thus, the calculated swirl values for the isolated rotor were used in the theory as an estimate of the unstalled turning performance of the rotor in the rotor-stator stage.

3. Losses Through the Stator Row

The losses through the stator row in the rotor-stator stage were obtained by combining the results from total pressure surveys downstream of the stators with the results from the total pressure surveys between the rotor and stator. The area-averaged loss coefficient through the stator row is given by

$$(-\Delta \overline{\overline{C}}_{P_{T_S}}) = \Delta \overline{\overline{C}}_{P_{T_1}} - \Delta \overline{\overline{C}}_{P_{T_2}} \qquad (74)$$

where $\Delta \overline{\overline{C}}_{P_{T_1}}$ is the area-averaged total pressure rise coefficient across the rotor, (see Figure 7) and $\Delta \overline{\overline{C}}_{P_{T_2}}$ is the area-averaged total pressure rise coefficient across the stage.

The area-averages of the total pressure rise coefficients $\Delta C_{P_{T_1}}$ and $\Delta C_{P_{T_2}}$ were obtained in a different manner for each axial location. At axial location 1, between the rotor and stators, a single radial survey was made mid-way between adjacent stator blades to determine the time-averaged total pressure rise across the rotor. These time-averaged data were then integrated radially to obtain an area average (Equation 65). At location 2, downstream of the stators, it was necessary to perform circumferential as well as radial surveys to ensure that the stationary stator blade wakes were properly taken into account. In this case, radial surveys were performed at 7 equally-spaced circumferential locations and the results were averaged circumferentially. The circumferential averages were then integrated radially to obtain the required area average. The circumferential extent of the surveys was large enough to cover two stator-blade spacings. Fourteen radial locations were used in the total pressure surveys at both axial locations. Thus, the area-averaged total pressure coefficient downstream of the stator represents an integration over 98 separate spatial locations.

The results from the total pressure surveys are summarized in Figure 16, where the area-averaged total pressure loss coefficients through the stator row (Equation 74) are shown as a function of rotor speed. The lines drawn through the experimental data were spline-fitted to the unstalled experimental points and used as inputs to the theory to represent the unstalled losses through the stator row.

4. Turning Angle of the Flow Through the Stator Row

The final input required by the rotating-stall stability theory is the turning angle of the flow through the stator row. The prediction of rotating stall inception is only weakly dependent on this parameter, while measurement of the turning through the stator row would require extensive spatial surveys downstream of the stage with hot-wire equipment. These extensive surveys were judge to be not necessary in view of the weak

dependence of the theoretical predictions on the results. Thus, the turning through the stators was estimated on the basis of correlations developed in Reference 1. The turning data used in the theory has been presented in Figure 32, of Reference 1 and is reproduced here in Figure 17. A full discussion of the correlation is presented in Reference 1.

5. Effect of Inlet Distortion

In Reference 1, the results of an extensive series of tests on an isolated rotor with stationary and rotating inlet distortion were presented. The tests on stationary distortion effects on a rotor row included both a two-lobed and a four-lobed circumferential distortion pattern. Although the total pressure distortions were quite high for both patterns, they did not significantly affect the rotating stall boundary or the rotating stall properties after inception. Similarly, measurements of averaged steady-state blade row loss and turning data prior to inception showed little influence of the distortion. The tests with moving distortion were performed by rotating the two-lobed pattern about the compressor axis, both in the direction of blade row rotation and opposite to it. It was found that the rotating distortion pattern either had little effect on, or else destructively interfered with rotating stall formation, except when the pattern was rotated at speeds near the natural stall propagation velocity for undistorted flow. Under these latter conditions, the rotor incurred rotating stall at much higher flow coefficients than for the undistorted flow case. A linearized small disturbance analysis was developed to predict the effect of rotating distortion. The theoretical analysis was in general agreement with the experimental findings. The theory concluded that if the steady-state blade row performance is unchanged in the presence of distortion, then the rotating stall boundary will not be influenced unless the rotating distortion pattern contains a Fourier component which corresponds to the natural rotating stall mode for the system.

Moreover, it was pointed out that the linearized small-disturbance theory would result in a similar conclusion for multiple blade rows such as in a rotor-stator stage. That is, the distortion would not affect rotating stall inception unless the averaged steady-state blade row performance changed or unless the distortion was rotated at a speed near that of naturally occurring rotating stall. If the distortion is stationary, then only a change in averaged steady-state turning and loss performance would affect inception and the two-blade row rotating stall theory for undistorted inlet flow should be applicable to the stage with distortion. A limited investigation of this possibility was performed during the current program.

The two-lobed circumferential distortion screen used for tests on the isolated rotor in Reference 1 was installed upstream of the stage as shown in Figure 4. Detailed calibrations of the distortion generated by this screen are presented in Reference 1. A brief summary of the results is given in Part A. 3 of this section.

The rotating stall inception boundary was determined on the stage with inlet distortion for stator stagger angles of 28.2 and 37.2 degrees. The results are presented in Table 3, along with similar results obtained on the stage without distortion and on the isolated rotor. As mentioned previously, the presence of inlet distortion had very little effect on rotating stall inception on the isolated rotor. With the stage, inlet distortion delayed inception by a small amount for both stator stagger angles. This unexpected result may be due to destructive interference between naturally occurring rotating stall on the stage, and the disturbances generated by the distortion screen. A similar result was observed, in some instances, on the isolated rotor with rotating distortion (Reference 1) and on a stator row with a disturbance generator mounted between the stator blades (Reference 2). It is also possible that the delay in inception was caused by changes in blade row steady-state performance in the presence of inlet distortion. The two blade row stability theory has been used to investigate the latter effect. The experimental steady-state performance data used as inputs to the theory for this application are described below.

Table 3

SUMMARY OF ROTATING STALL INCEPTION POINTS
WITH AND WITHOUT CIRCUMFERENTIAL INLET DISTORTION

TEST CONFIGURATION	ROTATING STALL INCEPTION WITH NO DISTORTION		ROTATING STALL INCEPTION WITH CIRCUMFERENTIAL DISTORTION	
	ROTOR RPM	FLOW COEFFICIENT	ROTOR RPM	FLOW COEFFICIENT
ISOLATED ROTOR	1000	0.517	1000 TO 1010	0.517 TO 0.512
ROTOR-STATOR, δ_{SM} = 28.2 deg	1035	0.500	1085	0.477
ROTOR-STATOR, δ_{SM} = 37.2 deg	1105	0.468	1160 TO 1165	0.446 TO 0.444

In Reference 1, it was found that the circumferential distortion screen had a negligible effect on the total pressure rise across the isolated rotor. This is illustrated in Figure 18, where the dimensionless total pressure rise across the rotor with and without distortion is shown as a function of flow coefficient. The same result was assumed to hold for the rotor in the rotor-stator stage. Thus, the undistorted total pressure rises for the rotor in the stage with the two stator stagger angles (Figure 11), were used to calculate the corresponding relative loss coefficients for the rotor in the stage with inlet distortion

Also in Reference 1, it was found that the presence of inlet distortion had only a small, almost constant effect on the turning of the flow through the isolated rotor. The results from that study are shown in Figure 19. Here, radial distributions of average swirl angle downstream of the isolated rotor with inlet distortion are compared to data obtained without inlet distortion. The data obtained with inlet distortion are averages of 20 measurements made at different circumferential locations downstream of the isolated rotor. In Figure 19, one degree has been added to the data measured with inlet distortion, so that direct comparisons can be made with the shapes of the radial distributions for the isolated rotor without distortion. A similar presentation in Reference 1 (Figure 20) used a two degree increment for the distorted flow measurements. However, a one degree increment appears to provide a better correspondence with the undistorted data at the higher rotor speeds near rotating stall inception. It is evident from Figure 19 that inlet distortion reduced the outlet swirl angle from the rotor by an approximately constant one degree at rotor speeds near inception.

It was assumed that the rotor in the stage was similarly affected by the inlet distortion. This assumption has two effects in the application of the theory. The most obvious effect is that the angle of attack on the stators is reduced by one degree at any given rotor speed. The second effect is that the rotor work coefficient is decreased slightly for a given rotor

speed. The latter effect can be seen by rearranging Equation (72) in the following form:

$$\overline{\overline{C_w}} = \frac{2\,\overline{\overline{W_b W_1}}}{U_o^2} \approx \frac{2\,\overline{\overline{W_b}}}{U_o}\,\overline{\overline{\tan\beta_1}}$$

where $\overline{\overline{\tan\beta_1}}$, is shown in Figure 15.

If the effect of distortion is to decrease $\overline{\overline{\beta_1}}$ by a constant one degree, then the rotor work coefficient with distorted flow becomes

$$\overline{\overline{C_{w_D}}} = \left(\frac{2\,\overline{\overline{W_b W_1}}}{U_o^2}\right) \approx \frac{2\,\overline{\overline{W_b}}}{U_o}\,\overline{\overline{\tan(\beta_1 - 1.0)}}$$

Further manipulation gives

$$\overline{\overline{C_{w_D}}} \approx \frac{\overline{\overline{C_w}} - (2\,\overline{\overline{W_b}}/U_o)\tan(1.0)}{1 + (\overline{\overline{C_w}}\,U_o/2\,\overline{\overline{W_b}})\tan(1.0)} \qquad (75)$$

The area-weighted relative loss coefficient for the rotor in the stage with distortion then becomes,

$$(-\overline{\overline{\Delta C_{P_{TR}}}})_D \approx \overline{\overline{C_{w_D}}} - \overline{\overline{\Delta C_{P_{T_1}}}}_{\substack{\text{STAGED ROTOR} \\ \text{WITHOUT DISTORTION}}} \qquad (76)$$

where the last term on the right is a consequence of the previous discussion of Figure 18.

In summary of the above discussion, the inputs required for application of the stability theory were obtained as follows. Equations (75) and (76) were used to estimate the relative losses through the rotor in the rotor-stator stage with distortion. The turning performance of the staged rotor was estimated from the data in Figure 15, corrected for one degree less turning. Stator row losses were taken from the data in Figure 16,

corrected for the one degree decrease in angle of attack. Finally, the stator row turning was taken from the correlation shown in Figure 17.

D. LOW HUB-TO-TIP RATIO ANNULAR CASCADE

At the conclusion of the test program on the high hub-to-tip ratio configuration of the annular cascade, major modifications were made to the hub of the annular cascade to provide it with a lower hub-to-tip ratio. The modified installation is shown in Figure 20.

The new hub was designed to accept the first stage rotor from a J-79 compressor at its normal and location relative to the J-79 outer casing which forms the test section of the annular cascade. This allows tests with the rotor alone, or with a stage consisting of the J-79 first stage rotor and first stage stator. The hub provides a constant area annulus with a hub-to-tip ratio of 0.44. The hub has an elliptical nose fairing at the front of the annulus, and the outer casing has the same bell mouth inlet as was used for the high hub-to-tip ratio configuration (Figure 2).

The rotor uses the original rotor hub section from the J-79 compressor to retain the blades. The original tapered hub was changed to a constant area design by filling the inter-blade spaces on the hub of the rotor blades. The tapered-end stator blades were converted to constant area by trimming the hub ends to the desired shape. The configuration of the stator blade hub-end fittings was retained to allow use of the original stator hub support ring from the J-79 compressor. The final hub-to-tip ratio (0.44) of the new configuration was governed by the radial length of the original stator blade trailing edges. With this design, the rotor blade stagger angle is fixed, but the stator stagger is variable through the variable geometry mechanisms on the J-79 compressor casing.

The new hub configuration was designed to incorporate as much of the existing hydraulic rotor-drive system and downstream ducting as possible. Incorporation of these components into the design required the use of a transition section at the downstream end. The transition, shown on the left-hand side of Figure 20, decreased the annulus area to the original high hub-to-tip ratio value. Mass flow through the test section is controlled by the existing two-speed axial flow fan and variable damper system.

In addition to the hub modifications to the annular cascade, a new radial traverse system for total pressure and hot-wire probes was built. The new traverse is powered by a variable speed electric motor and is capable of traversing the larger radial distances associated with the new hub. Microswitches prevent accidental encounters between the probes and the test section hub and tip. The multiple-tube total pressure rake used in the current study has been modified for use with the new traverse. This rake covers only a fraction (1.5 inches) of the total radial span of the modified annular cascade. Full span surveys are obtained by traversing the rake to different radial locations. This procedure has been adopted to ensure that the rake is aligned approximately with the local flow direction, which is determined at each radial location from a Conrad arrowhead style yawmeter incorporated on the rake.

The full rotor-stator stage configuration was assembled and found to fit properly without interference. Following this, the stators were removed and checkout tests of the rotor alone were performed. The hydraulic drive system was found to be capable of driving the rotor to speeds in excess of 1200 rpm without vibration or interference problems. However, maintaining a given mean axial velocity in the test section requires considerably more power from the downstream fan than was required for the high hub-to-tip ratio configuration. It is now necessary to use the downstream fan on high speed to attain the 60 feet per second mean axial velocity normally used for the experimental studies. Previously, the low speed setting of the downstream fan was adequate for this purpose. The increased power requirement is a result of

the higher mass flow in combination with the small annulus area of the downstream ducting.

A brief study was performed to determine the boundary for rotating stall inception on the isolated rotor. Rotating stall was detected in two ways: first with static pressure taps on the outer casing at the axial location of the rotor quarter chord, and second, with the total pressure rake located immediately downstream of the rotor. In the latter case, the rake was traversed over the full span of the rotor blades to determine the radial extent of the rotating stall. Rotating stall inception was determined for two values of the mean axial velocity through the test section. The results are summarized in Table 4.

Table 4

ROTATING STALL INCEPTION ON LOW HUB-TO-TIP RATIO ROTOR

MEAN AXIAL VELOCITY, U_o, ft/sec	ROTOR RPM AT INCEPTION	FLOW COEFFICIENT AT INCEPTION	REMARKS
33.2	645	0.532	INTERMITTENT FULL SPAN STALL, NO HYSTERESIS
59.6	1150	0.536	

The rotating stall which occurred on the low hub-to-tip ratio rotor did not display hysteresis between inception with increasing rpm and disappearance of stall with decreasing rpm. Near inception, rotating stall was intermittent and was preceded by gradually increasing turbulent pressure fluctuations on the pressure transducers used to detect rotating stall. This occurred both with the outer casing static pressure taps and with the total pressure rake in the annulus downstream of the rotor. Radial surveys with the total pressure rake showed that rotating stall encompassed the full span of the rotor. Table IV presents the inception results measured at both values of mean axial

flow velocity. The flow coefficient, $U_o / \overline{W}_b$, at inception for both mean axial velocities agree quite well. This indicates that inception is not a function of Reynolds number over the speed range of these tests.

The experience gained in the preliminary tests on the modified annular cascade has shown that the rig is capable of operating in the range required for studies of rotating stall. The downstream constriction of the annulus used to accommodate the existing hydraulic drive and outlet ducting, and the associated increased power requirements for the downstream fan, cause a large increase in operating noise. As it now stands, the annular cascade would not be suitable for the performance of acoustic studies such as those reported in References 13 and 14.

Further modifications to the annular cascade are planned to incorporate a torque measuring apparatus on the rotor drive shaft. This will require disassembly and rework of the rotor drive system. In view of the operating noise problem, it is planned to remove the constriction in the downstream ducting at the time the torquemeter is installed. This should eliminate the operating noise problem so that additional acoustic studies can be performed.

E. SUMMARY

The current work on rotating stall in the annular cascade was designed to provide basic information on rotor-stator interference and provide input data for the rotating stall stability theory. This data was obtained with the 0.8 hub-to-tip ratio configuration. The basic experimental data required as inputs to the rotating stall theory are the steady-state losses across the compressor blade row. These are required in a coordinate system fixed to the blade row (relative losses). The determination of the relative losses through a rotor row requires the measurement of total pressure rise in a duct-fixed coordinate system and a measurement of the work done by the rotor. In previous tests on an isolated rotor, the work done by the rotor was determined from the velocity components measured downstream of the rotor with

a crossed hot-wire anemometer system. In this case, good agreement was found between the prediction of the stability theory and the experimentally determined stall boundary. However, the situation for a closely coupled stage is more complex because we could not measure the components of velocity between the rotor and stator. Thus, an attempt was made to determine the rotor work by measuring the total temperature rise across the rotor, instead of the velocity components. The results of the total temperature studies demonstrated that the rotor work coefficients calculated from the total temperature measurements between the rotor and stator were reasonably consistent in the mid-annulus region with the work coefficients calculated from velocity measurements downstream of the isolated rotor. However, the repeatability of the total temperature measurements was not good, and the data appeared to be contaminated by heat addition from the hydraulic drive for the rotor. It was concluded that the total temperature results were not accurate enough to provide an estimate of the work done by the rotor for use in calculating the relative losses across the rotor in a rotor-stator stage.

On the other hand, an extensive series of total pressure surveys showed that at a given rotor speed, there was significantly more total pressure rise through the rotor with the stator behind it, compared to the isolated rotor case. This could be due to either: (a) the rotor-stator interference produces more rotor work than the isolated case, or (b) the rotor-stator interference produces a reduction in the rotor losses (presumably by influencing boundary layer separation). For application of the stability theory, the latter assumption was made and the work through the rotor in the stage was assumed to be the same as for the isolated rotor case at the same rpm. Thus, the relative losses through the rotor were calculated from the total pressure rise across the rotor in the stage and the work done by the isolated rotor.

The rotating stall stability theory requires several other inputs, as well as the relative losses through the rotor in the rotor-stator stage. These inputs are: the turning angle of the flow through the rotor, the losses through the stator row, and the turning angle of the flow through the stator row. The methods used to estimate these parameters from the experimental data

are presented in the text, along with the results. The results are presented for two stagger angle settings of the stators in the stage.

It will be shown in the following section that the use of the above steady-state data for input to the rotating stall stability theory leads to predictions of rotating stall inception for the stage which are in almost exact agreement with the experimental results. Successful application of the theory with the inputs derived as discussed above suggests that rotor-stator interference has no effect on the work done by the rotor in the stage. However, this is not conclusive proof as to which effect (more rotor work or reduced rotor losses) is the cause of the significant increase in total pressure rise through the rotor when the stator is placed behind it. Resolving this point is an important factor for rotating stall research as well as for general compressor design practice. Hence, it is planned to perform additional experiments which will attempt to prove conclusively which effect is occurring.

The above experimental studies on the rotor-stator stage were performed with undistorted inlet flow. In addition to these experiments, a brief study was performed to investigate the effect of circumferential inlet distortion on rotating stall inception in the rotor-stator stage. Here again, two stator stagger angles were used. The inlet distortion delayed rotating stall inception by a small amount for both stator stagger angles. Possible reasons for this surprising result are discussed in the text. Analysis of the experimental data to estimate the inputs required by the rotating stall stability theory is presented.

The final portion of this section describes modifications to the annular cascade facility to reduce the hub-to-tip ratio from 0.8 to 0.44. Preliminary tests of the modified rig showed that it is capable of operating in the range required for studies of rotating stall. The rotating stall inception boundary for a low hub-to-tip ratio rotor is presented.

SECTION IV

COMPARISON BETWEEN THEORY AND EXPERIMENT FOR A CLOSELY COUPLED ROTOR-STATOR STAGE

A. INTRODUCTION

A stability theory for the prediction of rotating stall inception on a stage consisting of a rotor and a stator was developed in Reference 2. Initial application of the theory indicated that the addition of a stator row downstream of a rotor can stabilize the stage, a result which was in agreement with experimental data obtained in the annular cascade facility (Reference 1). However, quantitative comparisons between theory and experiment for conditions at inception of rotating stall were not satisfactory because of large and questionable extrapolations of the available steady state data required as inputs to the theory. The experiments required to provide the steady-state input data for application of the theory are presented in Section III. Here the theoretical predictions will be compared with the experimental results.

Comparisons between theory and experiment for an isolated rotor, a closely coupled rotor-stator stage, and the same stage with circumferential inlet distortion are presented in Section IV-B. The results of a theoretical investigation of the effect of changing the axial spacing between the rotor and stator in a stage are presented in Section IV-C. The overall results are summarized in Section IV-D.

B. COMPARISONS BETWEEN THEORY AND EXPERIMENT

Comparisons between experimental and predicted inception of rotating stall on an isolated rotor were presented in Reference 2 for three stagger angle settings of the rotor (δ_{RM} = 30, 40 and 50 degrees). The predicted inception points agreed very well with the experimentally observed inception points in all three cases. However, the experimental steady-state loss data for δ_{RM} = 40 degrees contained a small error near rotating stall inception. These data have

been corrected in the current study. In addition, the referenced loss data were obtained with a total pressure rake situated 3.9 inches from the rotor trailing edge. In the current program, the rotor losses were measured at this axial location and at an axial location 0.7 inches from the rotor trailing edge. The results, shown in Figure 14, were different, with slightly lower losses calculated from the total pressure measurements close to the rotor. Thus the stability theory was applied using both loss curves as inputs to the theory. Only those experimental data measured prior to rotating stall inception were used to estimate the relative losses through the rotor. The lines drawn through the data points in Figure 14 are the inputs used in the theory. In addition to the losses through the rotor, the theory requires the steady-state turning performance of the rotor. These data were estimated as discussed in Section III and are shown in Figure 15.

Computed damping factors for the isolated rotor are shown in Figure 21 as a function of rotor rpm. The results using loss data calculated from measurements with the total pressure rake at both axial locations are shown. Theoretical rotating stall inception occurs when the damping factor first goes to zero. Although the damping factors calculated from the two sets of loss measurements differ at low rotor speeds, they become the same at higher rotor speeds and indicate the same rotor speed (998 rpm) at inception. Experimentally observed rotating stall inception, shown by an arrow in Figure 21, occurred at 1000 rpm. Thus the predicted and experimental inception points for the isolated rotor agree almost exactly in this case.

The inputs necessary for application of the stability theory to the rotor-stator stage require two other inputs in addition to the rotor loss and turning performance presented in Figures 14 and 15. These are the losses through the stator row and the turning through the stator row. The latter inputs were taken from Figures 16 and 17. In each instance, the input data appropriate to the stator stagger angle under investigation was used in the theory.

Computed damping factors for the stage are shown in Figures 22 and 23 for stator stagger angles of 28.2 and 37.2 degrees respectively. In each of these figures, the dashed curve labeled "rotor alone" shows the damping factor for the

rotor without the stator but with the losses measured for the rotor in the rotor-stator stage. The solid curves in Figures 22 and 23 show the damping factors for the complete rotor-stator stage.

The first application of the theory to the stage with a stator stagger angle of 28.2 degrees used a linear relation between stator losses and rotor speed in the higher rotor rpm range. In this case, the stator loss curve between 850 and 1025 rpm was taken as the straight dotted line shown in Figure 16. The predicted result for the stage damping factor is not shown in Figure 22 because there was very little difference between this curve and the curve for the rotor alone. In both cases, rotating stall inception was predicted at a rotor speed between 1015 and 1020 rpm, whereas experimental inception was observed at a rotor speed of 1035 rpm. While the agreement between these theoretical predictions and experiment appears to be quite good, the use of the straight-line stator loss approximation ignores the unstalled stator loss measured at a rotor speed of 1030 rpm (see Figure 16). This last unstalled loss measurement indicates that the stator loss coefficient began to decrease as rotating stall inception was approached. A second application of the stability theory was made to see if the apparent drop in stator loss coefficient near stall inception has a significant effect on inception. In this case, the straight line stator loss approximation was replaced by a spline fit to the unstalled data points (solid curve in Figure 16). In cases where two loss measurements were made, the spline fit used the average of the two data points. The measurement at 1030 rpm was included in the spline fit. With this stator loss curve, the calculated stage damping (solid curve in Figure 22) predicted a rotating stall inception point at 1042 rpm. This predicted value is in slightly better agreement with the experimental inception point (1035 rpm) than the prediction based on the straight line loss approximation (1017 rpm). Thus it is concluded that the drop in stator loss coefficient just before rotating stall inception has a small, but significant effect on the stability of the rotor-stator stage.

The predicted stability of the stage with a stator stagger angle of 37.2 deg. is shown in Figure 23. In this case, there is a substantial difference between the stability of the rotor alone and the stability of the complete stage. The rotor alone has a region of instability between rotor speeds of 939 and 983 rpm while the stage is highly stable in this region. Rotating stall inception for the stage is predicted at a rotor speed of 1109 rpm. Experimental inception

was observed at a rotor speed of 1105 rpm. The agreement between theory and experiment is excellent in this case. It is worth noting that for this stagger angle (δ_{SM} = 37.2 deg.), the measured stator loss curve (Figure 16) began to drop significantly in the rotor speed range between approximately 900 and 1000 rpm. This is the same speed range where the rotor alone displays an unstable region and the stage displays high stability. This behavior reinforces the conclusion that the stator loss characteristics can have a significant effect on the stability of the stage. It may be possible to take advantage of the stabilizing effect of the stator loss curve in designing a compressor. For instance, it may be possible to design a highly stable compressor by offsetting the locations of the drag buckets for the rotor and stator, provided, of course, that the stage efficiency does not decrease to unacceptable levels.

Past experience with the two-blade-row stability theory has shown that the theory generally results in a minimum number of stall cells below which no unstable solutions are found, and that this minimum number corresponds to the number of cells observed experimentally. A similar result was found in this study; one stall cell was found in the experiments and one stall cell was predicted by the theory as the minimum number of cells for an unstable solution on the rotor-stator stage.

Finally, rotating stall propagation velocities were not predicted very well by the theory. This is illustrated in Figure 24 which shows the theoretical propogation velocities relative to the rotor. The range of results from experimental measurements are shown as shaded bands for comparison. The experimental measurements showed relative propagation velocites between 35 and 45 percent of the rotor speed for the isolated rotor. (This corresponds to absolute propagation velocities between 65 and 55 percent of the rotor speed in the direction of the rotor velocity.) Similar measurements for the stage lie in the range between approximately 60 and 70 percent of the rotor speed. Conversely, the predicted disturbance propagation velocities vary widely with rotor speed, particularly for the stage with δ_{SM} = 28.2 degrees. At theoretical inception, the predicted propagation velocities relative to the rotor are too large in all cases.

The poor predictions of stall cell propagation velocity may result from the fact that the theory is a linearized theory and cannot be expected to apply after rotating stall has started. On the other hand, the experimental measurement of propagation velocity can be made only after rotating stall has started. The theory does predict one trend in propagation velocity which appears consistent with the experimental data. The predicted relative propagation velocities for the isolated rotor are approximately 50 to 60 percent lower than those for the rotor-stator stage. Similarly, experimental relative propagation velocities on the isolated rotor are approximately 60 percent lower than those on the stage.

The final comparison between theory and experiment is for the rotor-stator stage with circumferential inlet distortion. Experimentally, the distortion delayed rotating stall inception on the stage for both stator stagger angles that were tested. The theory was applied to see if the delay in inception can be predicted from the stage performance measured in the absence of distortion but corrected for a one degree decrease in turning of the flow through the rotor. The justification for this procedure and the method of data analysis used to provide the steady-state inputs to the theory are presented in Section III.C.5.

Computed damping factors for the stage with distortion are shown in Figure 25 for the stage with a stator stagger angle, δ_{SM} = 28.2 degrees, and in Figure 26 for δ_{SM} = 37.2 degrees. Here again, the stability of the complete stage, and of the rotor alone with losses corresponding to the rotor in the stage are shown. Comparison of these figures with the corresponding figures (Figures 22 and 23) for undistorted flow shows that the damping curves for the rotor alone are changed slightly and those for the stage are changed considerably. However, predicted inception on the stage is only delayed a small amount in both cases. For δ_{SM} = 28.2 degrees, predicted inception changes from 1042 rpm without distortion to 1049 rpm with distortion. For δ_{SM} = 37.2 degrees, the corresponding predictions are 1109 rpm without distortion and 1113 rpm with distortion. While the predicted delays in rotating stall incpetion show the proper trend, the magnitudes of the delays are not large enough to provide accurate predictions of the experimentally observed rotating stall inception points. The latter occurred at 1085 rpm for δ_{SM} = 28.2 degrees and at approximately 1160 rpm for δ_{SM} = 37.2 degrees.

Application of the theory to the isolated rotor with distortion to obtain numerical results has not been undertaken because for this case the results are obvious. The only input change required to consider the effect of distortion on the isolated rotor is a reduction of the flow turning through the rotor by one degree and a corresponding small change in the work performed by the rotor. The predicted inception point would be increased one or two rotor rpm's at most over that predicted for undistorted inlet flow. In this case, the result is in agreement with the experimental observations; on the isolated rotor, stationary inlet distortion had practically no effect on experimental rotating stall inception (see Table 3).

The apparent failure of the theory to predict rotating stall inception accurately for a stage with inlet distortion may be due to the assumptions made in estimating the steady-state blade row performance. These assumptions were based on the results of extensive measurements made on the isolated rotor with distortion and may not be representative of the rotor in the stage. The performance of even more extensive measurements to obtain accurate total pressure data for the rotor in the stage with distortion was not practical. Even with these results, it would still be necessary to use the isolated rotor work for calculating relative losses as discussed in Section III.

An alternative possibility for the inaccurate theoretical predictions of inception on the stage with distortion is the presence of destructive interference between the distortion pattern and the rotating stall which occurs naturally on the stage without distortion. This effect, which has been mentioned in Section III, was found to delay inception on the isolated rotor when the distortion pattern was rotated about the compressor axis at approximately half of the rotating stall propagation velocity (Reference 1, Figure 28). On the stage, the absolute propagation velocity was quite slow, about 30 to 40 percent of the rotor speed. Thus, if destructive interference occurs on the stage in the same way as it did on the isolated rotor, it would have a maximum effect when the distortion pattern rotated near 15 to 20 percent of the rotor speed. This is slow enough that the range of occurrence could encompass stationary distortion. The magnitude of the delay in inception on the isolated rotor with distortion

attained a maximum of about 10 percent over that observed on the rotor without distortion. This is easily large enough to explain the approximately 5 percent increase in rotor speed for inception on the stage with distortion.

C. THEORETICAL EFFECTS OF BLADE ROW SPACING

The previous comparisons between theory and experiment demonstrated that the stability theory is highly accurate in predicting rotating stall inception on a rotor-stator stage without distortion. These comparisons were made for a stage with the blade rows situated close together. Some further theoretical calculations have been made to display the effect of changing the axial spacing between the rotor and stator in the stage. The results are presented below.

The steady-state blade row performances used in these calculations were taken to be independent of blade row spacing. That is, the rotor and stator losses and turning were the same as those used for the closely-coupled stage discussed previously. Strictly speaking, it is incorrect to hold the blade-row performance constant as the axial spacing is changed. The experiments on the isolated rotor and on the rotor in the stage showed that losses through the rotor (Figure 14) change considerably when the rotor has a stator row added immediately downstream. Thus, one would expect the rotor losses to change from the closely-coupled stage values to the isolated rotor values as the distance between the blade rows is increased. Nevertheless, it is instructive to examine the stability of the system as a direct function of blade-row spacing, without considering the (unknown) effects of spacing changes on blade-row performance.

The stage configuration selected for this study used a stator stagger angle of 37.2 degrees. In the previous results for this configuration, the theoretical results displayed a large difference between the stability of the rotor alone (but with the losses of the rotor in the stage), and the stability of the stage (Figure 23). The large differences facilitate comparisons to see how the stage stability approaches that of the rotor alone as the axial spacing

between the blade rows is increased. The closely-coupled stage used in the comparisons between theory and experiment had an axial spacing of 1.5 inches between the mid-chords of the rotor and stator blades (Figure 4). The additional theoretical calculations used mid-chord axial spacings of 3, 6 and 12 inches. The results are shown in Figures 27(a), (b) and (c).

Computed damping factors for the stage with different blade row spacings are shown in Figures 27(a), (b) and (c) as a function of rotor speed. The damping factor of the rotor alone is shown for comparison. Each part of Figure 27 shows the calculated damping for a given number of stall cells and variable axial spacing. Figure 27(a) presents the results for one stall cell, 27(b) for three stall cells, and 27(c) for seven stall cells. Larger numbers of stall cells provided results very close to those found for seven cells (Figure 27(c)). For the rotor alone, the magnitude of the damping factor is a function of the number of stall cells, but the rotor speeds where the damping equals zero are not a function of number of cells. Thus, the regions of instability for the rotor alone remain unchanged in all three parts of Figure 27. However, for the stage, the zero damping points do depend on the number of stall cells. This can be seen by comparing the stage damping factors in Figures 27(a), (b) and (c).

In the experiments on the close-coupled stage (T_c = 1.5 inches), rotating stall inception was found to occur at a rotor speed of 1105 rpm with one stall cell propagating. It was noted in the comparison between theory and experiment for this case that the theory generally results in a minimum number of stall cells below which no unstable solutions are found and that this minimum number corresponds to the number of cells observed experimentally. This result can be seen by comparing the damping factors for T_c = 1.5 inches in Figure 27(a), (b) and (c). With one stall cell (Figure 27(a)), the damping factor for this case becomes zero at 1109 rpm. The corresponding rotor speeds for higher numbers of cells are 1112 rpm with three cells (Figure 27(b)) and 1127 rpm with seven cells (Figure 27(c)). Thus theoretical rotating stall inception occurs first at 1109 rpm with one stall cell. This result is in excellent agreement with the experiments.

Now consider what happens as the blade row spacing is increased. For one stall cell (Figure 27(a)), increasing the spacing has little effect on predicted inception (1109 to 1111 rpm). For three stall cells (Figure 27(b)), increased spacing makes the stage slightly more stable at first (T_c = 3 inches) and then progressively less stable, approaching that of the rotor alone at T_c = 12 inches. With seven stall cells (Figure 27(c)), the damping factor for T_c = 6 inches is close to that of the rotor alone and for T_c = 12 inches it is the same as that of the rotor alone. Overall inspection of the results in Figures 27(a), (b) and (c) shows that the stage stability is a function of both the axial spacing between the blade rows and the number of rotating stall cells. Table 5 summarizes the unstable rotor speed ranges as a function of blade row spacing and number of stall cells. For the rotor alone and for 6 and 12 inch blade-row spacings in the stage, there is an instability at intermediate rotor speeds as well as a final instability at a higher rotor speed. Both unstable ranges are given in the table. The numbers of stall cells shown in each range were taken from the criterion that the minimum number predicted theoretically will usually occur. It is evident that the stability of the system changes with blade-row spacing and that the number of rotating stall cells is a nonlinear function of the spacing.

The above theoretical results display the effect of axial spacing in a stage for the situation where the spacing does not affect the steady-state performance of the blade rows. As discussed earlier, there is experimental evidence that the steady-state blade-row performance is not independent of the axial separation between the blade rows. Thus the assumption of constant blade-row performance is not correct, and the theoretical predictions should be used only as a guide to indicate trends. In this respect, the calculations show that changes in blade-row spacing change both the stability of the stage and the number of stall cells which occur at inception. The theory suggests that larger blade-row spacings will decrease the stability of the stage and increase the number of stall cells which occur at inception. However, both the stability and number of cells are nonlinear functions of blade-row spacing.

AD-A077 690 CALSPAN ADVANCED TECHNOLOGY CENTER BUFFALO NY AERODYN--ETC F/G 21/5
BASIC STUDIES OF ROTATING STALL IN AXIAL FLOW COMPRESSORS.(U)
SEP 79 G R LUDWIG , J P NENNI F33615-76-C-2092
UNCLASSIFIED CALSPAN-XE-5933-A-105 AFAPL-TR-79-2083 NL

2 OF 2
AD
A077690



END
DATE
FILMED
1-80
DDC

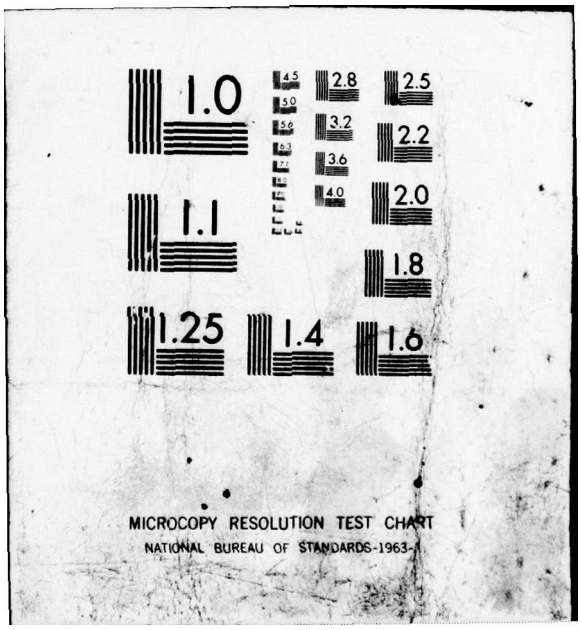

1.0
1.1
1.25
1.4
1.6
1.8
2.0
2.2
2.5
2.8
3.2
3.6
4.0
4.5
5.0
5.6
6.3
MICROCOPY RESOLUTION TEST CHART
NATIONAL BUREAU OF STANDARDS-1963-A

TABLE 5

THEORETICAL EFFECT OF BLADE ROW SPACING ON ROTATING STALL INCEPTION AND NUMBER OF CELLS

CONFIGURATION	ROTOR SPEED RANGE FOR UNSTABLE FLOW	NUMBER OF STALL CELLS
ROTOR ALONE	939 to 983 ≳ 1095	INDETERMINATE; PROBABLY ONE INDETERMINATE; PROBABLY ONE
STAGE WITH BLADE ROW AXIAL SPACING, T_c		
T_c = 1.5 INCHES	≳ 1109	ONE
T_c = 3.0 INCHES	≳ 1111	ONE
T_c = 6.0 INCHES	954 to 970 ≳ 1100	SEVEN SEVEN AT INCEPTION, PROBABLY CHANGING TO ONE.
T_c = 12 INCHES	939 to 983 ≳ 1095	SEVEN, PROBABLY CHANGING TO THREE. SEVEN AT INCEPTION, PROBABLY CHANGING TO THREE THEN ONE.

D. SUMMARY

The experimental steady-state measurements on an isolated rotor and on a rotor-stator stage have been used as inputs to the rotating stall stability theory. Final application of the theory to the stage configuration required the use of data measured on the isolated rotor as well as data measured on the stage. The theoretical predictions of rotating stall inception and of the number of stall cells which occur were found to agree extremely well with the experimental results. However, prediction of stall cell propagation velocity was poor. The theoretical results suggest that stator losses as well as the rotor losses play a major role in determining the stage stability. It may be possible to design a compressor which takes advantage of the stator loss characteristics to increase compressor stability.

A further application of the theory was made to see if the effects of inlet distortion could be predicted. Input data for the theory were estimated from steady-state data obtained on the isolated rotor with distortion and from stage data without distortion. For the isolated rotor, both the theory and the experiments showed negligible effects of inlet distortion. For the stage, the theory predicted rotating stall inception would be delayed only a very small amount by inlet distortion, while the experiments displayed a larger delay in inception.

A final application of the theory was made to study the theoretical effect of changing the axial separation between the blade rows in a stage. For this theoretical study, it was assumed that blade-row axial spacing has no effect on the steady-state blade-row performance. The experimental data showed that this assumption is not correct. Nevertheless, its use allowed a study of the direct effect of geometry on the stage stability. The results suggest that large blade-row spacings will decrease the stability of the stage and increase the number of stall cells which occur at inception. However, both the stage stability and number of cells are nonlinear functions of blade-row spacing.

SECTION V
SUMMARY AND CONCLUSIONS

A combined experimental and theoretical research program on rotating stall in axial flow compressors has been conducted. The theoretical studies were concerned with the development of an incompressible three-dimensional rotating stall stability theory and with revision of a two-dimensional stability theory for compressible flow. The major portion of the experimental program was oriented towards studying rotor-stator interference in a closely coupled rotor-stator stage. The experimental results have been compared with the predictions of an existing two-dimensional rotating stall stability theory for a rotor-stator stage.

In the theoretical studies, the two-dimensional stability theory for wholly subsonic compressible flows was modified through the revision of the energy matching conditions. Also the formulation of the theory to supersonic flow has been initiated and some analysis of the theory has been made with respect to the mechanisms of rotating stall in supersonic flows. In addition to the above, a stability theory for three-dimensional, incompressible flow was developed but not implemented because of extensive computational requirements. It appears that the stability of three-dimensional flows would be best studied through analysis of the response of the blade row rather than a stability theory approach.

The experimental studies on rotor-stator interference were performed in the Calspan/Air Force annular cascade in a configuration with a hub-to-tip ratio of 0.8. The investigation included measurements on an isolated rotor, a closely coupled rotor-stator stage, and the same stage with circumferential inlet distortion. The experiments on the stage were performed for two different stagger angle settings of the stators. With undistorted flow, it was found that the presence of the stators delayed rotating stall inception over that which occurs on the isolated rotor. Moreoever, prior to rotating stall inception, there was significantly more total pressure rise across the rotor with the stator

behind it than there was across the isolated rotor. This could be due to either: (a) the rotor-stator interference produces more rotor work than the isolated case, or (b) the rotor-stator interference produces a reduction in the rotor losses (presumably by influencing boundary layer separation). An attempt was made to resolve these possibilities by measuring the total temperature rise across the rotor. However, the results were not accurate enough to provide reliable estimates of the work done by the rotor.

The experimental steady-state performance data measured on the isolated rotor and on the stage were used to provide inputs to a two-dimensional rotating stall stability theory. The inputs required by the theory are the relative losses and the turning of the flow through the rotor and the losses and turning of the flow through the stators. Calculation of the relative losses through the rotor in the stage requires determination of the total pressure rise across the rotor and of the work done by the rotor. As noted above, attempts to measure the rotor work through total temperature measurements were not successful. However, the work done by the isolated rotor had been determined previously through an extensive series of velocity measurements. Thus for application of the stability theory, it was assumed that the work done by the rotor in the stage was the same as that done by the isolated rotor. This corresponds to assuming that the observed increase in total pressure rise across the rotor in the stage is a result of reduced losses through the rotor. With this input, the resulting stability boundary predictions from the theory agreed extremely well with the experimental stall inception boundary for the stage for both stator stagger angles that were tested. However, this result is not conclusive proof as to which effect, more rotor work or reduced rotor losses, is the cause of the significant increase in total pressure rise across the rotor when the stator is placed behind it. Resolving this point is an important factor for rotating stall research as well as for general compressor design practice.

In addition to predicting the conditions for rotating stall inception, the theory predicts the number of stall cells which will occur and the propagation velocity of the stall cells. The predicted number of stall cells agreed with the experiments but the prediction of stall cell propagation velocity was

poor. The poor predictions of propagation velocity may result from the fact that the theory is is a linearized theory and cannot be expected to apply after rotating stall has started. On the other hand, experimental measurements of propagation velocity can be made only after rotating stall has started. The theoretical results suggest that the stator loss characteristics can have a significant effect on the stability of the stage. It may be possible to take advantage of the stabilizing effect of the stator loss curve in designing a compressor. Finally, the theoretical effect of changing the axial separation between the rotor and stator in a stage is presented.

The above experimental studies were performed with undistorted inlet flow. In addition, a brief study was performed to investigate the effect of circumferential inlet distortion on rotating stall inception in the rotor-stator stage with two different settings of the stator stagger angle. The results were surprising; the presence of inlet distortion caused a delay in rotating stall inception for both stator stagger angles. A further application of the stability theory was made to see if these results could be predicted. Input data for the theory were estimated from steady-state data measured on the isolated rotor with distortion and from stage data without distortion. With these inputs the theory predicted a delay in inception but the delay was not as large as that observed experimentally. In contrast, for the isolated rotor, both the theory and experiments showed negligible effects of inlet distortion. The possibility that destructive interference between rotating stall and inlet distortion caused the delayed inception on the stage is discussed in the text. Such a phenomenon has been observed previously on an isolated rotor with a distortion pattern rotating about the compressor axis.

At the conclusion to the above studies, the annular cascade was modified to reduce the hub-to-tip ratio of the annulus from 0.8 to 0.44. These modifications are described along with the results of checkout tests and a preliminary study to investigate the rotating stall boundary on a low hub-to-tip ratio rotor.

REFERENCES

1. Ludwig, G.R., Nenni, J.P. and Erickson, J.C., Jr. "Investigation of Rotating Stall Phenomena in Axial Flow Compressors, Vol. I - Basic Studies of Rotating Stall" AFAPL-TR-76-48 June 1976

2. Ludwig, G.R., Nenni, J.P. and Arendt, R.H. "Investigation of Rotating Stall in Axial Flow Compressors and the Development of a Prototype Rotating Stall Control System" AFAPL-TR-73-45 May 1973

3. Smith, S.N. "Discrete Frequency Sound Generation in Axial Flow Turbomachines" University of Cambridge, Department of Engineering Report CUED/A-TURBO/TR 29 1971

4. Liepmann, H.W. and Roshko, A. Elements of Gasdynamics John Wiley & Sons 1956 p. 193

5. Pai, S.I. Viscous Flow Theory, Vol. I Laminar Flow Van Nostrand Co., Inc. 1956 p. 41

6. Vavra, M.H. Aero-Thermodynamics and Flow in Turbomachines John Wiley and Sons 1960 p.50

7. Shapiro, A.H. The Dynamics and Thermodynamics of Compressible Fluid Flow, Vol. 1 Ronald Press 1953 p. 160

8. Lichtfuss, H.J. and Starken, H. Supersonic Cascade Flow Progress in Aerospace Sciences, Vol. 15 Ed. Kuchemann, D. Pergamon Press 1974

9. Bauer, H.F. "Tables of Zeros of Cross Product Bessel Function $J'_p(\xi)\, Y'_p(k\xi) - J'_p(k\xi)\, Y'_p(\xi) = 0$" Math Comp 18 (1964) p. 128

10. Frazer, R.A., Duncan, W.J. and Collar, A.R. Elementary Matrices and Some Applications to Dynamics and Differential Equations Cambridge 1938

11. Coddington, E.A. and Levinson, N. Theory of Ordinary Differential Equations McGraw-Hill 1955

12. Ludwig, G.R. and Arendt, R.H. "Investigation of Rotating Stall Phenomena in Axial Flow Compressors, Volume III - Development of a Rotating Stall Control System" AFAPL-TR-76-48 June 1976

13. Lordi, J.A., Homicz, G.F. and Ludwig, G.R. "Investigation of Rotating Stall Phenomena in Axial Flow Compressors, Volume II - Investigation of Rotor-Stator Interaction Noise and Lifting Surface Theory for a Rotor" AFAPL-TR-76-48 June 1976

14. Homicz, G.F., Lordi, J.A. and Ludwig, G.R. "Aerodynamic and Acoustic Investigations of Axial Flow Fan and Compressor Blade Rows, Including Three-Dimensional Effects" AFAPL-TR-79-2061 August 1979

APPENDIX A

FUNCTIONS APPEARING IN THE THREE-DIMENSIONAL STABILITY THEORY

Eq. (53) appearing in Section II-C is given below along with the expression for the coefficients of the derivatives.

$$\Gamma_{i1} V_2 + \Gamma_{i2} V_2' + \Gamma_{i3} u_0 + \Gamma_{i4} u_0' + \Gamma_{i5} u_0''$$

$$+ \Gamma_{i6} u_1 + \Gamma_{i7} u_1' + \Gamma_{i8} u_1'' + \Lambda_{i1} p_0 + \Lambda_{i2} p_0'$$

$$+ \Lambda_{i3} p_1 + \Lambda_{i4} p_1' + \Lambda_{i5} p_2 + \Lambda_{i6} p_2' = 0$$

for $i = 1, \ldots, 6$

where

$i = 1$

$$\Gamma_{11} = jc k_1 + jn \left(B a_2 k_5 + D_2 k_{14} + \frac{B U_\infty}{2} k_1 \right) - \frac{2j}{n} \left(B k_3 a_2 + \beta_1 \right)$$

$$\Gamma_{12} = a_2 k_3 + k_1 U_\infty$$

$$\Gamma_{13} = -k_4 a_2''$$

$$\Gamma_{14} = -\frac{2j}{n} \left(B k_4 a_2 + \beta_2 \right)$$

$$\Gamma_{15} = 0$$

$$\Gamma_{16} = -k_1 a_2''$$

$$\Gamma_{17} = -\frac{2j}{n}\left(B k_1 a_2 + \beta_3\right)$$

$$\Gamma_{18} = 0$$

$$\Lambda_{11} = 0$$

$$\Lambda_{12} = 0$$

$$\Lambda_{13} = k_9$$

$$\Lambda_{14} = 0$$

$$\Lambda_{15} = \partial k_{10}$$

$$\Lambda_{16} = 0$$

$i = 2$

$$\Gamma_{21} = jcA_1 + k_2 a_2' + jn\left(B a_2 k_6 + D_2 k_4 + B\frac{U_\infty}{2} A_1\right) - \frac{2j}{n}\left(B k_7 a_2 + \beta_4\right)$$

$$\Gamma_{22} = a_2 k_7 + A_1 U_\infty$$

$$\Gamma_{23} = -k_1 a_2''$$

$$\Gamma_{24} = -\frac{2j}{n}\left(B k_1 a_2 + \beta_5\right)$$

$$\Gamma_{25} = 0$$

$$\Gamma_{26} = -A_1 a_2''$$

$$\Gamma_{27} = -\frac{2j}{n}\left(B A_1 a_2 + \beta_6\right)$$

$$\Gamma_{28} = 0$$

$$\Lambda_{21} = 0$$

$$\Lambda_{22} = 0$$

$$\Lambda_{23} = k_{10}$$

$$\Lambda_{24} = 0$$

$$\Lambda_{25} = k_{11}$$

$$\Lambda_{26} = 0$$

$i = 3$

$$\Gamma_{31} = -\frac{2j}{n} a_2' k_1 + B U_\infty k_1 - B k_3 a_2 - \beta_1 + B k_5 a_2 - \frac{j}{n} k_3 a_2'$$

$$\Gamma_{32} = \frac{j}{n} k_{12} a_2$$

$$\Gamma_{33} = B k_4 a_2'$$

$$\Gamma_{34} = -k_9 \frac{c}{n} - B k_4 a_2 - \beta_2 - \frac{j}{n} k_4 a_2'$$

$$\Gamma_{35} = \frac{j}{n} (k_{13} a_2 + U_\infty k_9)$$

$$\Gamma_{36} = B a_2' k_1$$

$$\Gamma_{37} = -k_{10} \frac{c}{n} - \frac{j}{n} k_1 a_2' - B k_1 a_2 - \beta_3 - \frac{j}{n} k_1 a_2'$$

$$\Gamma_{38} = \frac{j}{n} U_\infty k_{10}$$

$$\Lambda_{31} = j n k_8$$

$$\Lambda_{32} = 0$$

$$\Lambda_{33} = jnk_9$$

$$\Lambda_{34} = 0$$

$$\Lambda_{35} = jnk_{10}$$

$$\Lambda_{36} = 0$$

$i = 4$

$$\Gamma_{41} = A_1 \frac{c}{n} - \frac{j}{n} 2a_2' A_1 + Ba_2 (A_1 - K_0 k_4)$$

$$+ BU_\infty A_1 - Bk\, a_2 - \beta_4 + Bk_6 a_2 - \frac{j}{n} k_7 a_2'$$

$$\Gamma_{42} = \frac{j}{n} (-2A_1 a_2 - U_\infty A_1)$$

$$\Gamma_{43} = Ba_2' k_1$$

$$\Gamma_{44} = -k_{10} \frac{c}{n} - Bk_1 a_2 - \beta_5 - \frac{j}{n} k_1 a_2'$$

$$\Gamma_{45} = \frac{j}{n} U_\infty k_{10}$$

$$\Gamma_{46} = B A_1 a_2'$$

$$\Gamma_{47} = -k_{11} \frac{c}{n} - \frac{j}{n} k_1 a_2' - BA_1 a_2 - \beta_6 - \frac{j}{n} A_1 a_2'$$

$$\Gamma_{48} = \frac{j}{n} (-A_1 a_2 + U_\infty k_{11})$$

$$\Lambda_{41} = jnk_9$$

$$\Lambda_{42} = 0$$

$$\Lambda_{43} = jnk_{10}$$

$$\Lambda_{44} = 0$$

$$\Lambda_{45} = jn k_{11}$$

$$\Lambda_{46} = 0$$

$i = 5$

$$\Gamma_{51} = -a_2 K_1 k_{14}$$

$$\Gamma_{52} = 0$$

$$\Gamma_{53} = jc k_8 + a_2' k_{14} + jn\left(B a_2 k_{14} + B \frac{U_\infty}{2} k_8\right) + \partial a_2' k_{14}$$

$$\Gamma_{54} = \partial a_2 k_{14} + U_\infty k_8$$

$$\Gamma_{55} = 0$$

$$\Gamma_{56} = jc k_9 + jn\left(B a_2 k_4 + B \frac{U_\infty}{2} k_9\right) + k_{13} a_2'$$

$$\Gamma_{57} = a_2 k_{13} + U_\infty k_9$$

$$\Gamma_{58} = 0$$

$$\Lambda_{51} = 0$$

$$\Lambda_{52} = k_9$$

$$\Lambda_{53} = 0$$

$$\Lambda_{54} = k_{10}$$

$$\Lambda_{55} = 0$$

$$\Lambda_{56} = k_{11}$$

$i = 6$

$$\Gamma_{61} = -a_2 K_1 k_4$$

$$\Gamma_{62} = 0$$

$$\Gamma_{63} = jc k_9 + a_2' k_4 + jn\left(B a_2 k_4 + B \frac{U_\infty}{2} k_9\right) + k_{13} a_2'$$

$$\Gamma_{64} = k_{13} a_2 + U_\infty k_9$$

$$\Gamma_{65} = 0$$

$$\Gamma_{66} = jc k_{10} + jn\left(B a_2 k_1 + B \frac{U_\infty}{2} k_{10}\right)$$

$$\Gamma_{67} = k_{10} U_\infty$$

$$\Gamma_{68} = 0$$

$$\Lambda_{61} = 0$$

$$\Lambda_{62} = k_{10}$$

$$\Lambda_{63} = 0$$

$$\Lambda_{64} = k_{11}$$

$$\Lambda_{65} = 0$$

$$\Lambda_{66} = k_{15}$$

where

$$K_0 = r_T r_H$$

$$K_1 = -(r_H + r_T)$$

$$A_1 = -\frac{(r_T - r_H)^3}{6} = K_0 (r_T - r_H) + \frac{K_1}{2}\left(r_T^2 - r_H^2\right) + \frac{1}{3}\left(r_T^3 - r_H^3\right)$$

$$k_1 = K_0 \ln \frac{r_T}{r_H} + K_1 (r_T - r_H) + \frac{1}{2}\left(r_T^2 - r_H^2\right)$$

$$k_2 = -2\left\{r_H r_T (r_H + r_T) \ln \frac{r_T}{r_H} - \frac{3}{2}(r_H - r_T) r_H r_T - \frac{1}{6}\left(r_T^3 - r_H^3\right)\right\}$$

$$k_3 = (K_1^2 + 2K_0) \ln \frac{r_T}{r_H} - 3(r_T^2 - r_H^2)$$

$$k_4 = 2(r_T - r_H) - (r_H + r_T) \ln \frac{r_T}{r_H}$$

$$k_7 = -r_H r_T (r_H + r_T) \ln \frac{r_T}{r_H} + \frac{3}{2}(r_T - r_H) r_H r_T + \frac{1}{6}(r_T^3 - r_H^3)$$

$$k_8 = \ln \frac{r_T}{r_H}$$

$$k_9 = (r_T - r_H)$$

$$k_{10} = \frac{1}{2}(r_T^2 - r_H^2)$$

$$k_{11} = \frac{1}{3}(r_T^3 - r_H^3)$$

$$k_{12} = (r_H + r_T)^2 \ln \frac{r_T}{r_H} - 2(r_T^2 - r_H^2)$$

$$k_{13} = K_1 \ln \frac{r_T}{r_H} + (r_T - r_H) \cdot 2$$

$$k_{14} = -\frac{1}{2} \frac{(r_T^2 - r_H^2)}{r_H r_T} + \ln \frac{r_T}{r_H}$$

$$k_{15} = \frac{1}{4}(r_T^4 - r_H^4)$$

$$k_{16} = -\frac{1}{12}(r_T - r_H)^2$$

$$k_{17} = \frac{1}{2} \frac{(r_T - r_H)^2}{r_T^2 + 4 r_T r_H + r_H^2}$$

$$k_{18} = \ln \frac{r_T}{r_H} - \frac{3(r_T + r_H)}{r_T^2 + 4 r_T r_H + r_H^2}$$

$$k_{19} = \frac{k_8}{k_9}$$

$$k_{20} = \frac{k_{10}^2 - k_9 k_{11}}{k_9 k_{11} - 2 k_{10}^2}$$

$$k_{21} = \frac{k_9 k_{10}}{k_9 k_{11} - 2 k_{10}^2}$$

$$\beta_1 = D_2 \left[2 \ln \frac{r_T}{r_H} - \frac{r_T^2 - r_H^2}{r_H r_T} \right]$$

$$\beta_2 = D_2 \frac{(r_T - r_H)}{r_H r_T} + B \frac{U_\infty}{2} (r_T - r_H)$$

$$\beta_3 = D_2 \ln \frac{r_T}{r_H} + \frac{1}{4} B U_\infty (r_T^2 - r_H^2)$$

$$\beta_4 = D_2 \left[2(r_T - r_H) - (r_H + r_T) \ln \frac{r_T}{r_H} \right] - \frac{1}{2} B U_\infty A_1$$

$$\beta_5 = \beta_3$$

$$\beta_6 = D_2 (r_T - r_H) + B \frac{U_\infty}{6} (r_T^3 - r_H^3)$$

The coefficients of λ appearing in Eq. (57) Section III-B are given below.

$$F_{11} = B U_\infty k_1 - \beta_1 - k_{19} \left[A_1 \frac{c}{n} + B U_\infty A_1 - \beta_4 - 6 K_0 k_9 G_2 \frac{(m+M)}{M} \right]$$

$$- n k_{20} \left[c k_1 + n \left(D_2 k_{14} + B \frac{U_\infty}{2} k_1 \right) - \frac{2}{n} \beta_1 + n B \left(k_5 - \frac{2}{n^2} k_3 \right) \cdot G_2 \left(\frac{m+M}{M} \right) \right] - n (k_{19} + k_{21}) \left[c A_1 + n \left(D_2 k_4 + B \frac{U_\infty}{2} A_1 - \frac{2}{n^2} \beta_4 \right) + n B \left(k_6 - \frac{2 k_7}{n^2} \right) G_2 \left(\frac{m+M}{M} \right) \right] + \left\{ - \frac{j}{n} (2 k_1 + k_3) G_2 m - 6 k_{19} K_0 k_9 G_2 \frac{m}{M} + \frac{j}{n} k_{19} (2 A_1 + k_7) G_2 m + n^2 k_{20} B \left(k_5 - \frac{2}{n^2} k_3 \right) G_2 \frac{m}{M} + (k_{19} + k_{21}) n \left[j k_2 G_2 m + n B \left(k_6 - \frac{2 k_7}{n^2} \right) G_2 \frac{m}{M} \right] \right\} \cdot e^{-Mz}$$

$$H_{11} = \frac{j}{n} k_{12} G_2 \frac{(m+M)}{M} + k_{19} \left[A_1 U_\infty + 2 A_1 G_2 \frac{(m+M)}{M} \right] \frac{j}{n}$$

$$+ jn k_{20} \left[k_1 U_\infty + k_3 G_2 \left(\frac{m+M}{M} \right) \right] + jn (k_{19} + k_{21}) \left[A_1 U_\infty \right.$$

$$\left. + k_7 G_2 \frac{(m+M)}{M} \right] + \left\{ -\frac{j}{n} k_{12} G_2 \frac{m}{M} - k_{19} 2 A_1 G_2 \frac{m}{M} \frac{j}{n} \right.$$

$$\left. - jn k_{20} k_3 G_2 \frac{m}{M} - jn (k_{19} + k_{21}) k_7 G_2 \frac{m}{M} \right\} \cdot e^{-Mz}$$

$$F_{12} = \left\{ B k_4 G_2 m - k_{19} B k_1 G_2 m + jn k_{20} k_4 G_2 M m \right.$$

$$\left. + jn (k_{19} + k_{21}) k_1 G_2 m M \right\} e^{-Mz}$$

$$H_{12} = -k_9 \frac{c}{n} - \beta_2 - B k_4 G_2 \frac{(m+M)}{m} - k_{19} \left[-k_{10} \frac{c}{n} - \beta_5 - B k_1 G_2 \left(\frac{m+M}{M} \right) \right]$$

$$+ 2 k_{20} \left(\beta_2 + B k_4 G_2 \frac{(m+M)}{m} \right) + 2 (k_{19} + 2 k_{21}) \cdot$$

$$\left[B k_1 G_2 \frac{m+M}{M} + \beta_5 \right] + \left\{ B k_4 G_2 \frac{m}{M} - \frac{j}{n} k_4 G_2 m \right.$$

$$- k_{19} B k_1 G_2 \frac{m}{M} - \frac{j}{n} k_1 G_2 m - 2 k_{20} B k_4 G_2 \frac{m}{M}$$

$$\left. - 2 (k_{19} + k_{21}) B k_1 G_2 \frac{m}{M} \right\} \cdot e^{-Mz}$$

$$P_{12} = \frac{j}{n}\left(k_9 U_\infty + k_{13} G_2 \frac{m+M}{M}\right) - k_{19}\frac{j}{n} U_\infty k_{10} - \left\{\frac{j}{n} k_{13} G_2 \frac{m}{M}\right\} e^{-Mz}$$

$$F_{13} = \left\{ B k_1 G_2 m - k_{19} B A_1 G_2 m + jn k_{20} k_1 G_2 m M + jn (k_{19}+k_{21}) A_1 G_2 m M \right\} e^{-Mz}$$

$$H_{13} = -k_{10}\frac{c}{n} - \beta_3 - B k_1 G_2 \frac{m+M}{M} + k_{19}\left[k_{11}\frac{c}{n} + \beta_6 + B A_1 G_2 \frac{m+M}{M}\right] + 2 k_{20}\left(\beta_3 + B k_1 G_2 \frac{m+M}{M}\right) + 2 (k_{19}+k_{21})\left(\beta_6 + B A_1 G_2 \frac{m+M}{M}\right) + \left\{ -\frac{2j}{n} k_1 G_2 m + B k_1 G_2 \frac{m}{M} - k_{19} B A_1 G_2 \frac{m}{M} - \frac{j}{n}(k_1 + A_1) G_2 m - 2 k_{20} B k_1 G_2 \frac{m}{M} - 2 (k_{19}+k_{21}) \cdot B A_1 G_2 \frac{m}{M} \right\} \cdot e^{-Mz}$$

$$P_{13} = \frac{j}{n} U_\infty k_{10} - k_{19}\frac{j}{n} U_\infty k_{11} + \frac{j}{n} A_1 G_2 \frac{m+M}{M} k_{19} + \left\{ -k_{19}\frac{j}{n} A_1 G_2 \frac{m}{M} \right\} \cdot e^{-Mz}$$

$$F_{21} = -K_1 k_{14} G_2 \frac{(m+M)}{M} + \frac{j}{n}\left[-6K_0 k_9 + \frac{j}{n}(2A_1 + k_7)M\right] m G_2 e^{-Mz}$$

$$H_{21} = \frac{j}{n}\left\{A_1 \frac{c}{n} + BU_\infty A_1 - \beta_4 - 6K_0 k_9 G_2 \frac{m+M}{M}\right\}$$
$$+ \left\{\frac{j}{n} 6K_0 k_9 G_2 \frac{m}{M} - \frac{j}{n}(2A_1 + k_7) G_2 m - \frac{j}{n} 2A_1 G_2 m\right\} e^{-Mz}$$

$$P_{21} = \frac{1}{n^2}\left\{A_1 U_\infty + 2A_1 G_2 \frac{(m+M)}{M}\right\} - \frac{1}{n^2}\left\{2A_1 G_2 \frac{m}{M}\right\} e^{-Mz}$$

$$F_{22} = jk_8\left(c + n\frac{BU_\infty}{2}\right) + jn k_{14} B G_2 \frac{m+M}{M}$$
$$+ \left\{3k_{14} G_2 m - jn k_{14} B G_2 \frac{m}{M} - \frac{j}{n} B k_1 G_2 m M\right\} e^{-Mz}$$

$$H_{22} = k_8 U_\infty + 2k_{14} G_2 \frac{m+M}{M}$$
$$+ \left\{-2k_{14} G_2 \frac{m}{M} + \frac{j}{n}\left[G_2 m\left(\frac{j}{n} k_1 M\right)\right]\right\} \cdot e^{-Mz}$$

$$P_{22} = \frac{j}{n}\left\{-k_{10}\frac{c}{n} - \beta_5 - B k_1 G_2 \frac{m+M}{M}\right\} + \frac{j}{n}\left\{B k_1 G_2 \frac{m}{M} - \frac{j}{n} k_1 G_2 m\right\} \cdot e^{-Mz}$$

$$Q_{22} = -\frac{U_\infty k_{10}}{n^2}$$

$$F_{23} = j k_9 \left(c + B \tfrac{n}{2} U_\infty\right) + jnB k_4 G_2 \frac{m+M}{M} + \left\{ k_{13} G_2 m - jnB k_4 G_2 \frac{m}{M} - \frac{j}{n} B A_1 G_2 M m \right\} e^{-Mz}$$

$$H_{23} = k_9 U_\infty + k_{13} G_2 \frac{m+M}{M} + \left\{ -k_{13} G_2 \frac{m}{M} + \frac{j}{n} B A_1 G_2 m + G_2 m \left[M \frac{j}{n} (k_1 + A_1) - B A_1 \right] \right\} e^{-Mz}$$

$$P_{23} = \frac{j}{n} \left\{ -k_{11} \frac{c}{n} - \beta_6 - B A_1 G_2 \frac{m+M}{M} \right\} + \frac{j}{n} \left\{ B A_1 G_2 \frac{m}{M} - \frac{j}{n} (k_1 + A_1) G_2 m - \frac{j}{n} A_1 G_2 m \right\} e^{-Mz}$$

$$Q_{23} = -\frac{1}{n^2} U_\infty k_{11} + \frac{1}{n^2} A_1 G_2 \frac{m+M}{M} + \left\{ -\frac{1}{n^2} A_1 G_2 \frac{m}{M} \right\} e^{-Mz}$$

$$F_{31} = -K_1 k_4 G_2 \frac{m+M}{M} + \left\{ \frac{K_1 j}{2n} \left(6 K_0 k_9 - \frac{j}{n} (2A_1 + k_7) M\right) G_2 m + k_{16} B j n \left(k_5 - \frac{2k_3}{n^2}\right) G_2 m \right\} \cdot e^{-Mz}$$

$$H_{31} = k_{16}\left[jck_1 + jn\left(D_2 k_{14} + B\frac{U_\infty}{2}k_1\right) - \frac{2j}{n}\beta_1 + jn\left(Bk_5 - \frac{2}{n^2}Bk_3\right)\cdot G_2\frac{m+M}{M}\right] - \frac{K_1 j}{2n}\left[A_1\frac{c}{n} + BU_\infty A_1 - \beta_4 - 6K_0 k_9 G_2\frac{m+M}{M}\right]$$
$$+ \left\{-k_{16}jn\left(Bk_5 - \frac{2}{n^2}Bk_3\right)G_2\frac{m}{M} + k_{16}k_3 G_2 m - K_1\frac{j}{2n}\left[6K_0 k_9 G_2\frac{m}{M} - \frac{j}{n}(2A_1 + k_7)G_2 m - \frac{j}{n}2A_1 G_2 m\right]\right\}\cdot e^{-Mz}$$

$$P_{31} = k_{16}\left[k_1 U_\infty + k_3 G_2\frac{m+M}{M}\right] - \frac{K_1}{2n^2}\left[A_1 U_\infty + 2A_1 G_2\frac{m+M}{M}\right]$$
$$+ \left\{-k_{16}k_3 G_2\frac{m}{M} + \frac{K_1}{n^2}A_1 G_2\frac{m}{M}\right\}\cdot e^{-Mz}$$

$$F_{32} = jk_9\left(c + nB\frac{U_\infty}{2}\right) + jnBk_4 G_2\frac{m+M}{M}$$
$$+ \left\{(k_{13} + k_{14})G_2 m - jnBk_4 G_2\frac{m}{M} + \frac{K_1 j}{2n}Bk_1 G_2 M m - k_{16}k_4 G_2 M^2 m\right\}\cdot e^{-Mz}$$

$$H_{32} = k_9 U_\infty + k_{13} G_2 \frac{m+M}{M} + \left\{ -k_{13} G_2 \frac{m}{M} - \frac{K_1 j}{2n} \left[B k_1 G_2 m + \left(\frac{j}{n} M - B \right) k_1 G_2 m \right] + k_{16} \left[k_4 G_2 M m - \frac{2j}{n} B k_4 G_2 m \right] \right\} e^{-Mz}$$

$$P_{32} = + k_{16} \left\{ \frac{-2j}{n} B k_4 G_2 \frac{m+M}{M} - \frac{2j}{n} \beta_2 \right\} - \frac{K_1 j}{2n} \left\{ -k_{10} \frac{c}{n} - \beta_5 - B k_1 G_2 \frac{m+M}{M} \right\} + \left\{ k_{16} \frac{2j}{n} B k_4 G_2 \frac{m}{M} - \frac{K_1 j}{2n} \left[B k_1 G_2 \frac{m}{M} - \frac{j}{n} k_1 G_2 m \right] \right\} e^{-Mz}$$

$$Q_{32} = \frac{K_1}{2n^2} U_\infty k_{10}$$

$$F_{33} = j k_{10} \left(c + \frac{n}{2} B U_\infty \right) + jn B k_1 G_2 \frac{m+M}{M} + \left\{ -jn B k_1 G_2 \frac{m}{M} + \frac{K_1}{2} \frac{j}{n} M B A_1 G_2 m - k_{16} k_1 G_2 m M^2 \right\} e^{-Mz}$$

$$H_{33} = k_{10} U_\infty + \left\{ \frac{-K_1 j}{2n} \left[B A_1 G_2 m + \left(\frac{j}{n} M (k_1 + A_1) - B A_1 m \right) G_2 \right] + k_{16} \left[k_1 G_2 m M - \frac{2j}{n} B k_1 G_2 m \right] \right\} e^{-Mz}$$

$$P_{33} = -k_{16} \frac{2j}{n} \left[\beta_3 + B k_1 G_2 \frac{m+M}{M} \right] - \frac{K_1 j}{2n} \left[-k_{11} \frac{c}{n} - \beta_6 - B A_1 G_2 \frac{m+M}{M} \right] + \left\{ k_{16} \frac{2j}{n} B k_1 G_2 \frac{m}{M} - \frac{K_1 j}{2n} \left[B A_1 G_2 \frac{m}{M} - \frac{j}{n} (k_1 + A_1) G_2 m - \frac{j}{n} A_1 G_2 m \right] \right\} e^{-Mz}$$

$$Q_{33} = \frac{K_1}{2n^2}\left[k_{11}U_\infty - A_1 G_2 \frac{m+M}{M}\right] + \frac{K_1}{2n^2}\left\{A_1 G_2 \frac{m}{M}\right\} \cdot e^{-MZ}$$

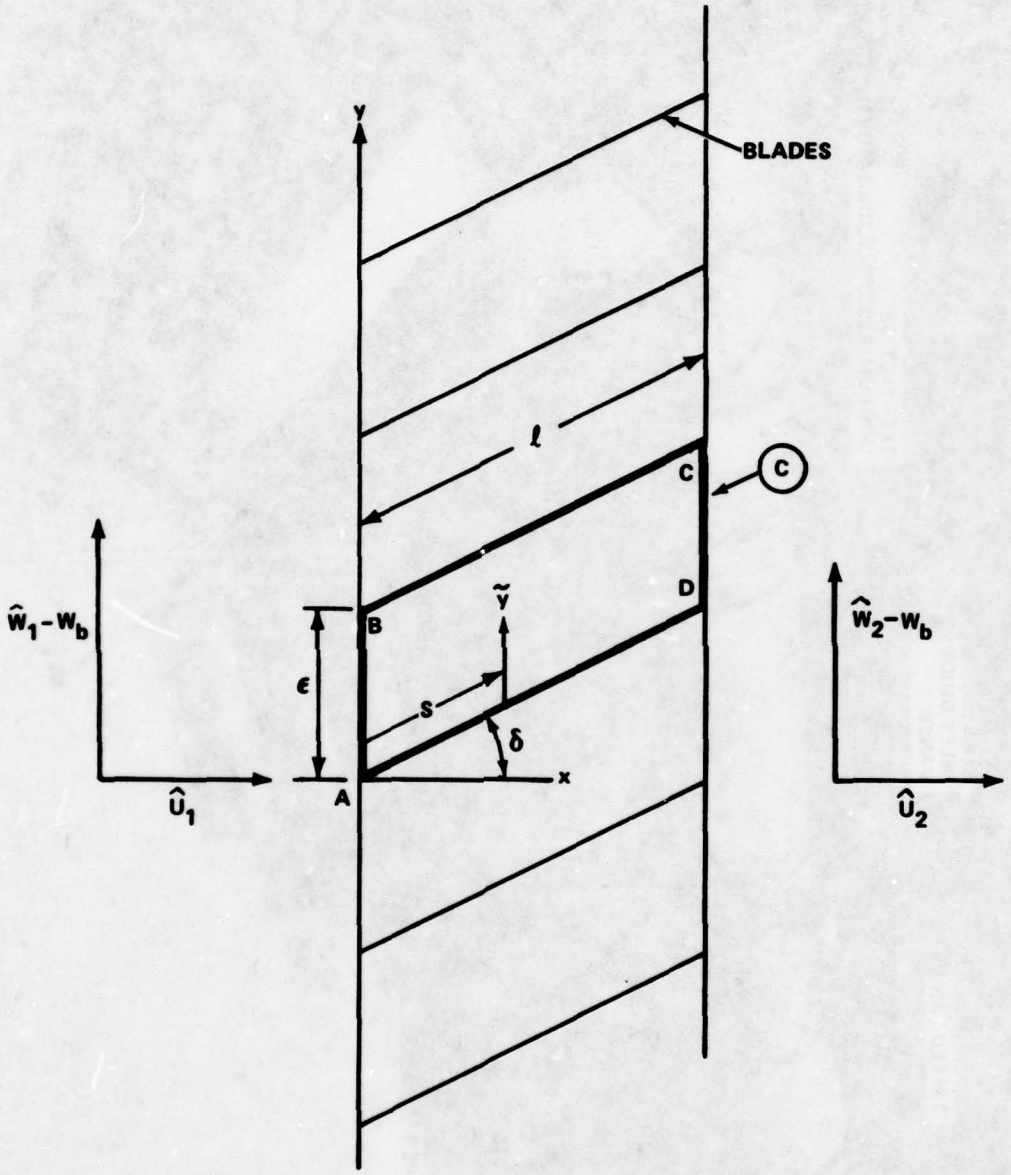


Figure 1 ACTUATOR MODEL FOR TWO-DIMENSIONAL ANALYSIS

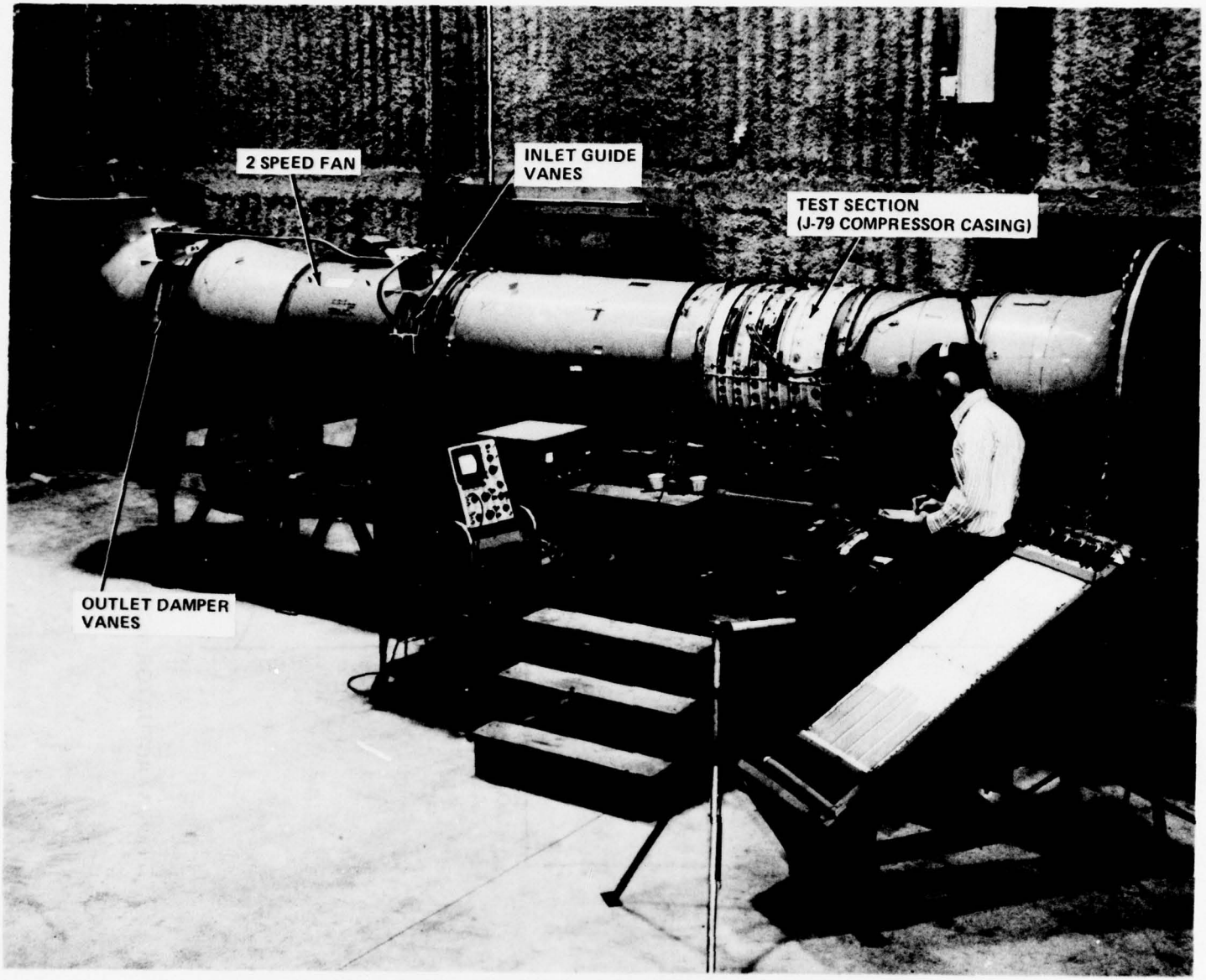


Figure 2 OVERALL VIEW OF ANNULAR CASCADE FACILITY

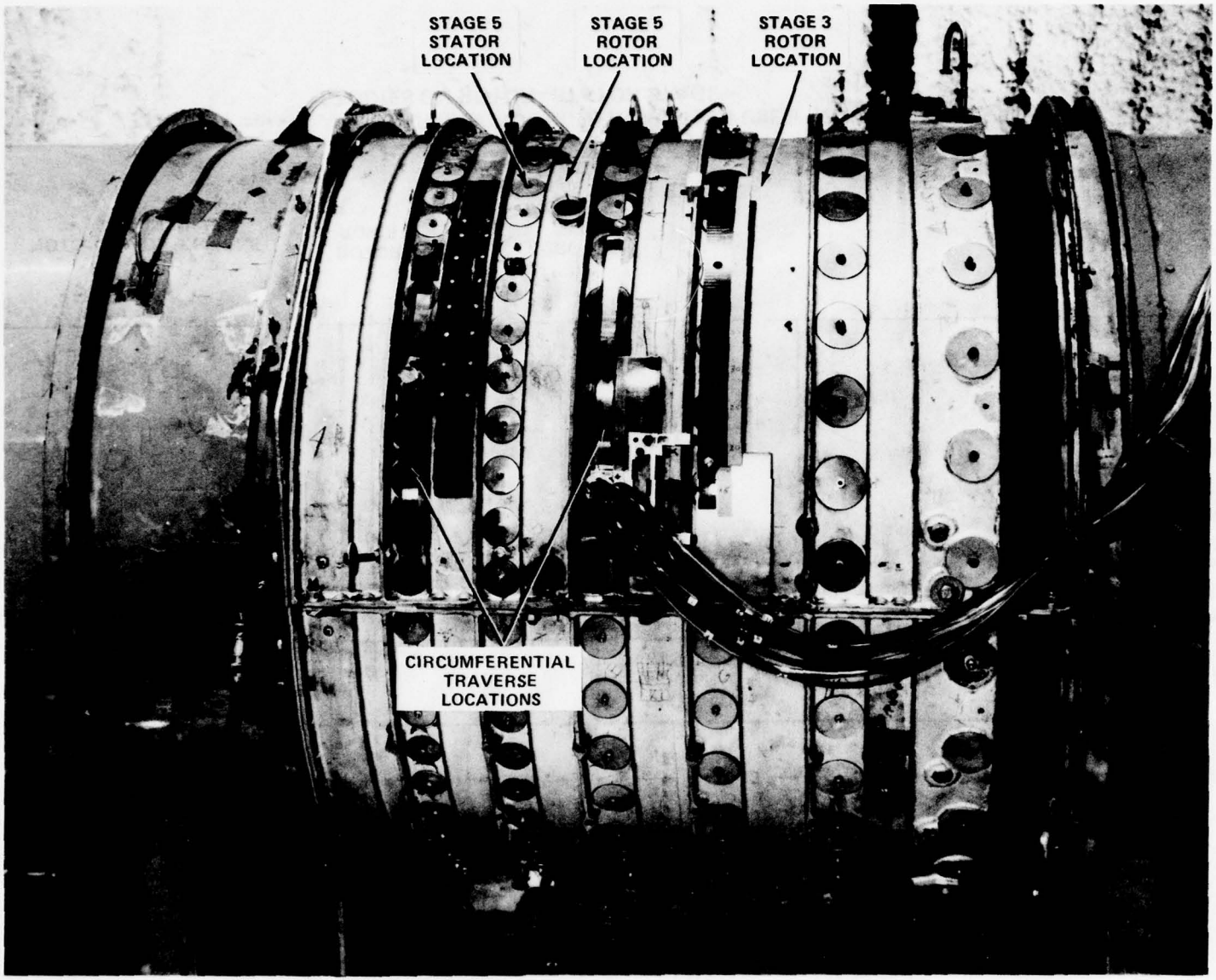


Figure 3 VIEW OF ANNULAR CASCADE TEST SECTION

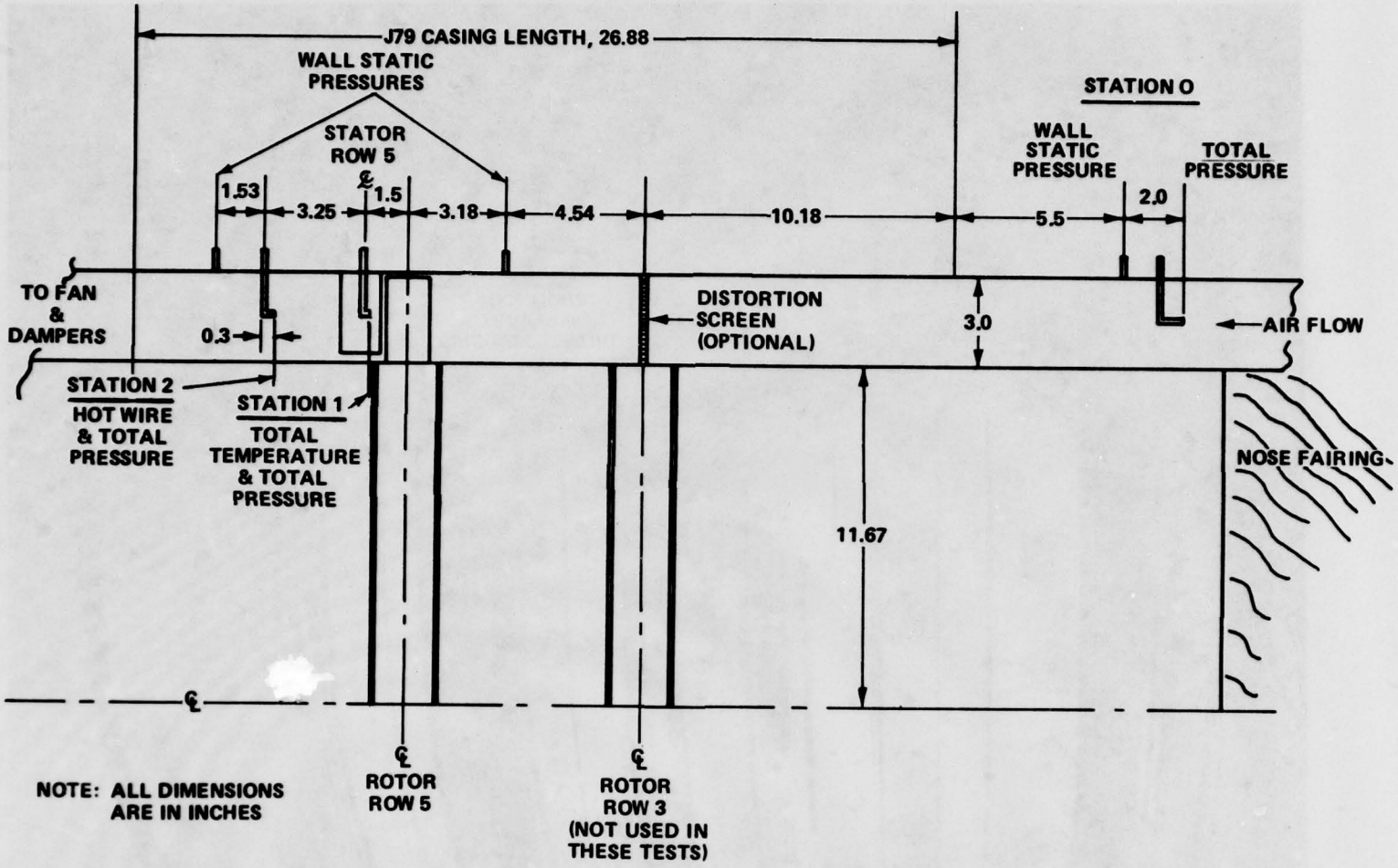


Figure 4 ANNULAR CASCADE CONFIGURATION USED FOR ROTATING STALL STUDIES ON ROTOR–STATOR STAGE

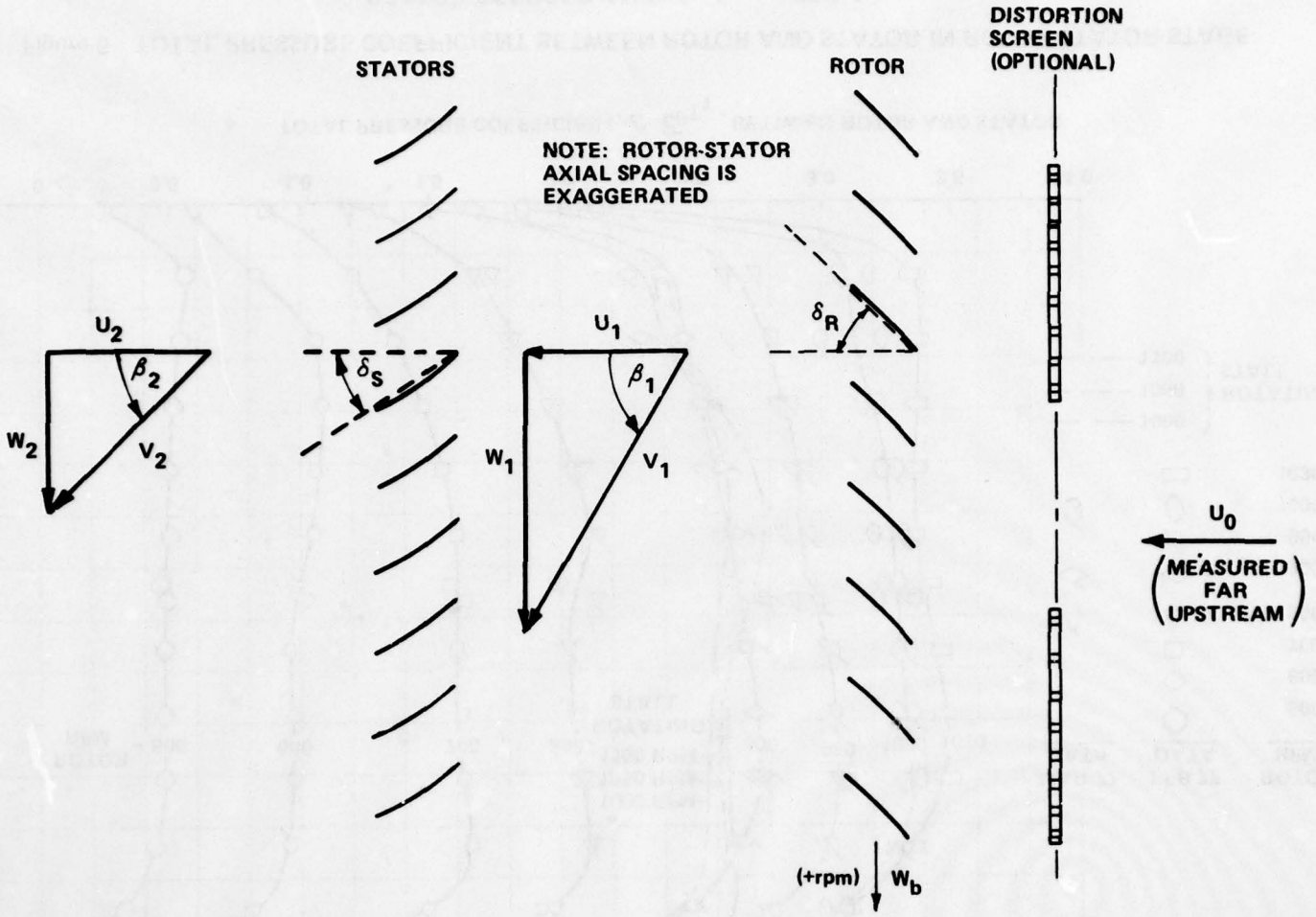


Figure 5 NOTATION FOR ANNULAR CASCADE WITH ROTOR-STATOR STAGE

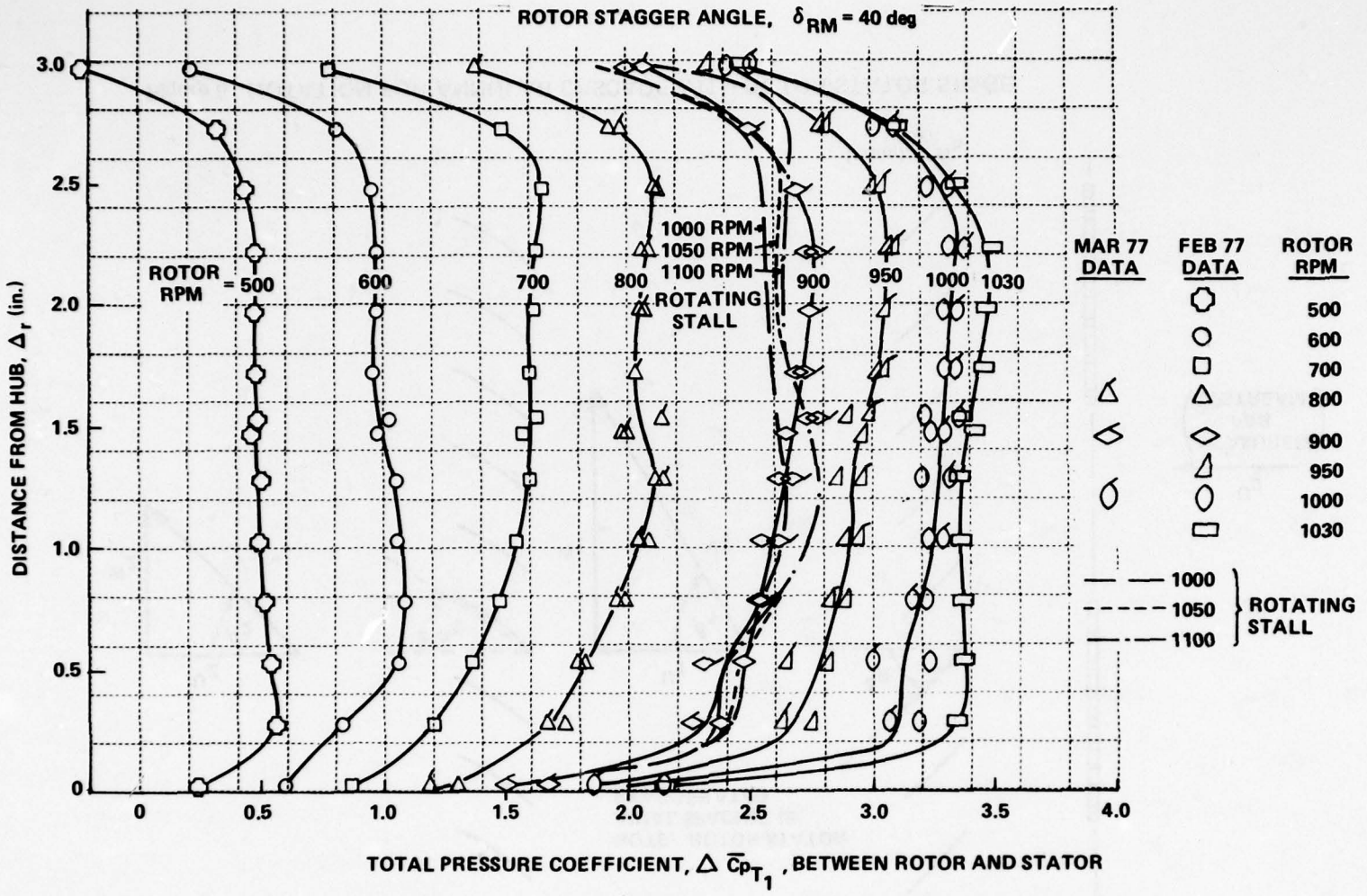


Figure 6 TOTAL PRESSURE COEFFICIENT BETWEEN ROTOR AND STATOR IN ROTOR-STATOR STAGE

a. STATOR STAGGER ANGLE, δ_{SM} = 28.2 deg

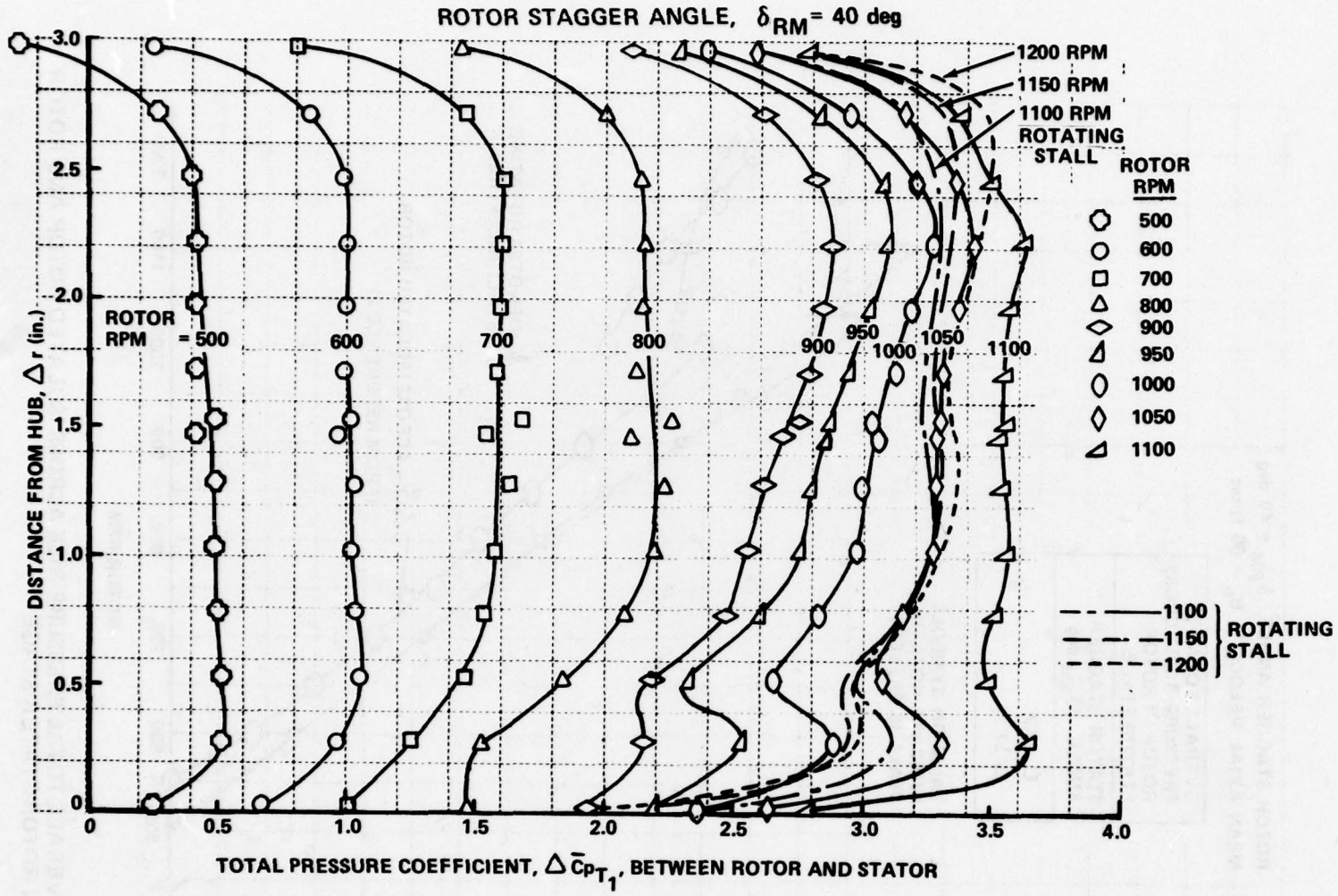


Figure 6 (Cont.) TOTAL PRESSURE COEFFICIENT BETWEEN ROTOR AND STATOR IN ROTOR-STATOR STAGE

b. STATOR STAGGER ANGLE, δ_{SM} = 37.2 deg

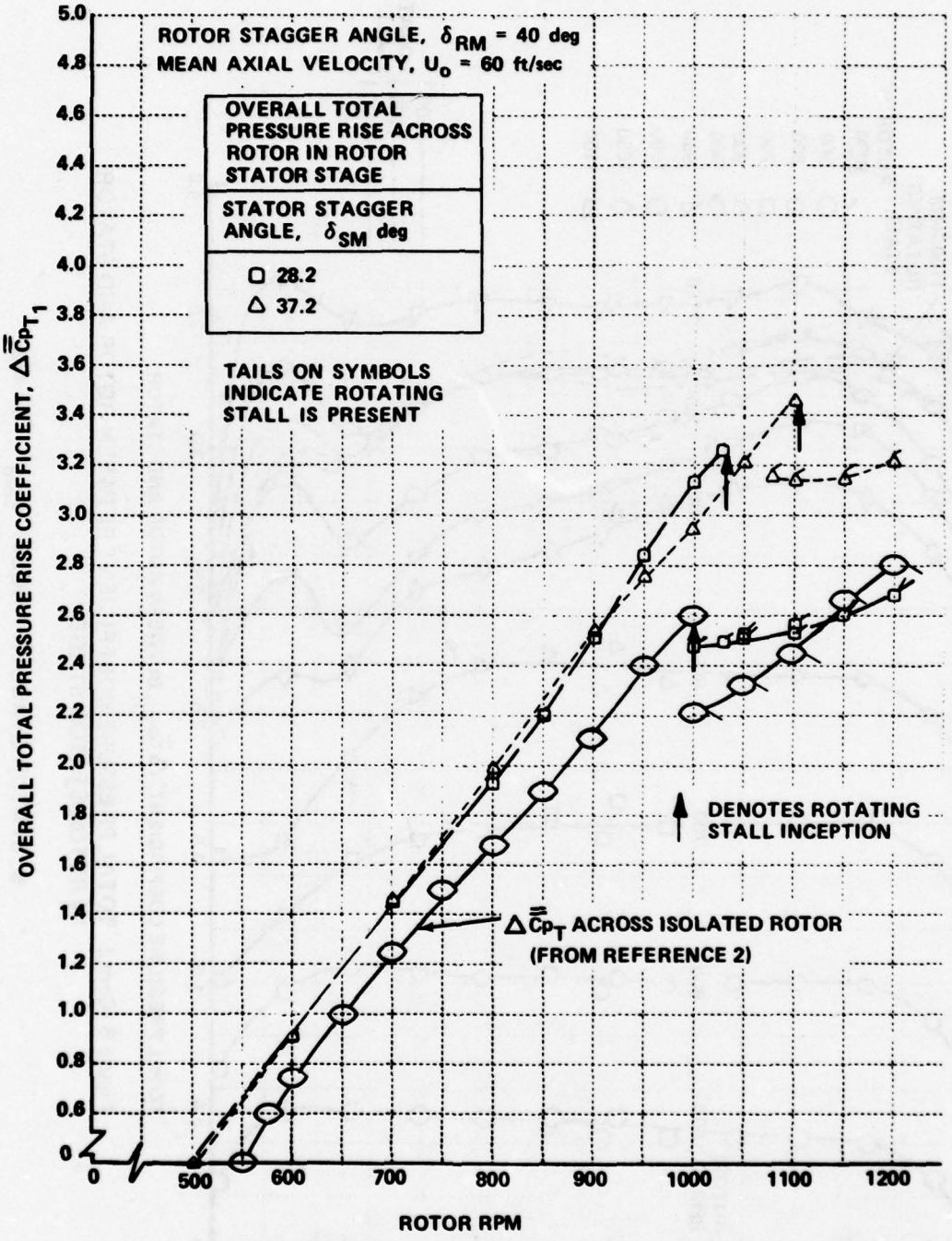


Figure 7 OVERALL TOTAL PRESSURE RISE ACROSS ISOLATED ROTOR AND ROTOR IN ROTOR-STATOR STAGE

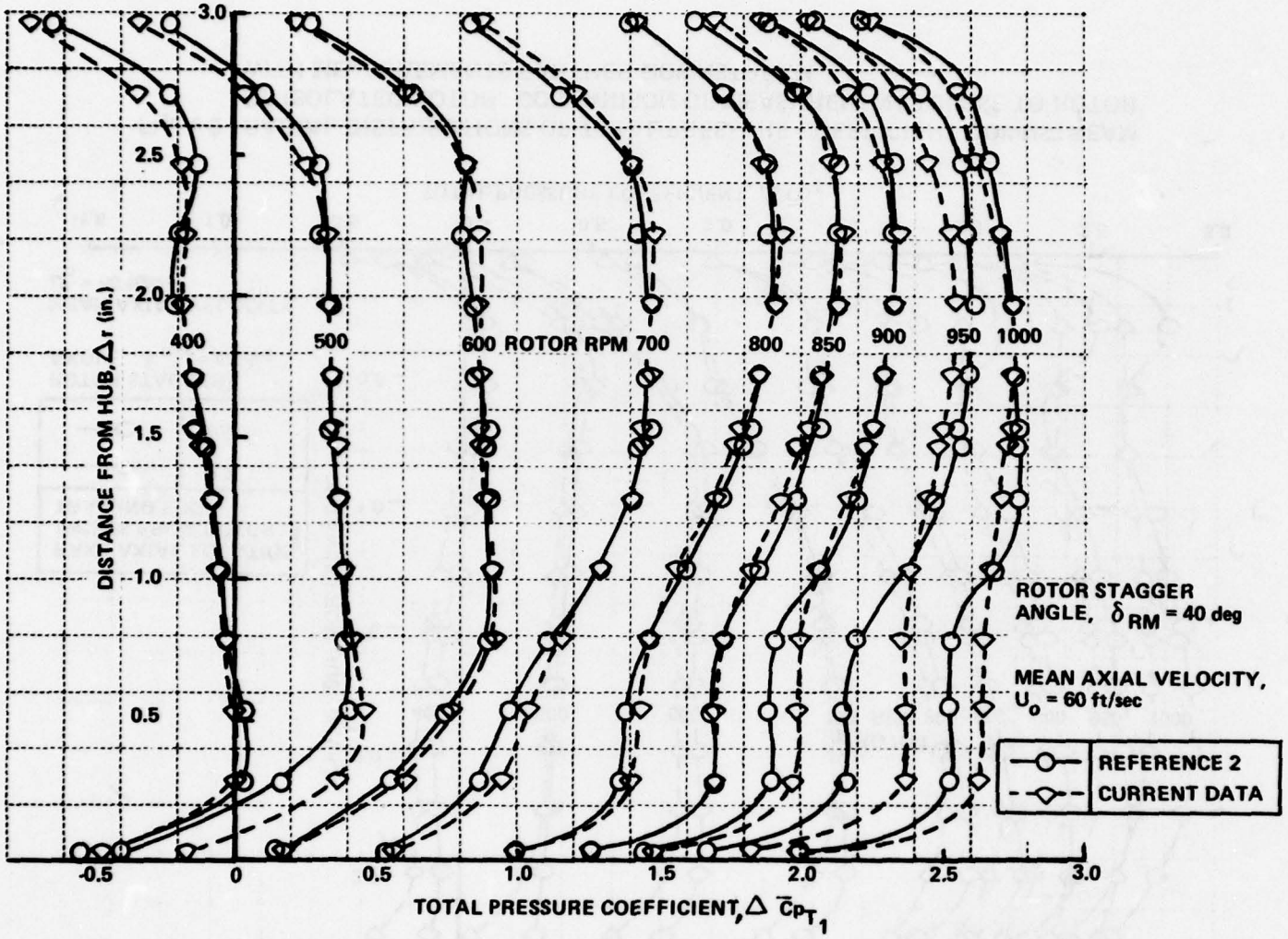


Figure 8 RADIAL DISTRIBUTIONS OF TOTAL PRESSURE COEFFICIENT DOWNSTREAM OF ISOLATED ROTOR. TOTAL PRESSURE RAKE LOCATED AT AXIAL DISTANCE 3.9 INCHES FROM ROTOR TRAILING EDGE

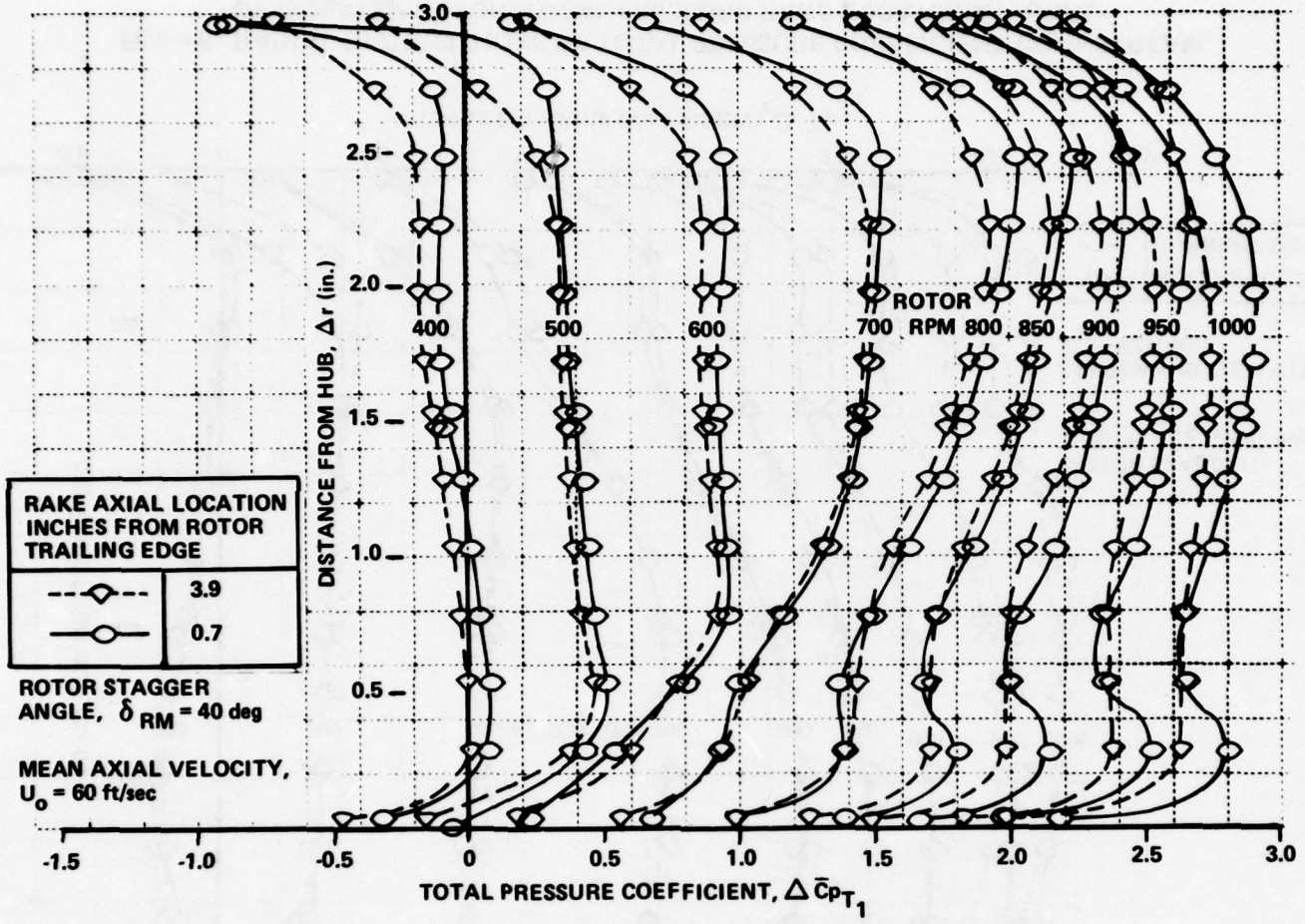


Figure 9 RADIAL DISTRIBUTIONS OF TOTAL PRESSURE COEFFICIENT DOWNSTREAM OF ISOLATED ROTOR. COMPARISON OF MEASUREMENTS CLOSE TO ROTOR WITH MEASUREMENTS FARTHER DOWNSTREAM

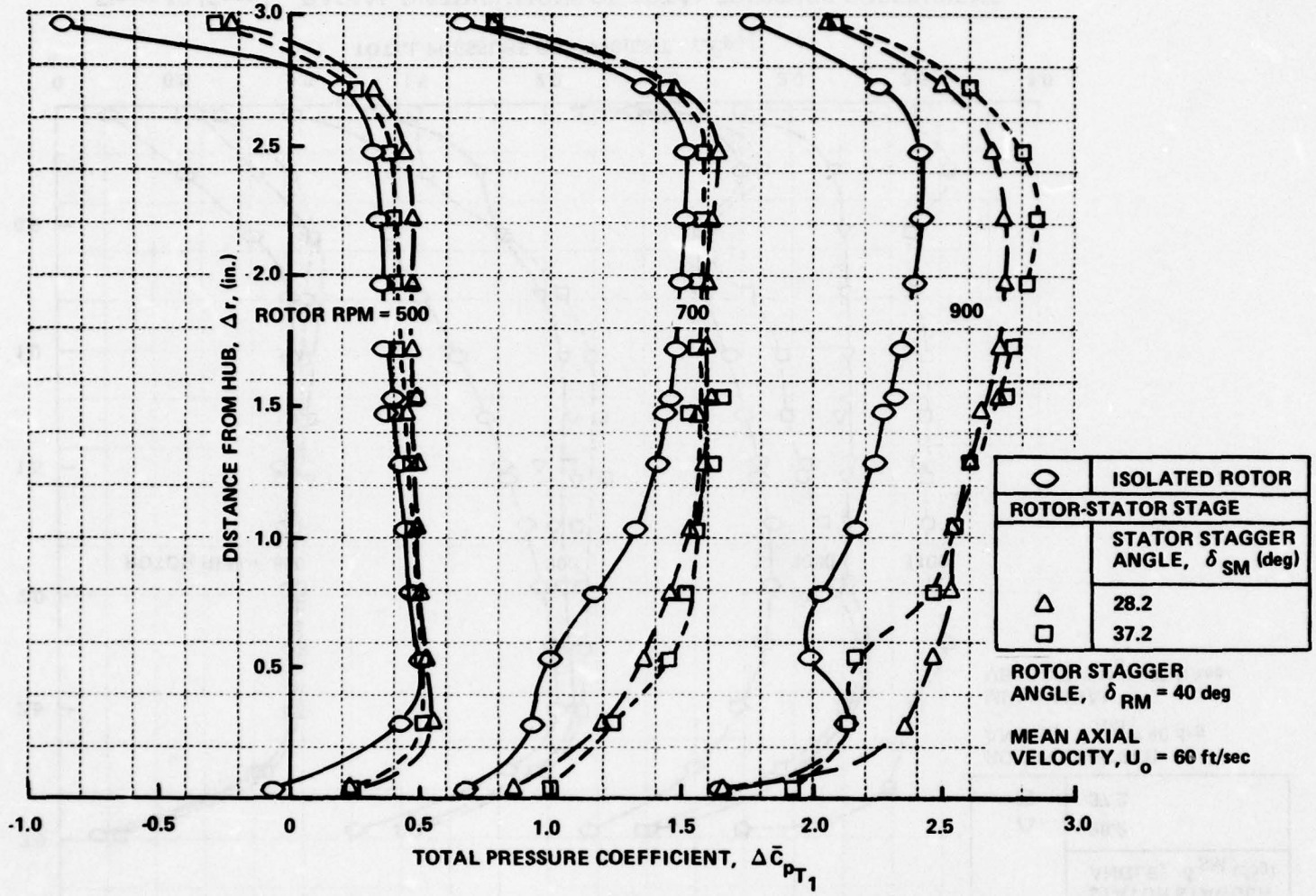


Figure 10 RADIAL DISTRIBUTIONS OF TOTAL PRESSURE COEFFICIENT IMMEDIATELY DOWNSTREAM OF ISOLATED ROTOR AND THE SAME ROTOR IN ROTOR-STATOR STAGE

a. ROTOR RPM = 500, 700, 900

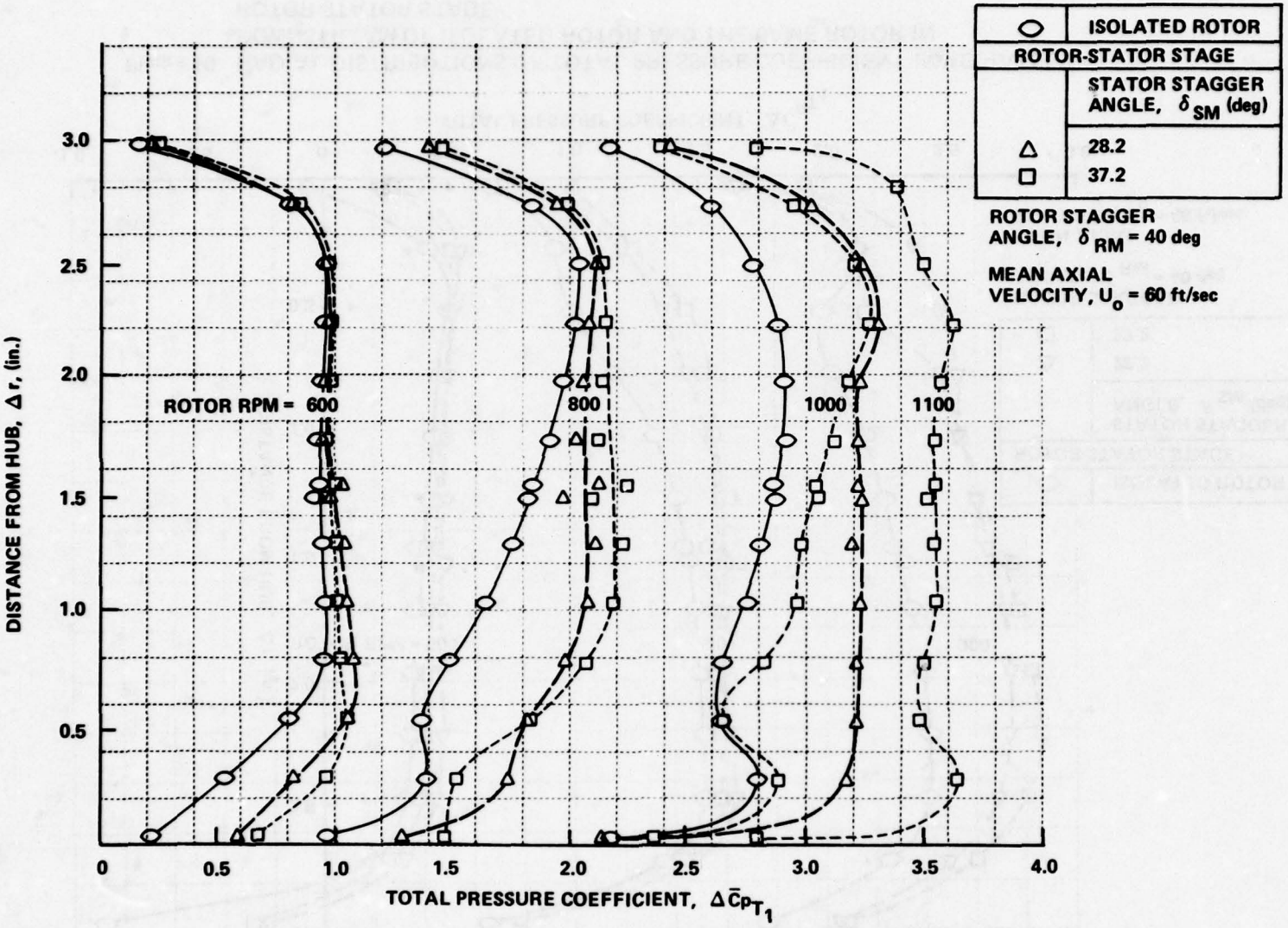


Figure 10 (Cont.) RADIAL DISTRIBUTIONS OF TOTAL PRESSURE COEFFICIENT IMMEDIATELY DOWNSTREAM OF ISOLATED ROTOR AND THE SAME ROTOR IN A ROTOR-STATOR STAGE

b. ROTOR RPM = 600, 800, 1000, 1100

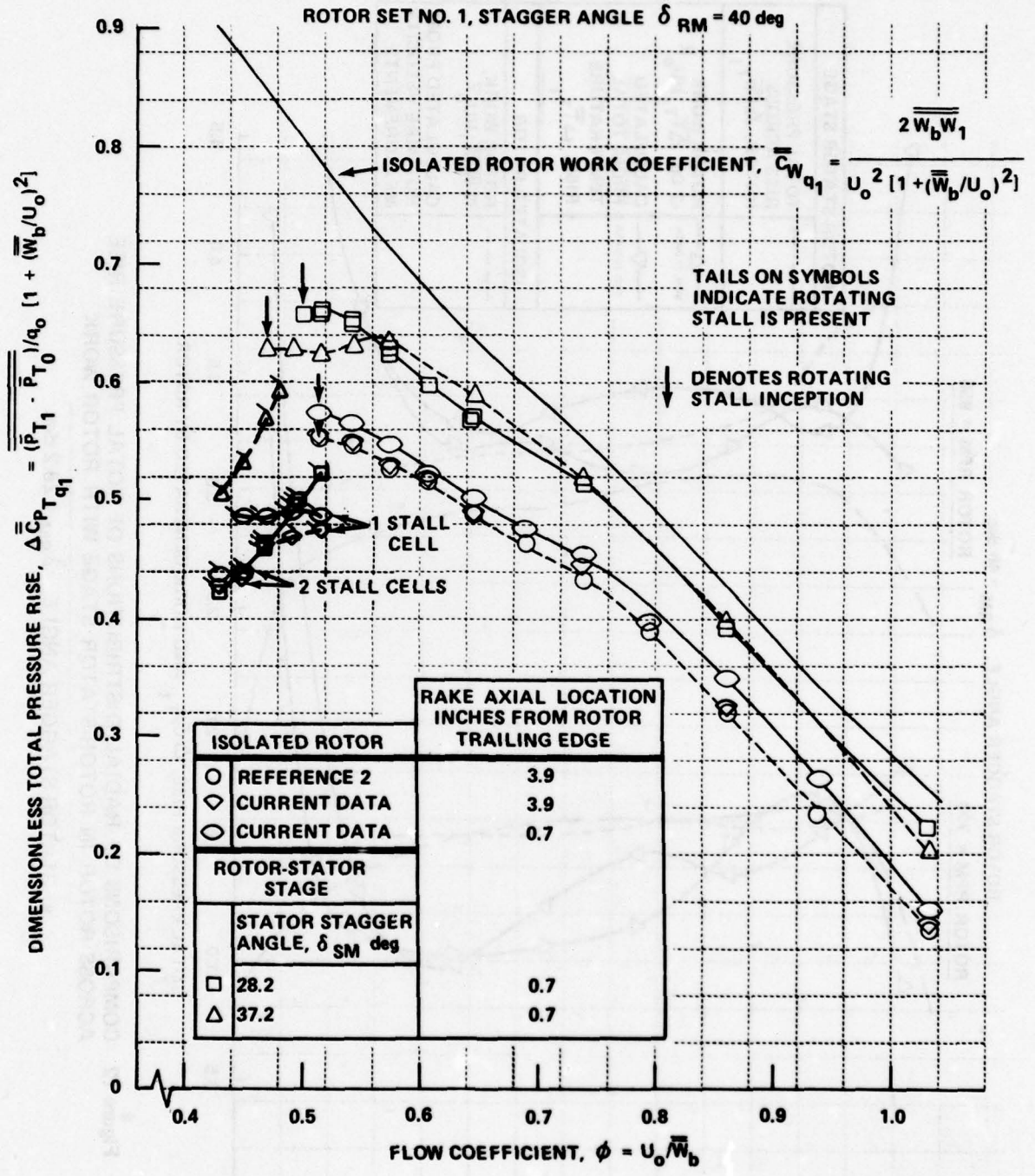


Figure 11 TOTAL PRESSURE RISE ACROSS ISOLATED ROTOR AND ACROSS ROTOR IN CLOSELY COUPLED ROTOR-STATOR STAGE

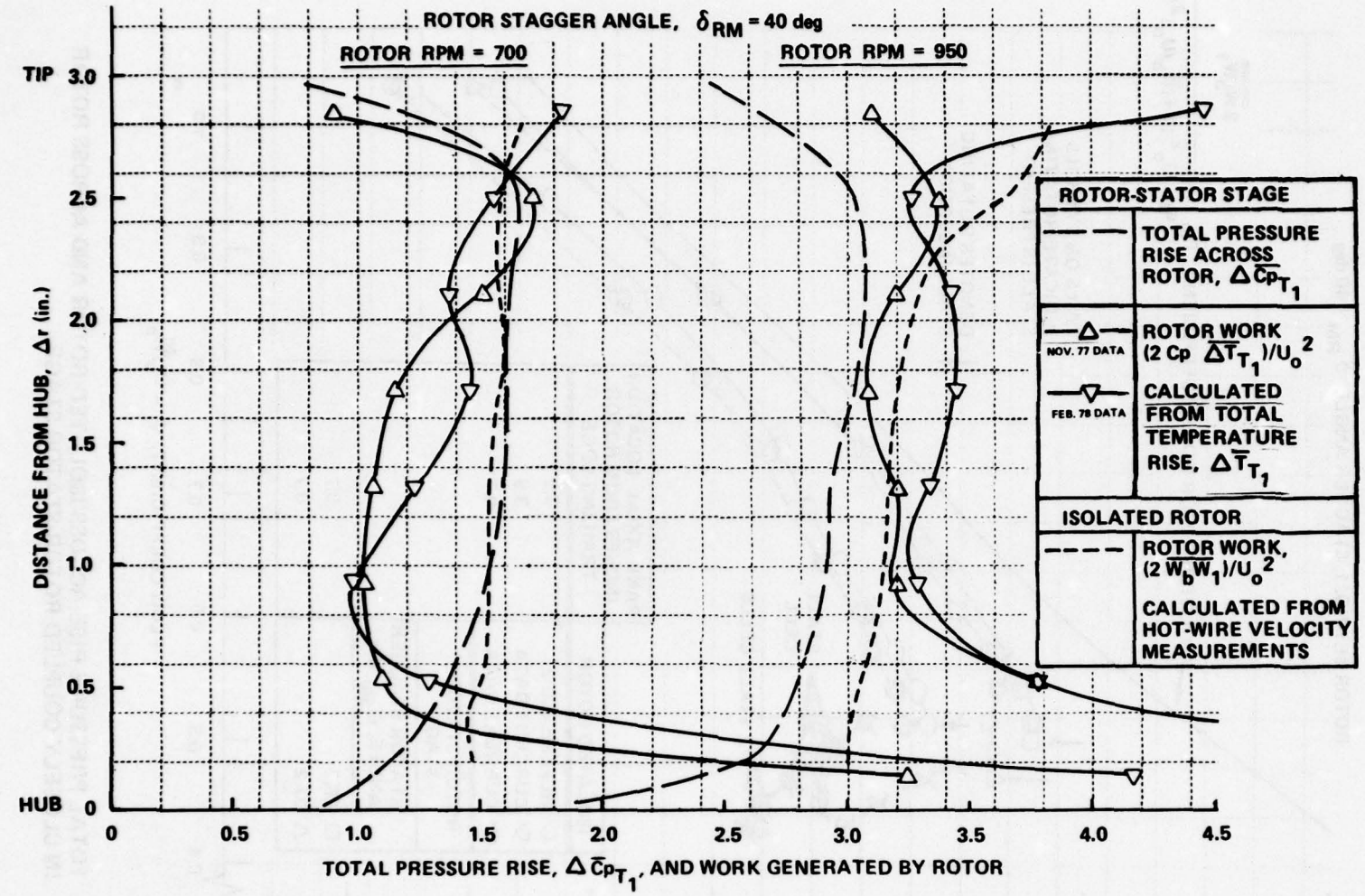


Figure 12 COMPARISONS OF RADIAL DISTRIBUTIONS OF TOTAL PRESSURE RISE ACROSS ROTOR IN ROTOR-STATOR STAGE WITH ROTOR WORK

a. STATOR STAGGER ANGLE, δ_{SM} = 28.2 deg

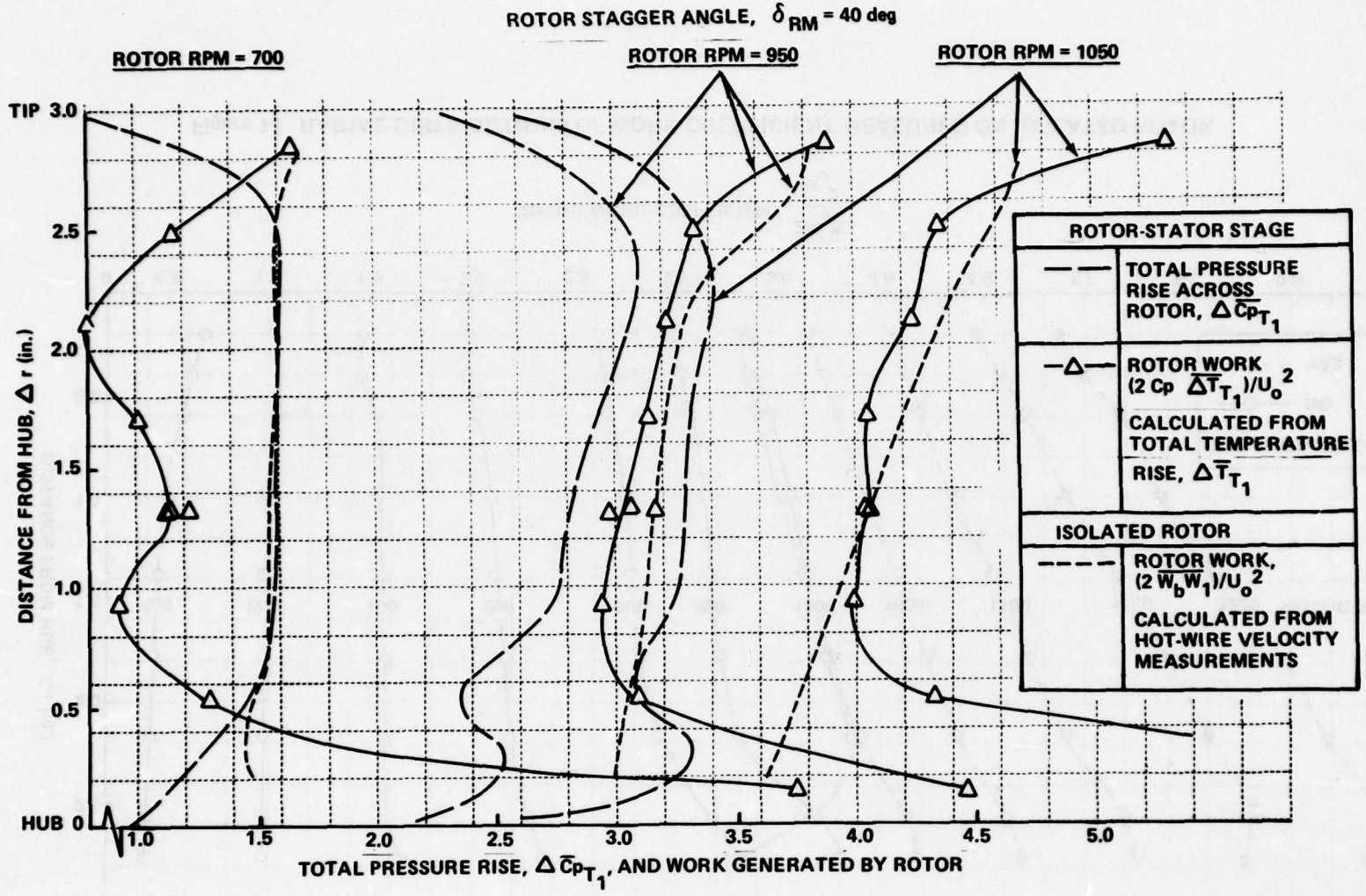


Figure 12 (Cont.) COMPARISONS OF RADIAL DISTRIBUTIONS OF TOTAL PRESSURE RISE ACROSS ROTOR IN ROTOR-STATOR STAGE WITH ROTOR WORK

b. STATOR STAGGER ANGLE, δ_{SM} = 37.2 deg

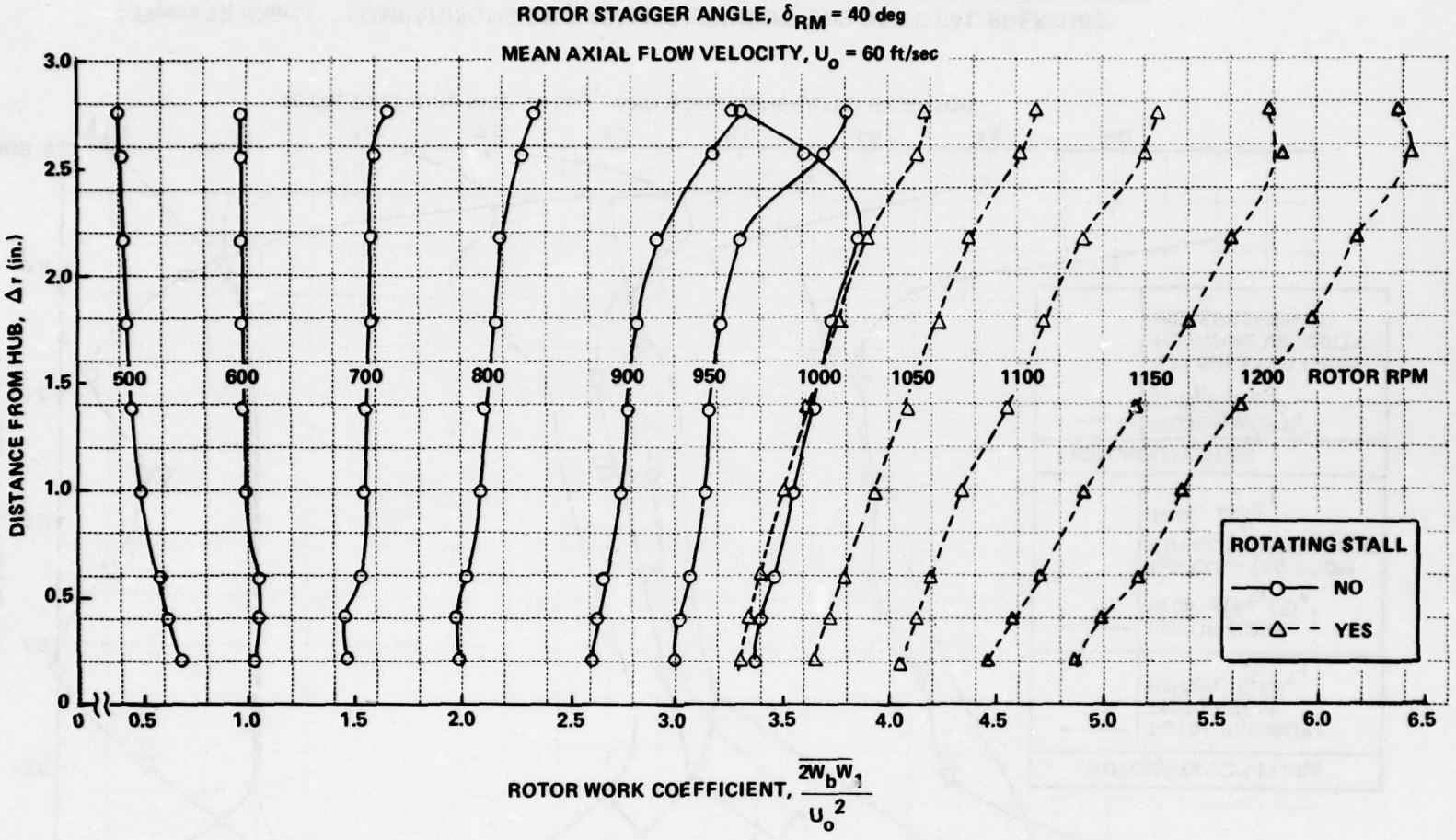


Figure 13 RADIAL DISTRIBUTIONS OF WORK COEFFICIENT MEASURED ON ISOLATED ROTOR

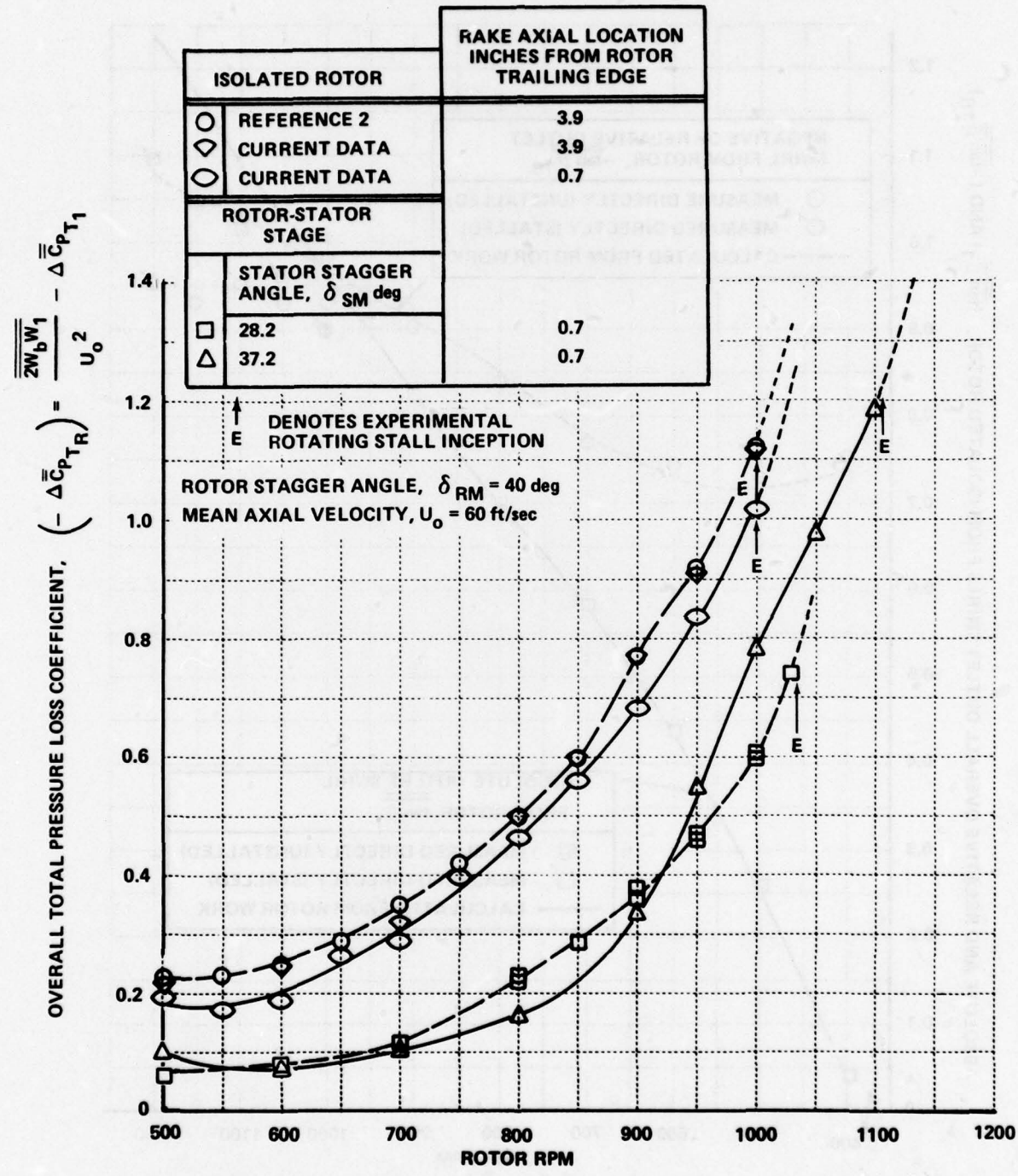


Figure 14 OVERALL TOTAL PRESSURE LOSS THROUGH ROTOR IN ROTOR-STATOR STAGE, COORDINATE SYSTEM RELATIVE TO ROTOR

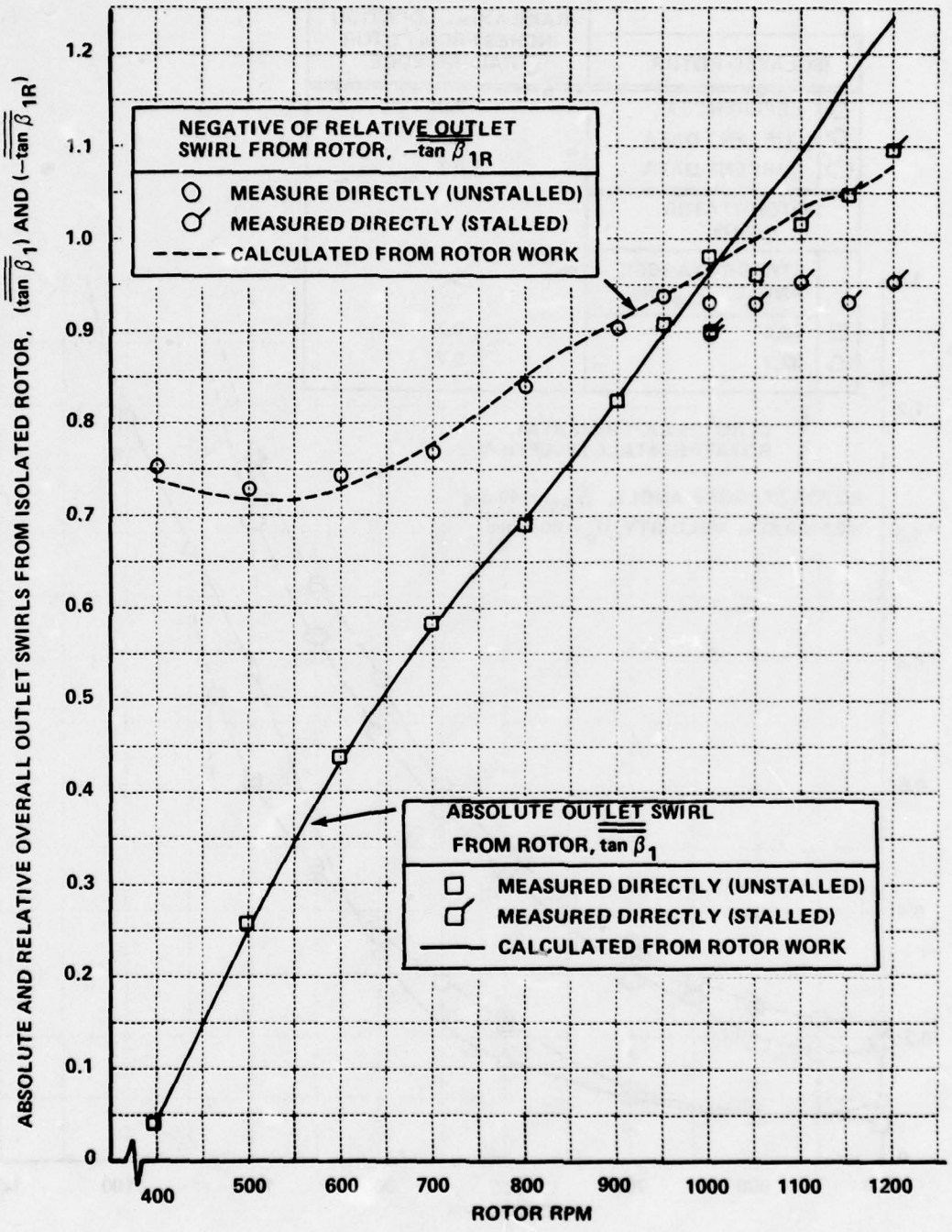


Figure 15 COMPARISON OF OVERALL OUTLET SWIRL FROM ISOLATED ROTOR CALCULATED FROM ROTOR WORK WITH DIRECT MEASUREMENTS

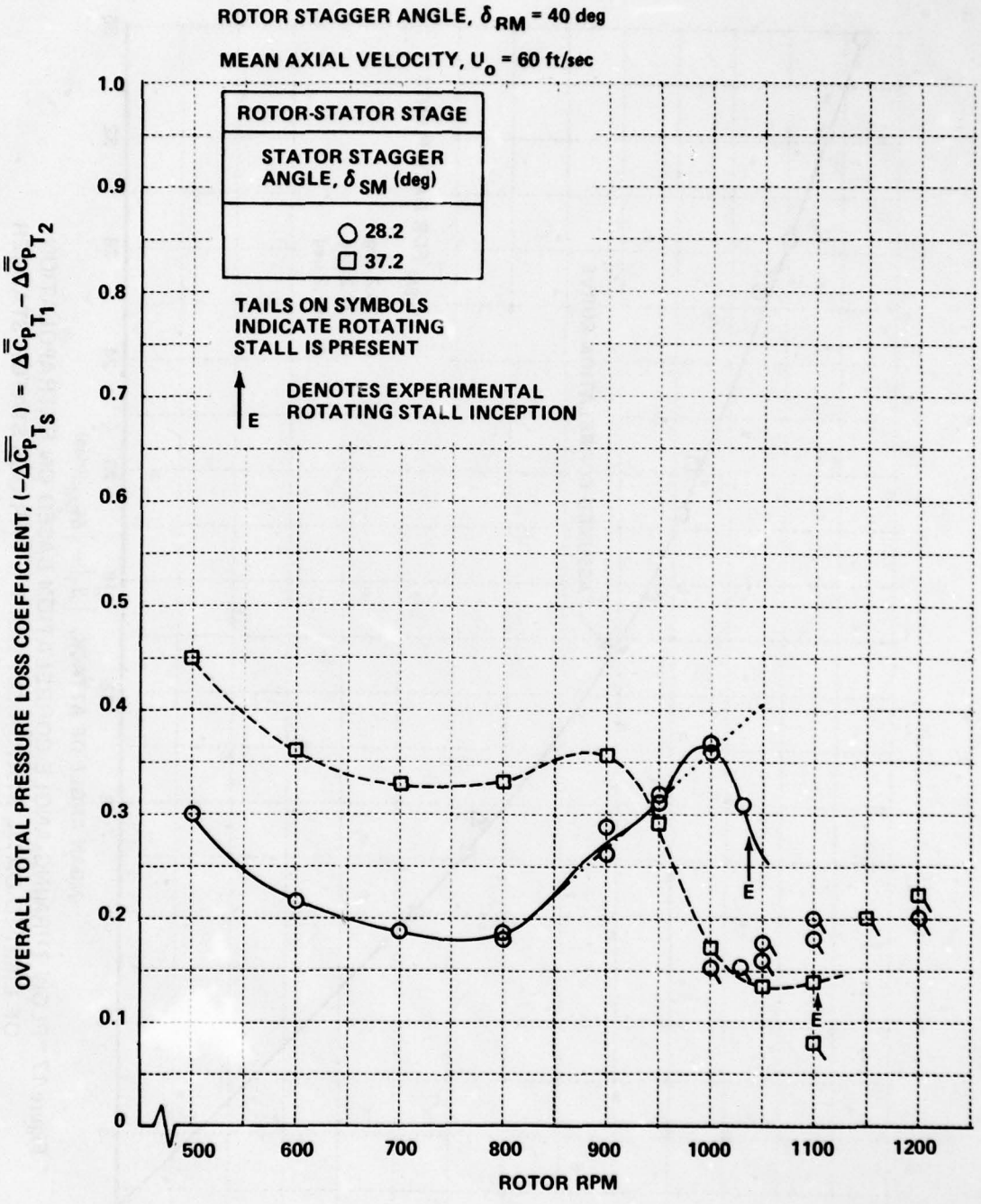


Figure 16 OVERALL TOTAL PRESSURE LOSS THROUGH STATORS IN ROTOR-STATOR STAGE

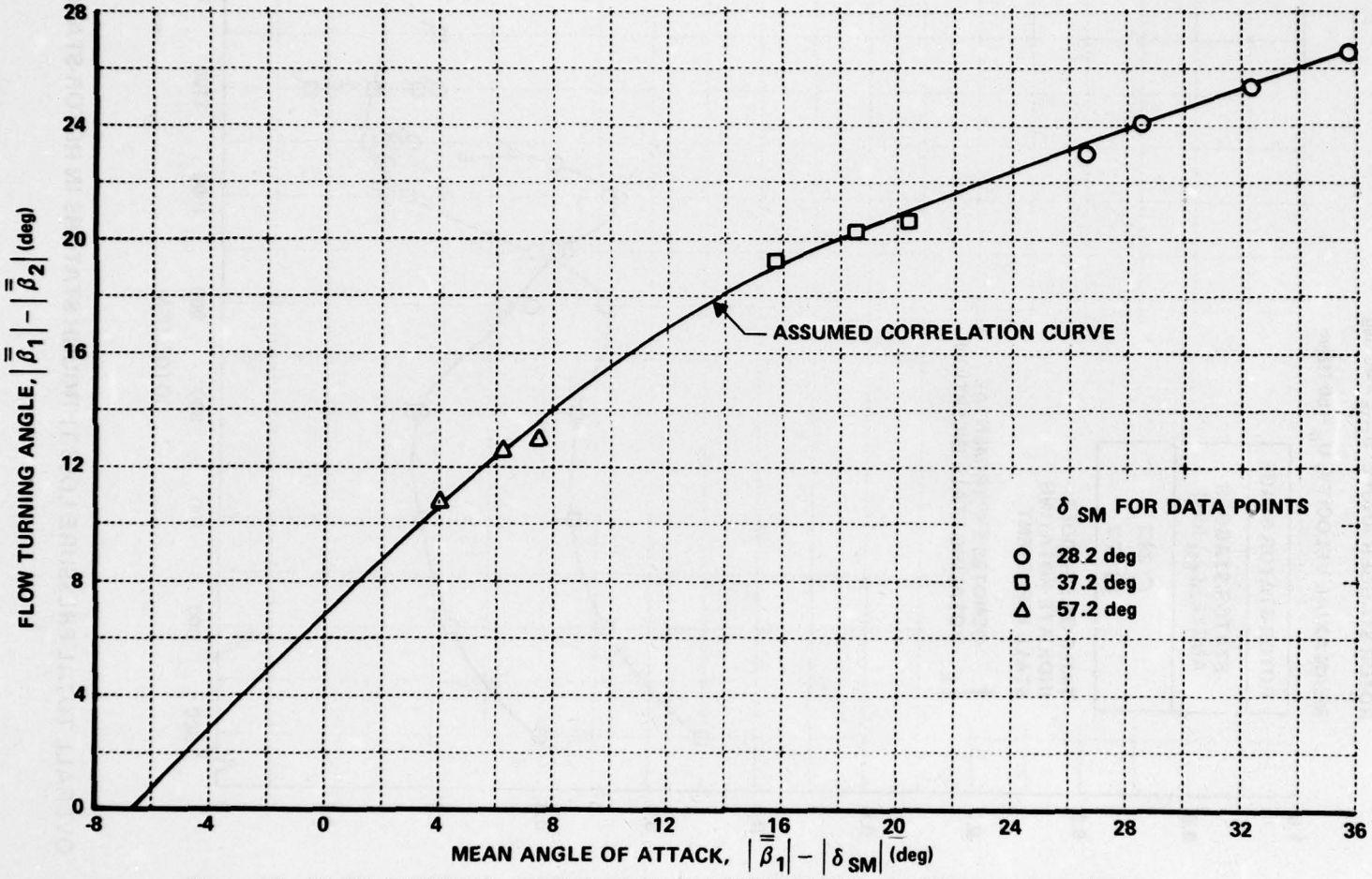


Figure 17 FLOW TURNING ANGLE CORRELATION BASED ON EXTRAPOLATION OF LIMITED DATA, STATOR SET NO. 1 – VARIOUS STATOR STAGGER ANGLES, δ_{SM}

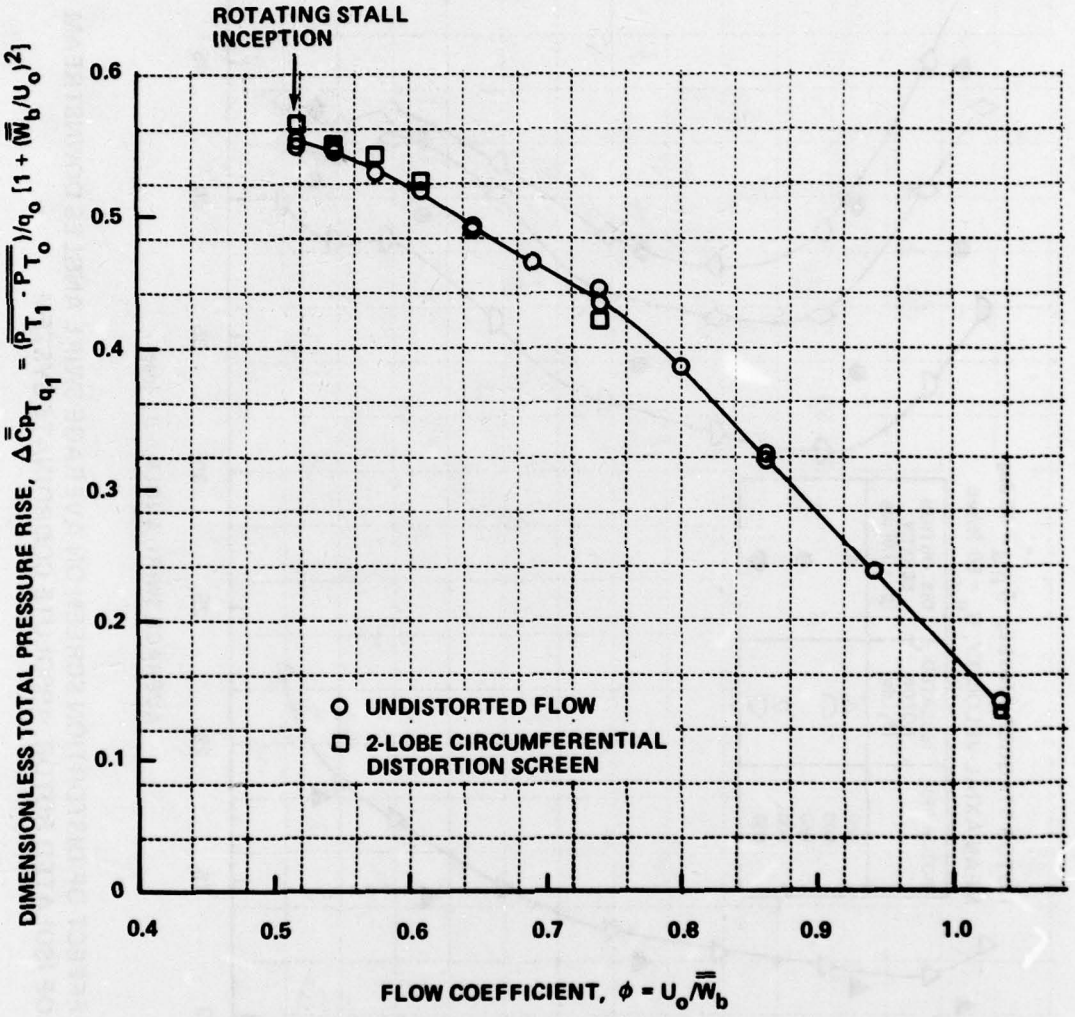


Figure 18 EFFECT OF DISTORTION SCREEN ON TOTAL PRESSURE RISE OF ISOLATED ROTOR, ABSOLUTE COORDINATE SYSTEM

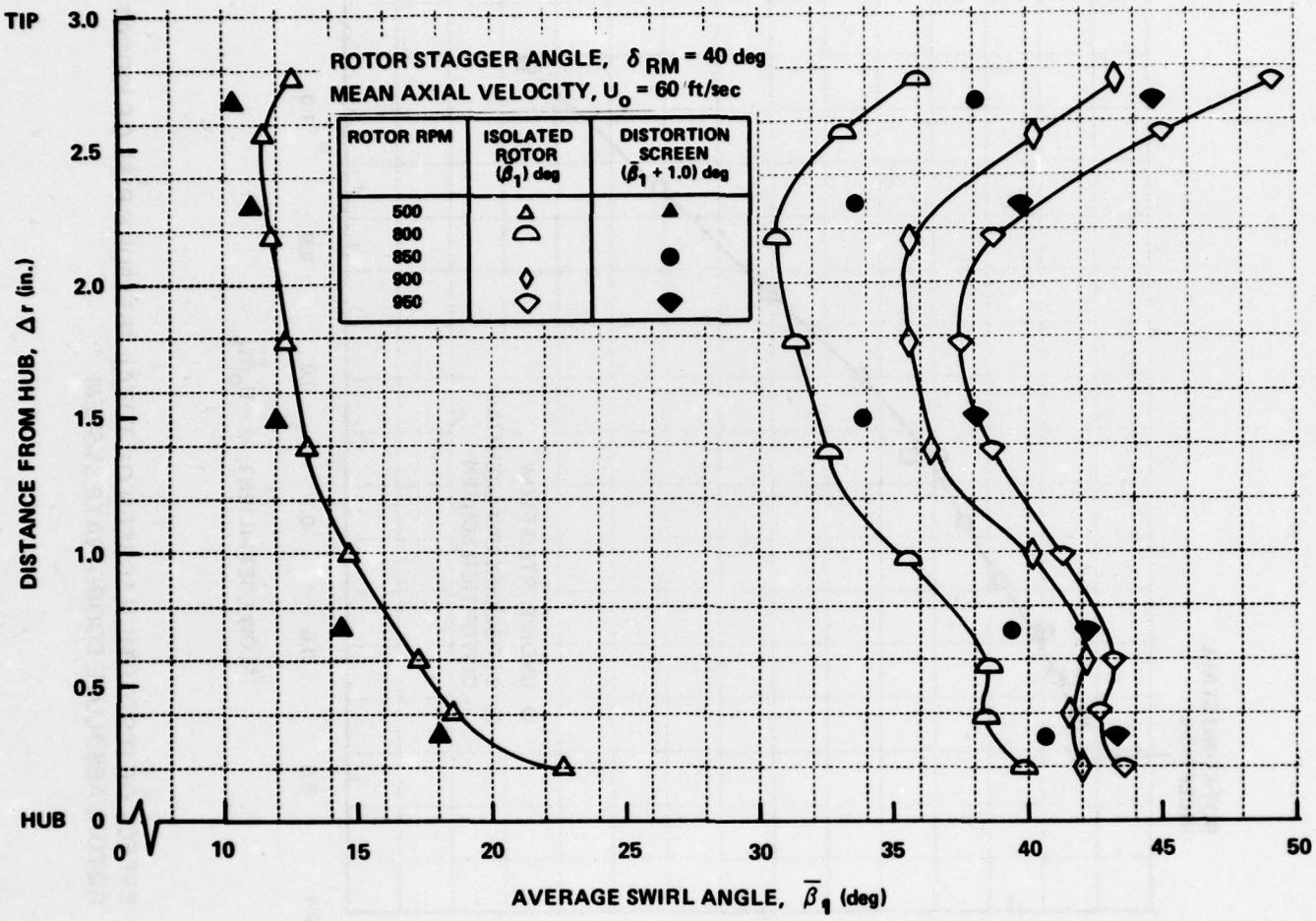
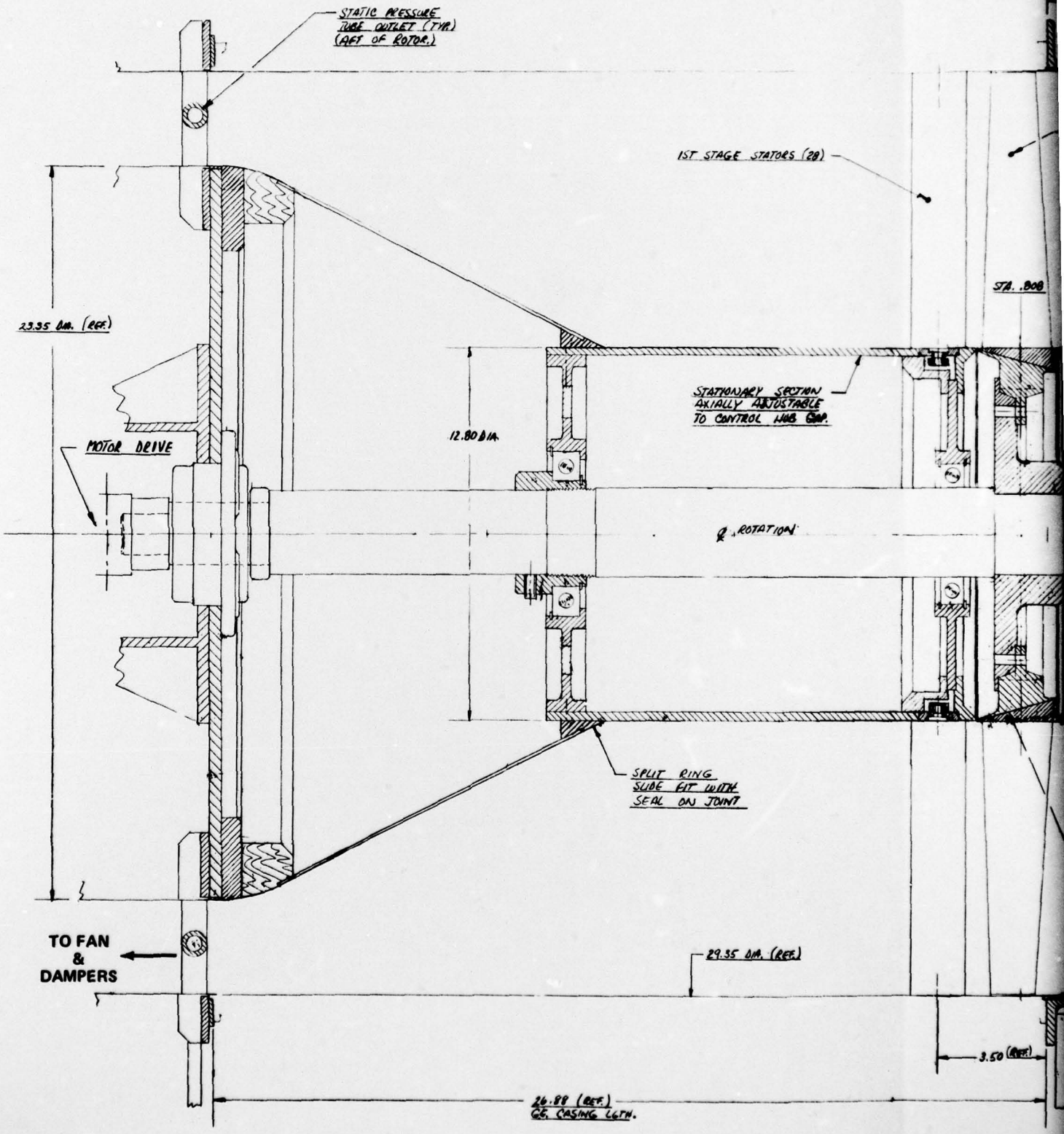


Figure 19 EFFECT OF DISTORTION SCREEN ON AVERAGE SWIRL ANGLES DOWNSTREAM OF ISOLATED ROTOR, ABSOLUTE COORDINATE SYSTEM


STATIC PRESSURE TAP OUTLET (TYP.) (AFT OF ROTOR.)
1ST STAGE STATORS (28)
STA. .808
23.35 DIA. (REF.)
STATIONARY SECTION AXIALLY ADJUSTABLE TO CONTROL HUB GAP.
12.80 DIA.
MOTOR DRIVE
ROTATION
SPLIT RING SLIDE FIT WITH SEAL ON JOINT
TO FAN & DAMPERS
29.35 DIA. (REF.)
3.50 (REF.)
26.88 (REF.) OF CASING LGTH.

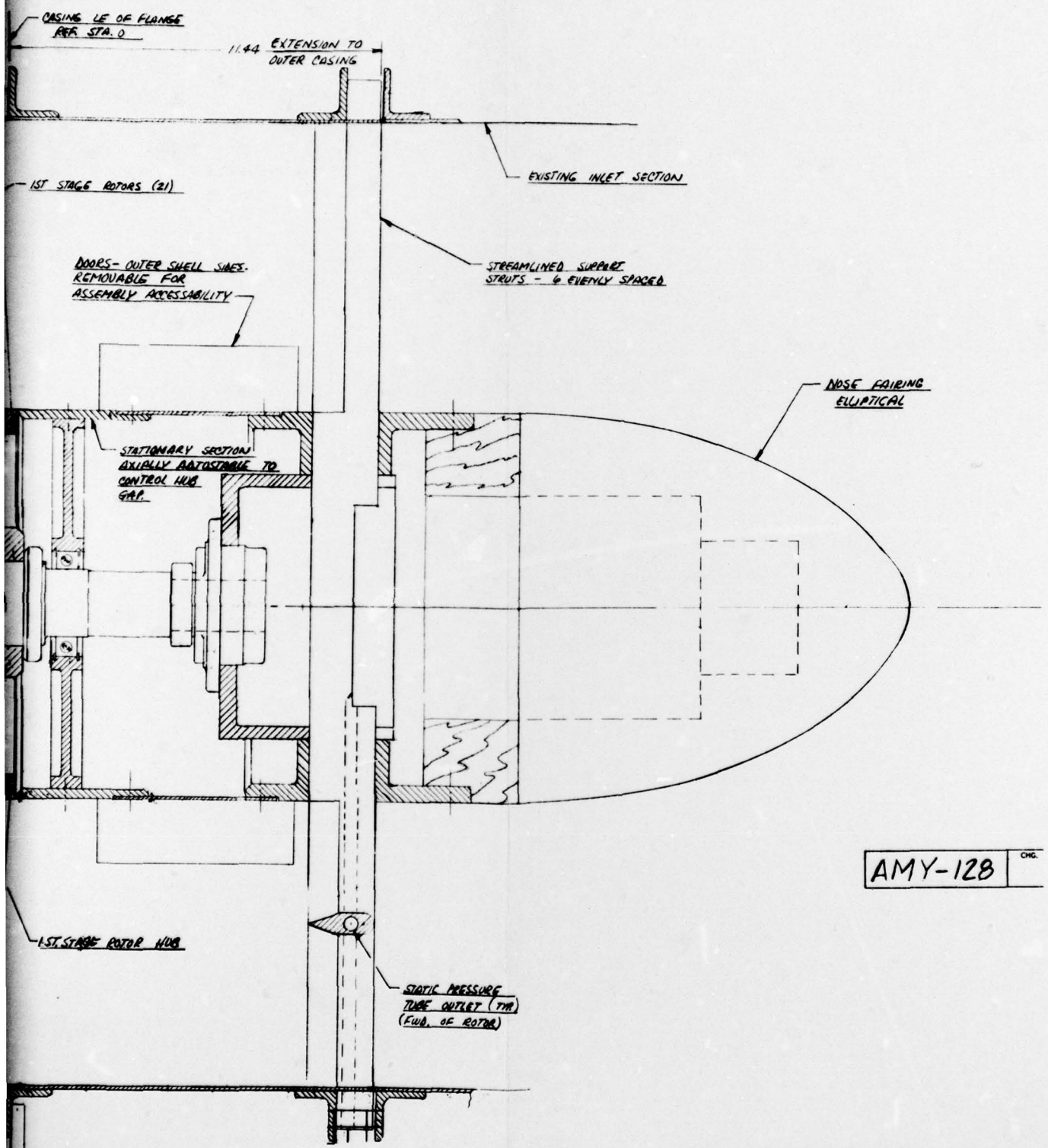


Figure 20 ANNULAR CASCADE WITH LOW HUB-TO-TIP RATIO

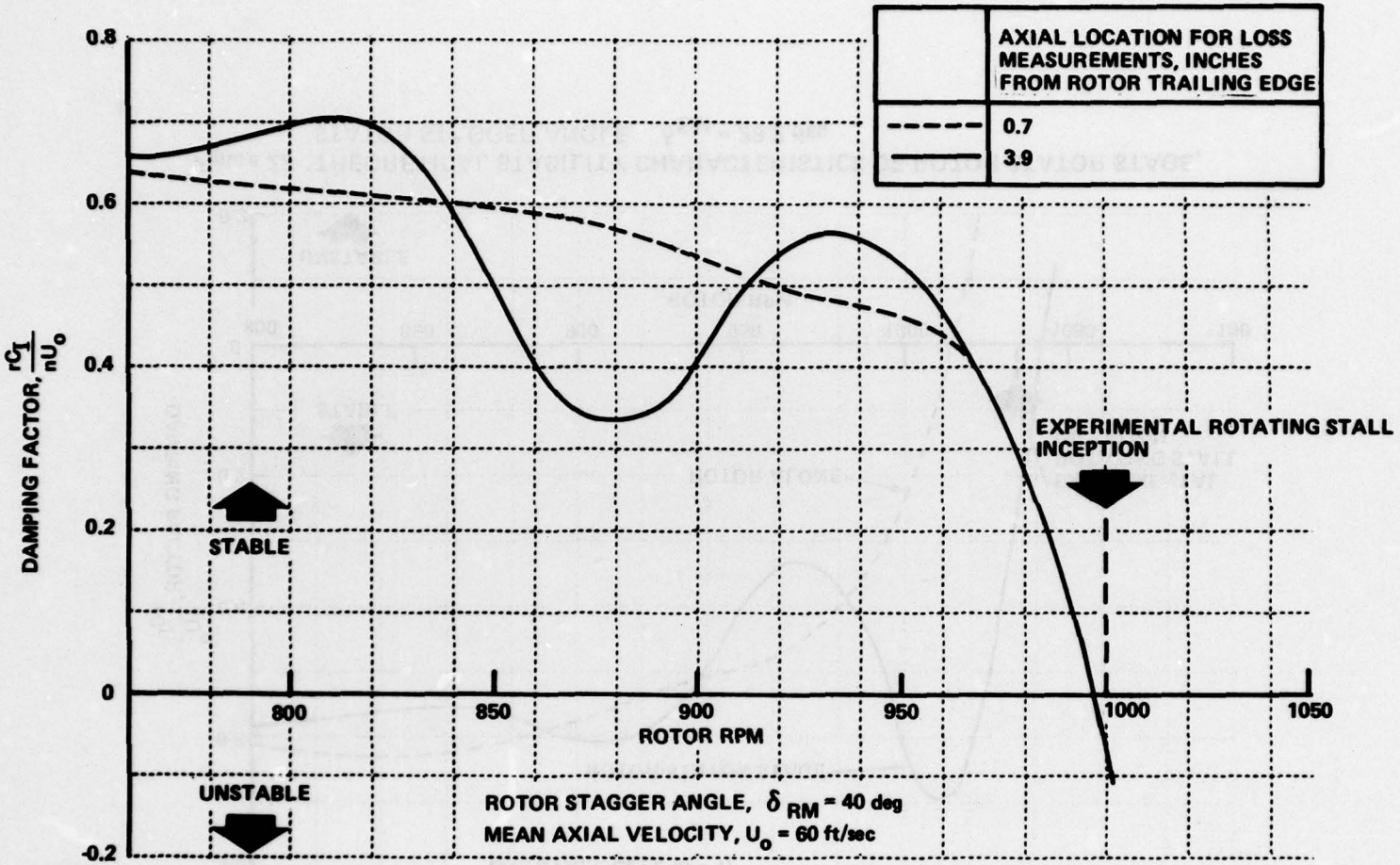


Figure 21 THEORETICAL STABILITY CHARACTERISTICS OF ISOLATED ROTOR

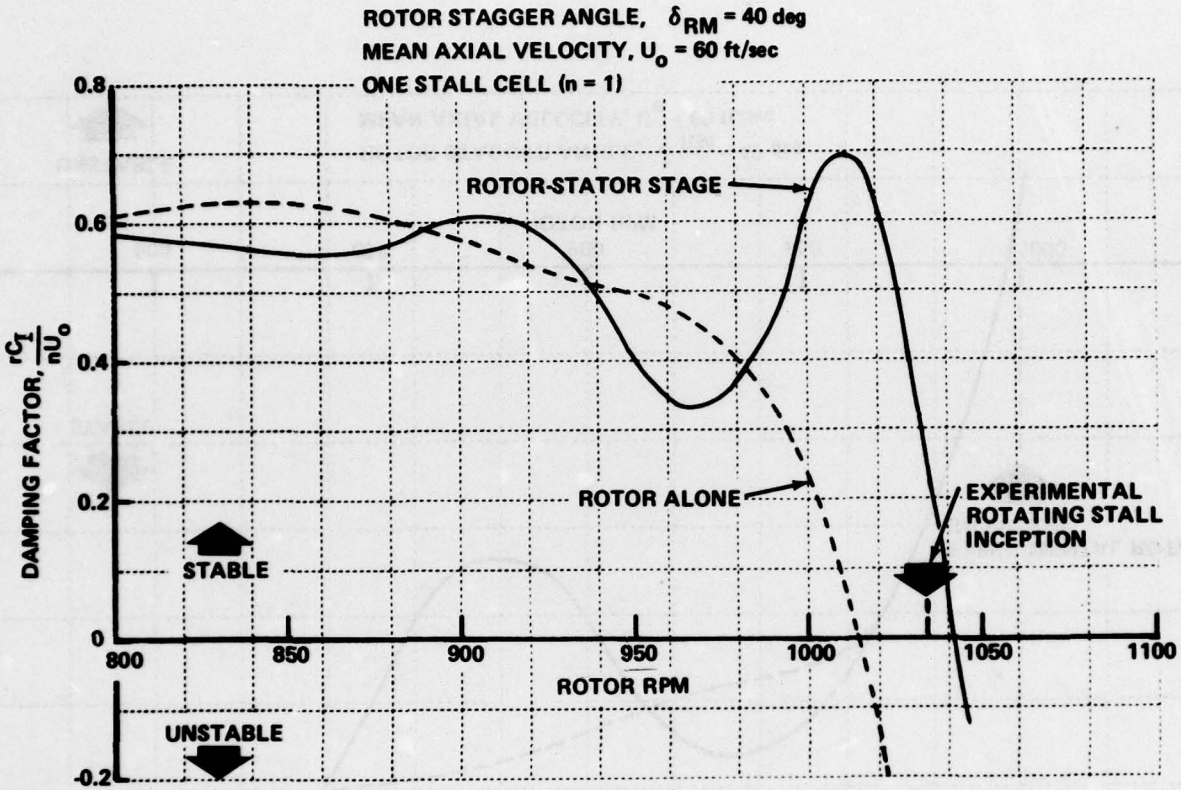


Figure 22 THEORETICAL STABILITY CHARACTERISTICS OF ROTOR-STATOR STAGE, STATOR STAGGER ANGLE, δ_{SM} = 28.2 deg

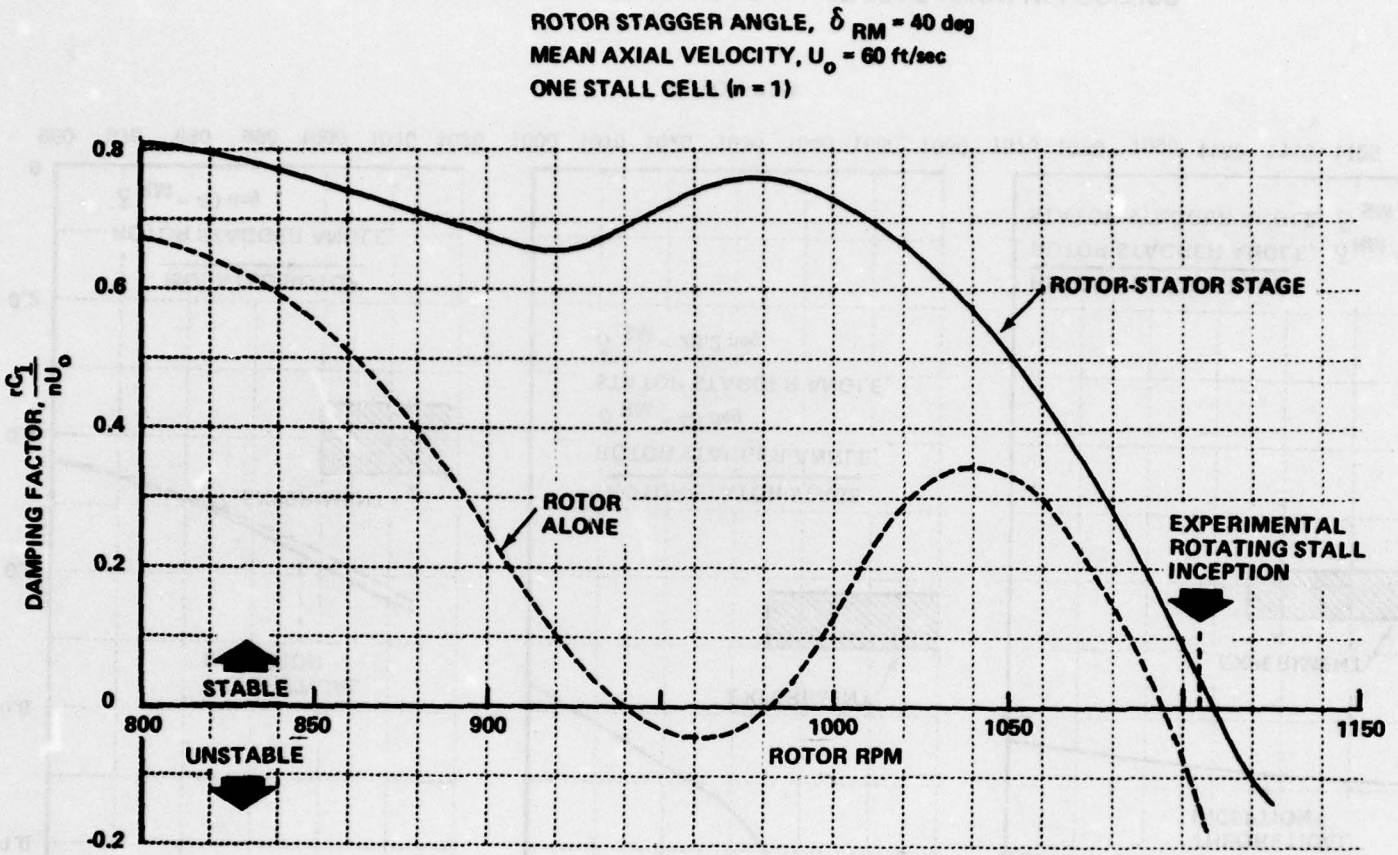


Figure 23 THEORETICAL STABILITY CHARACTERISTICS OF ROTOR-STATOR STAGE, STATOR STAGGER ANGLE, δ_{SM} = 37.2 DEG

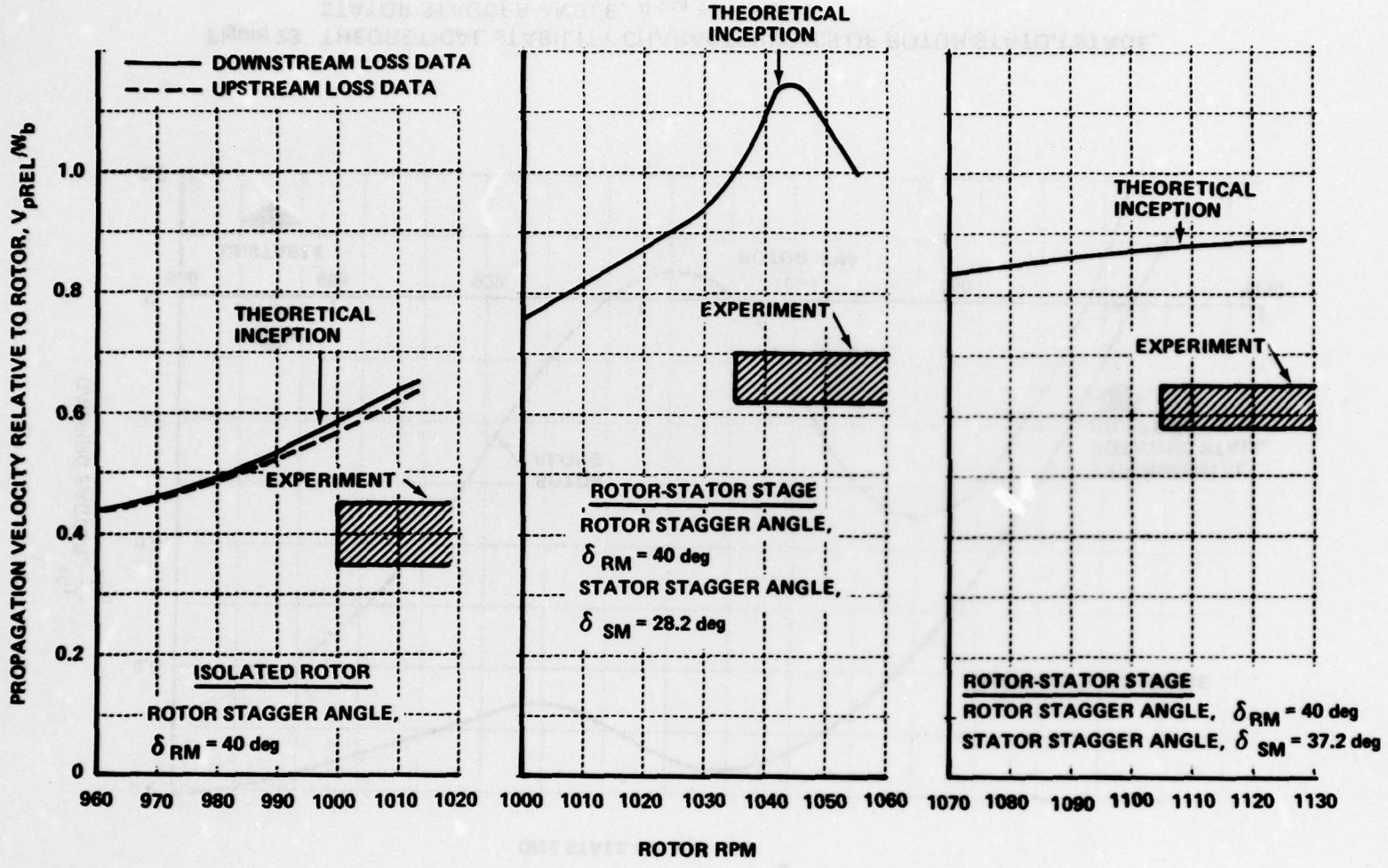


Figure 24 THEORETICAL ROTATING STALL PROPAGATION VELOCITIES

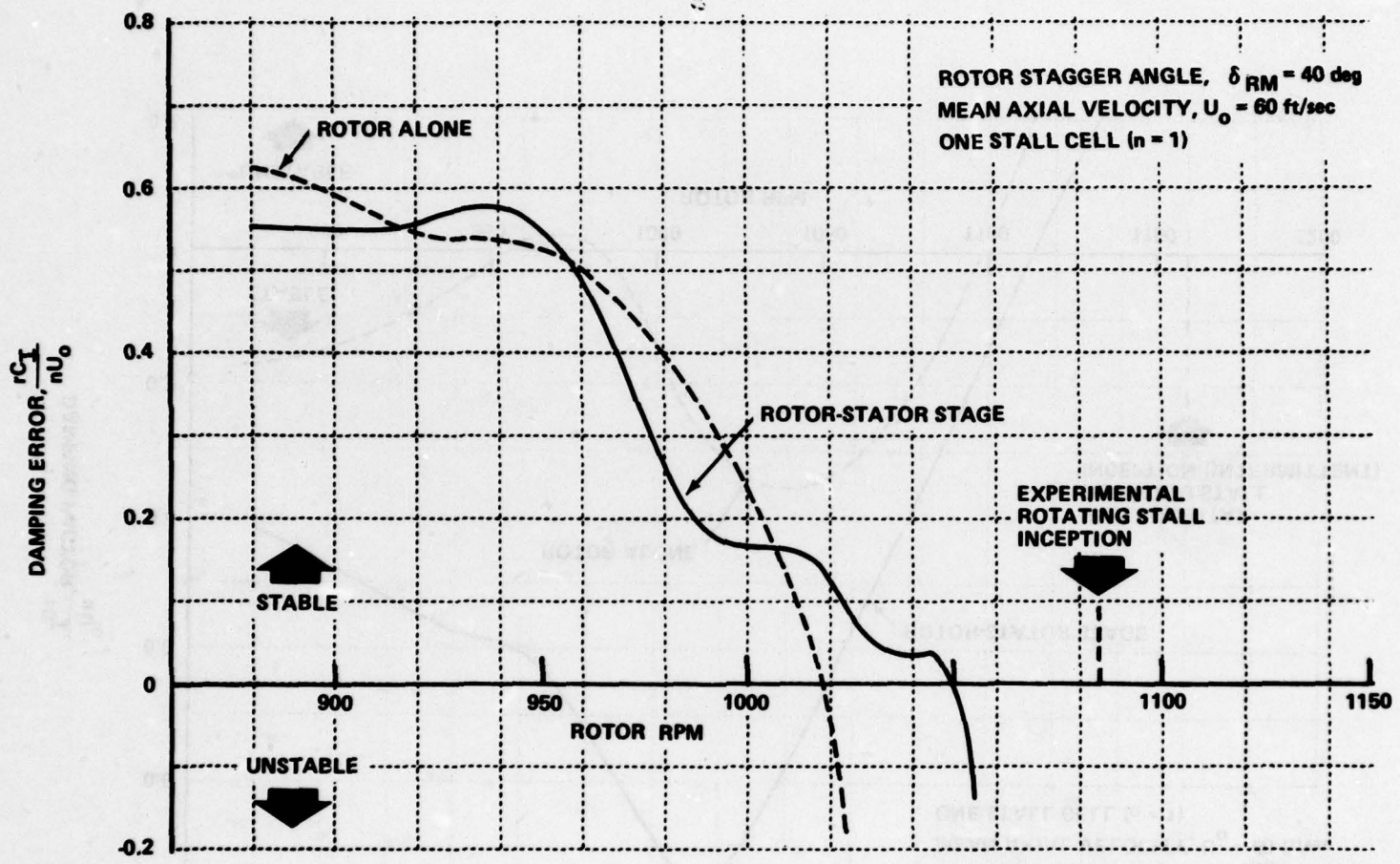


Figure 25 THEORETICAL STABILITY CHARACTERISTICS OF ROTOR-STATOR STAGE WITH CIRCUMFERENTIAL INLET DISTORTION, STATOR STAGGER ANGLE, δ_{SM} = 28.2 DEG

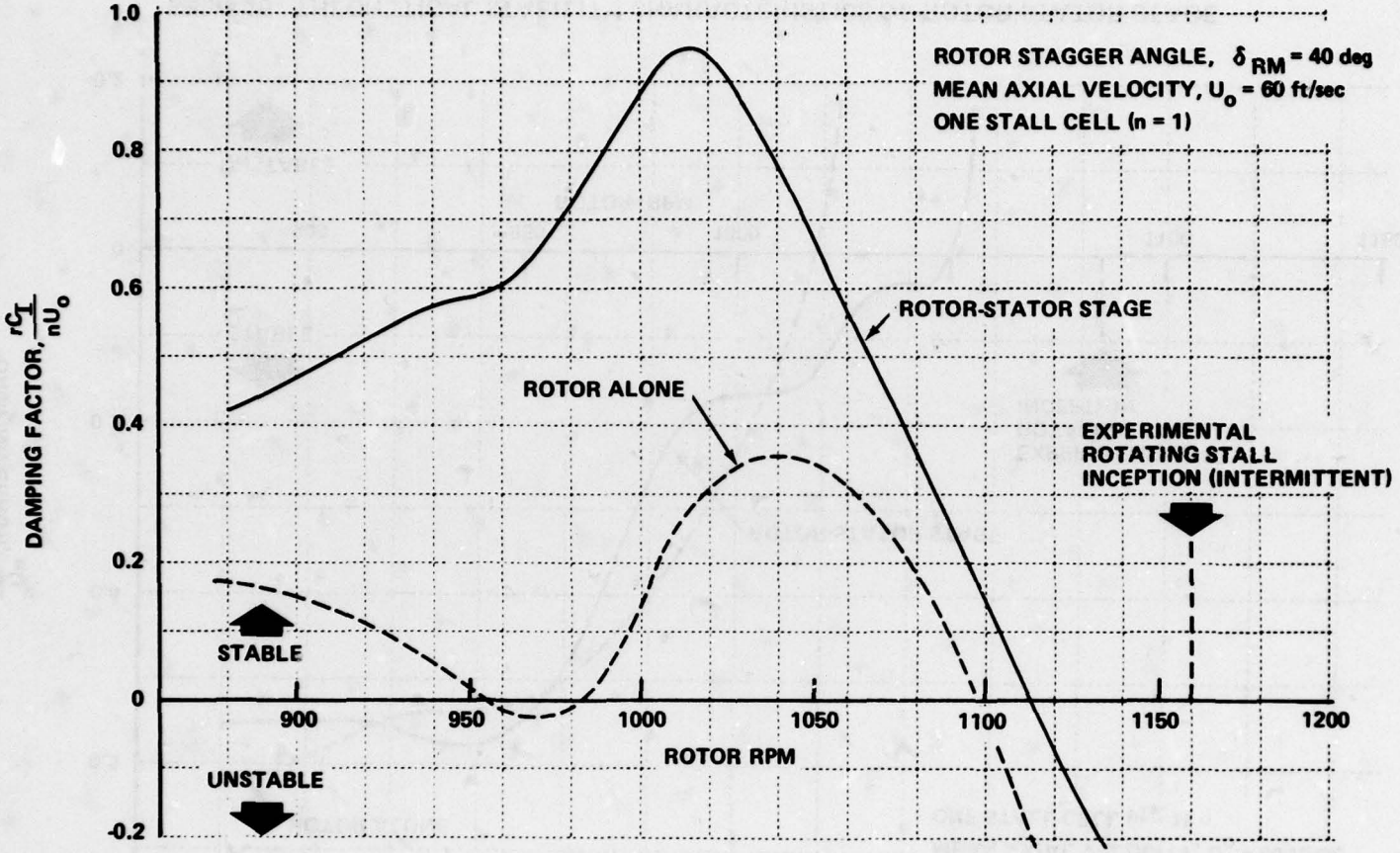


Figure 26 THEORETICAL STABILITY CHARACTERISTICS OF ROTOR-STATOR STAGE WITH CIRCUMFERENTIAL INLET DISTORTION, STATOR STAGGER ANGLE, δ_{SM} = 37.2 deg

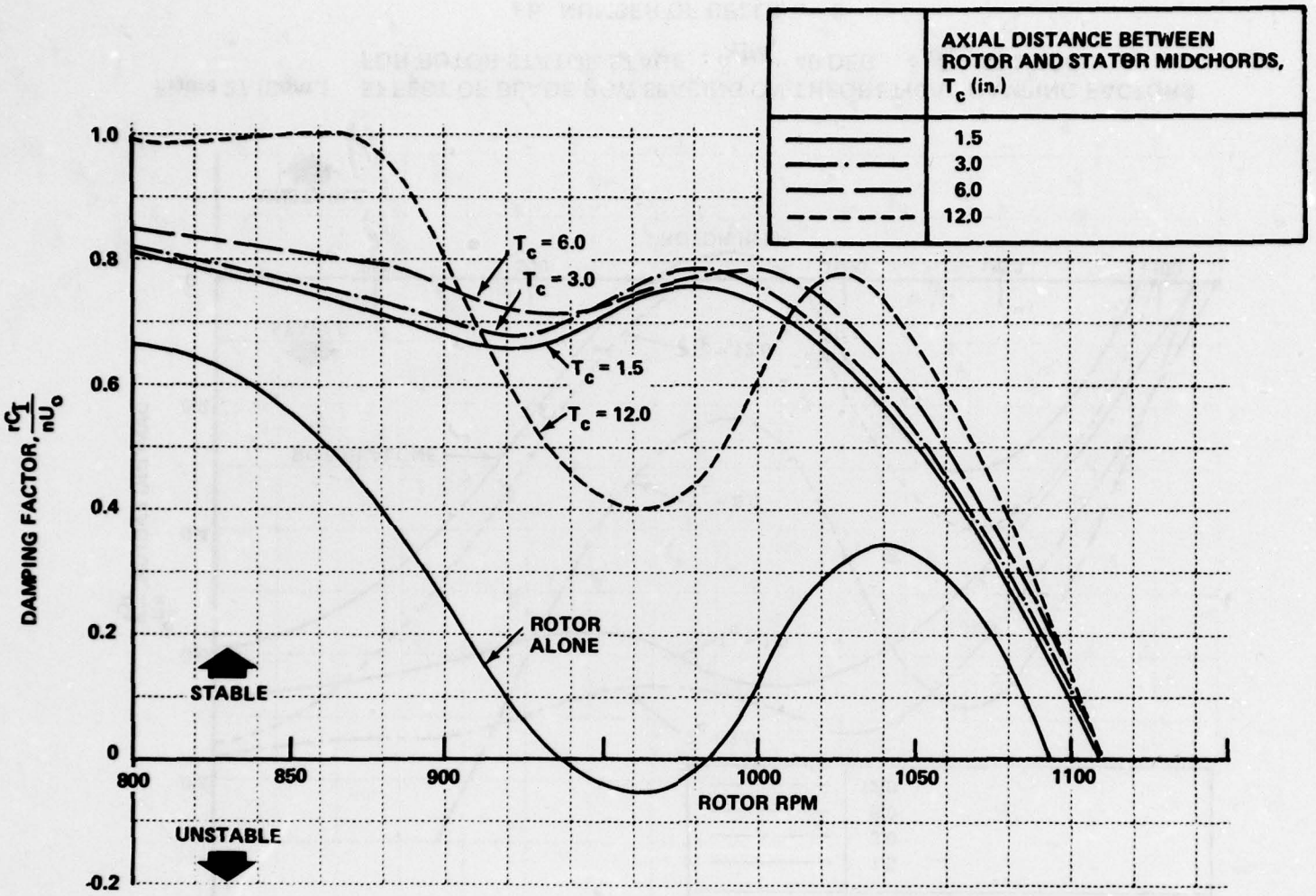


Figure 27 EFFECT OF BLADE ROW SPACING ON THEORETICAL DAMPING FACTORS FOR ROTOR-STATOR STAGE, δ_{RM} = 40 DEG, δ_{SM} = 37.2 DEG

a. NUMBER OF CELLS, n = 1

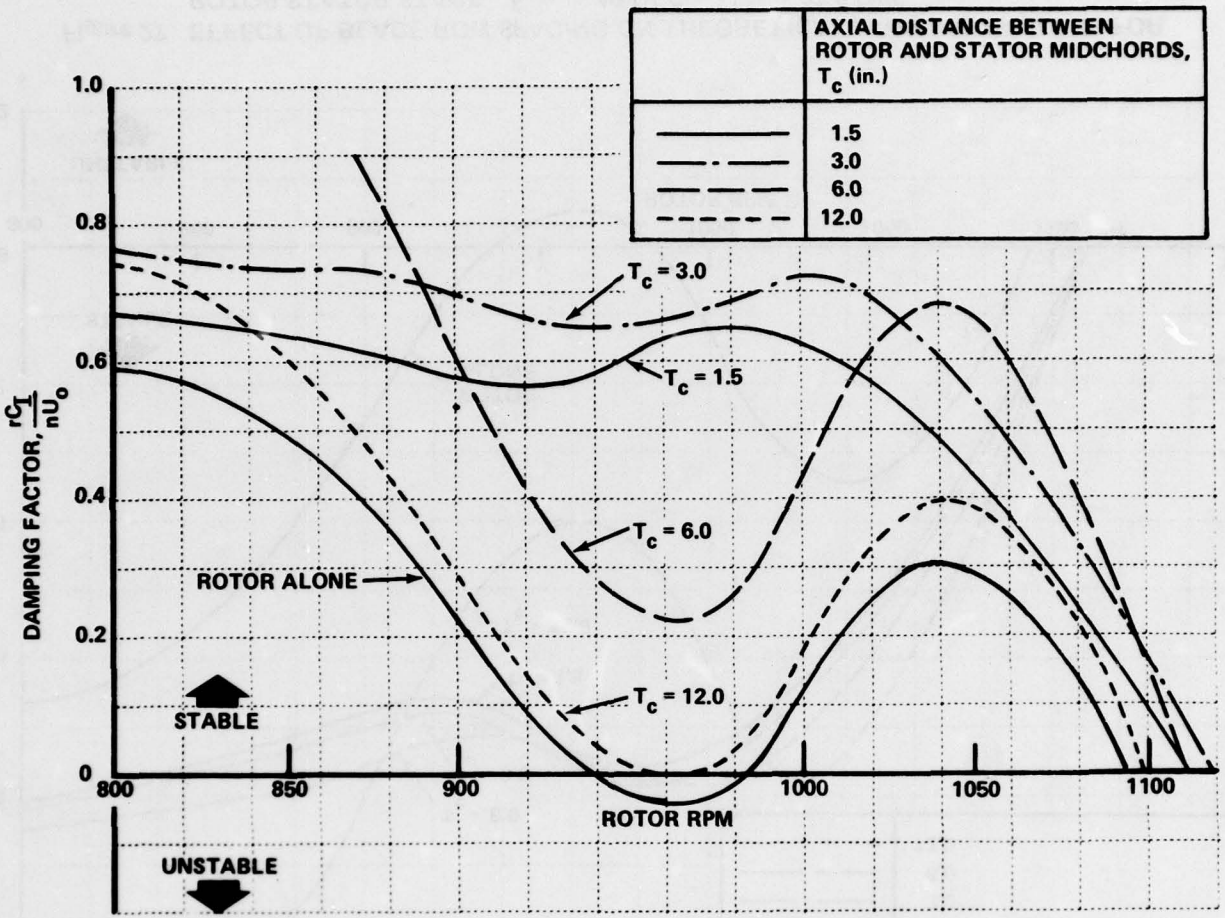


Figure 27 (Cont.) EFFECT OF BLADE ROW SPACING ON THEORETICAL DAMPING FACTORS FOR ROTOR-STATOR STAGE, δ_{RM} = 40 DEG, δ_{SM} = 37.2 DEG

b. NUMBER OF CELLS, n = 3

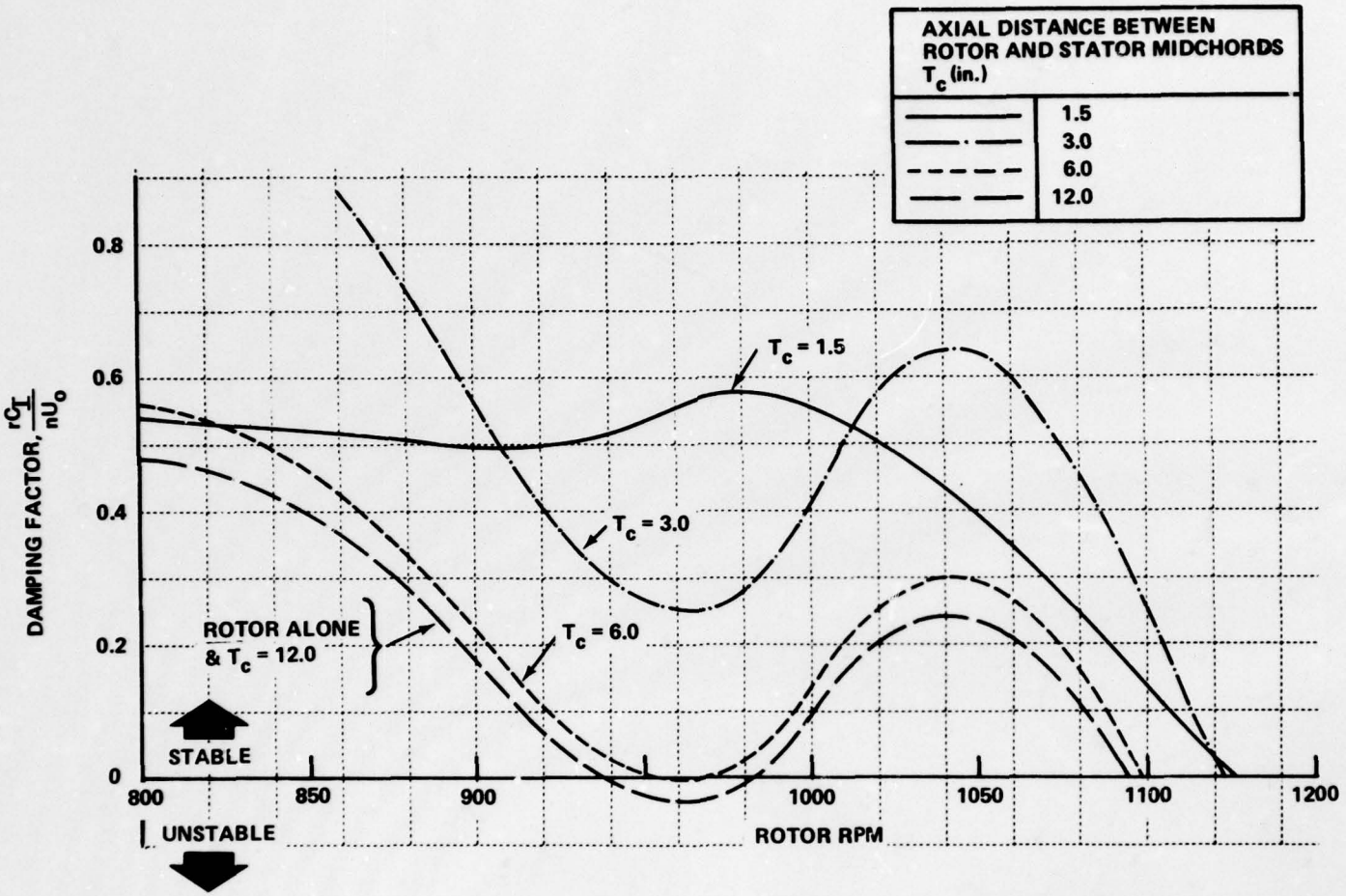


Figure 27 (Cont.) EFFECT OF BLADE ROW SPACING ON THEORETICAL DAMPING FACTORS FOR ROTOR-STATOR STAGE, δ_{RM} = 40 DEG, δ_{SM} = 37.2 DEG

c. NUMBER OF CELLS, n = 7

*U.S.Government Printing Office: 1979 — 657-084/253